

Masterarbeit

Zur Erlangung des akademischen Grades Master of Science

**Time-, momentum- and towards
branch-resolved phonon dynamics in MoS₂**

Humboldt-Universität zu Berlin
Mathematisch-Naturwissenschaftliche Fakultät I
Institut für Physik

eingereicht von: Patrick-Nigel Hildebrandt
geboren am: 14.08.1994, Berlin
Betreuung: Prof. Christoph T. Koch
(Humboldt-Universität zu Berlin)
Prof. Dr. Ralph Ernstorfer
(TU Berlin und Fritz-Haber-Institut der MPG)
eingereicht am: 21.12.2021

Abstract

In this thesis we combine femtosecond electron diffuse scattering experiments and ab initio calculations to study the non-equilibrium lattice dynamics in a thin film of photo-excited MoS₂. By simultaneously analyzing the elastic and diffuse scattering signals, we reveal the non-thermal character of lattice dynamics and obtain a detailed momentum-resolved view on the electron-phonon and phonon-phonon coupling over a wide range of the Brillouin zone. We also explore the extent to which branch-resolution can be extracted from the data. We show that our ability to retrieve energy resolution is inherently limited by multicollinearity of the branch-resolved structure factors and multi-phonon scattering. These effects, observed in MoS₂, are expected to play significant roles in most materials of similar complexity. We find that partial energy-resolution can nevertheless be achieved by reducing the number of phonon branches by grouping them into effective branches. Overall, this work contributes to a deeper understanding of the recently developed time-resolved diffuse scattering methods. This understanding is necessary in view of reaching the ultimate goal of a phonon mode-resolved view of lattice dynamics in materials.

Contents

1	Abbreviations	7
2	Introduction	8
3	Electron diffraction theory	10
3.1	Diffraction from crystals	10
3.1.1	Scattering intensity and phonons	12
3.1.2	Elastic scattering	14
3.1.3	Inelastic scattering	15
3.1.4	Thin film effect	16
3.2	The time-, momentum- and branch-resolved approach	17
3.2.1	Approximations	19
4	Regression theory	22
4.1	Linear overdetermined regression problems	22
4.2	Least squares method	22
4.3	Detection of multicollinearity	23
4.4	Least square algorithms	24
5	Molybdenum disulfide	25
5.1	Crystal structure	25
5.2	Electronic band structure	27
5.3	Phonon dispersion	28
5.4	One-phonon contribution calculations	29
6	Self-consistency and the role of multicollinearity	31
6.1	Determination of phonon temperatures	31
6.2	Self-consistency test on graphene	32
6.3	Branch binning	36
6.4	Self-consistency test with binned phonon system	36
7	Experimental methods	39
7.1	Experimental setup	39
7.2	Sample preparation	41
7.3	Pump parameters	42
7.4	Data processing	43
7.4.1	Reciprocal space mapping of diffraction patterns	47
7.4.2	Sampling of the first Brillouin zone	52
8	Elastic scattering analysis	53
8.1	Results	53
8.2	Quantification of lattice dynamics	56
8.3	Breathing modes in MoS ₂	58

9 Inelastic scattering analysis	62
9.1 Overview of inelastic signals	62
9.2 Quantification of inelastic signals	65
9.2.1 Phonon dynamics around the Brillouin zone edges	66
9.2.2 Phonon dynamics around the Brillouin zone center	70
10 Towards branch-resolved inelastic scattering analysis	73
10.1 Self-consistency test on MoS ₂	73
10.1.1 Multicollinearity of one-phonon structure factor contributions .	74
10.2 Phonon branch binning on MoS ₂	76
10.3 Sensitivity of the experiment to effective phonon branches	78
10.4 Merging model and experimental intensities	79
10.4.1 Multi-phonon scattering effects	83
10.5 Results	84
10.6 Residuals	89
11 Conclusion	91
A Phonon branch polarization and energy of MoS₂	103
B Results of the residual fit	105
C Standard deviation of inelastic scattering fit parameters	106
D Complete phonon temperatures of every branch	107

1 Abbreviations

BZ Brillouin zone

BVLS Bounded variable least squares

CB Conduction band

CBM Conduction band minimum

DFT Density functional theory

DFPT Density functional perturbation theory

DWF Debye-Waller factor

EPC Electron-phonon coupling

FED Femtosecond electron diffraction

FEDS Femtosecond electron diffuse scattering

HPC High performance computation

MSD Mean squared displacement

NNLM Non-negative least squares

NLM Non-thermal lattice model

OPSF One phonon structure factor

OPC One phonon contribution

PPC Phonon-phonon coupling

SNR Signal-to-noise ratio

TEM Transmission electron microscopy

TTM Two-temperature model

UXDS Ultrafast x-ray diffuse scattering

VB Valence band

VBM Valence band maximum

2 Introduction

The complex and diverse interaction mechanisms between electrons and lattice (phonons) form the basis of our fundamental understanding of condensed matter phenomena. Interactions after the collective excitation of the electrons and/or phonons are known to play an important role for physical phenomena such as superconductivity, charge-density waves (CDW), multiferroicity, and soft-mode phase transitions [1, 2]. These interactions can be divided into two groups, electron-phonon and phonon-phonon interactions¹. Electron-phonon interactions are central to our understanding of electrical transport [3], optical response [4], and energy-conversion processes [5]. Phonon-phonon interactions are essential for a microscopic understanding of thermal conductivity and of the interactions between thermal phonons and defects [6]. The design of practical applications such as optoelectronic devices or field-effect transistors, which mainly operate in non-equilibrium conditions, strongly relies on the knowledge of the interaction mechanisms between the excited electron and phonon systems.

Pump-probe experiments are powerful methods to probe such excited states. In the pump-probe approach, an ultrashort laser (pump) pulse photoexcites the material and a probe pulse (e.g. laser light, electrons) probes the coupling between the subsystems of the material (e.g. electrons, lattice, spin). In particular, the technique of femtosecond electron diffraction (FED) [7–9] is used to study electron-phonon coupling (EPC) and phonon-phonon coupling (PPC) in materials by measuring directly the lattice dynamics after photo excitation. Early FED experiments mostly focused on the analysis of elastic scattering signals (via the Debye-Waller effect) [10–12], which provide a stable but momentum-integrated view on the lattice dynamics. At that stage, most techniques were not able to extract the time-resolved diffuse scattering signals contained in the data, because of insufficient signal-to-noise ratios. This has changed over the last few years, and current FED experiments have reached sufficient stability to enable a time- and momentum-resolved analysis of phonon dynamics. Such analysis is the focus of this thesis. In particular, we wish to explore the extent to which a branch-resolved view of phonon dynamics can be additionally extracted from FED data.

To place our work in context, we briefly discuss the various ways in which phonons dynamics can be probed. Optical spectroscopy techniques e.g. time-resolved Raman and Brillouin spectroscopies, provide an energy-resolved view on the phonon dynamics, however they are restricted to zero-momentum phonons [13, 14]. The recent developments of ultrafast x-ray diffuse scattering (UXDS) provided a first method to probe the momentum-resolved lattice dynamics over a wide range within the Brillouin zone (BZ) [15, 16]. Due to the low intensity of diffuse signals compared to elastic signals, UXDS experiments rely on the high brightness of the beam source. A clear advantage of UXDS is the excellent reciprocal space resolution. However, UXDS experiments suffer from the weak interaction of photons with the lattice. They also are bound to having access to large x-ray facilities.

Similar developments in FED opened the field of femtosecond electron diffuse scattering (FEDS) [17–21]. While the coherence of the electron beam is low compared to x-rays, FEDS experiments have a number of advantages. Besides their laboratory scale setups, they benefit from the strong interaction of beam electrons with the sample atoms. High

¹Interactions with the spin system are not discussed, since they are not relevant for this thesis.

electron energies allow measurements over many BZs due to their flat Ewald sphere. The simultaneous extraction of elastic and diffuse scattering signals additionally helps the interpretation of the delicate diffuse signals on the basis of the stable elastic signals.

In this thesis we combine FEDS and ab initio simulations to study the momentum- and partially branch-resolved lattice dynamics in photo-excited MoS₂, following an approach presented for graphene Ref. [20]. Section 3 gives a detailed description of the diffraction theory necessary to describe the elastic and diffuse scattering signals observed in the FEDS experiments. Additionally, the branch-resolved approach, that combines simulations and FEDS signals in an equation system, is introduced and we discuss the central approximations of this approach and their implications. The combination of the simulations and FEDS signals uses the least squares method. An algebraic description of the regression theory for the specific case of the least-squares method is given in Section 4. We focus on the discussion of multicollinearity in the equation system and its detection, as it plays a central role for the applicability of the branch-resolved approach. In Section 5 we present an overview of the material properties of MoS₂ that are necessary to describe the lattice dynamics after photoexcitation. Additionally we provide the simulated branch-resolved diffuse scattering patterns and their calculation parameters. In Section 6 we extend the original approach of Ref. [20] by introducing a self-consistency test that is used to verify the quality and trustworthiness of results. We apply the self-consistency test on graphene and introduce a phonon branch binning method to reduce the negative effects of multicollinearity. Section 7 provides an overview of the experimental methods used to study the momentum-resolved lattice dynamics in MoS₂, with a focus on the extraction and processing steps of FEDS data developed as part of this thesis. In particular, we present an approach to account for the diffraction pattern distortions in reciprocal space for an exact extraction of diffuse scattering signals. In Sec. 8, we study the momentum integrated phonon dynamics in MoS₂ by analyzing the elastic scattering signals of the Bragg peaks. We also discuss the additionally observed layer-breathing modes in a sub section. We use the results of the elastic scattering signals to extend our analysis to the more delicate diffuse scattering signals as presented in Sec. 9. Finally, in Sec. 10, we apply the branch-resolved approach with the self-consistency test on MoS₂. We discuss a binning of phonon branches into effective branches and the effects of multi-phonon scattering for MoS₂.

This thesis is composed of a computational work with the focus on the implementation of a diffuse scattering analysis pipeline that combines experimental results with first principle calculations. The FED experiments on MoS₂ were conducted by Dr. Hélène Seiler in May 2019 ². The first-principle calculations on MoS₂ were conducted by Dr. Marios Zacharias ³.

²Currently affiliated at the Fritz Haber Institute of the Max Planck Society, Faradayweg 4-6, 14195 Berlin, Germany

³Currently affiliated at the Cyprus University of Technology, previously a postdoctoral researcher at the Fritz-Haber Institut der Max-Planck Gesellschaft

3 Electron diffraction theory

This section presents an overview of the elastic and inelastic scattering theory with a focus on electron scattering from thin crystals. Most parts are based on the scattering theory chapters of Refs. [22–26].

3.1 Diffraction from crystals

In general, the incoming electron beam interacts with crystal atoms via Coulomb forces. To describe the electron beam interaction with the crystal, we start with the discussion of a single electron-atom scattering event. Using the particle-wave duality, electrons can be treated as a wave with a wave function describing the probability of scattering events. The incoming electron is described as a plane wave impinging on a single atom at the scattering center. Similar to Huygens principle, the scattered wave is described by a wavelet with its origin at the scattering center.

Going back to the electron beam crystal interaction, each scattering from the crystal atoms can be described by a wavelet. The resulting diffraction pattern is then the superposition of all wavelets. Here, only coherent scattering is considered, which means that the phase between the different wavelets is preserved. As a result, wavelets can interfere constructively or destructively, leading to the characteristic shape of a diffraction pattern. The diffraction pattern itself reflects the intensity of the beam being proportional to its wave function $I \propto \Psi^* \Psi$.

In order to describe the wave function, we use the first Born approximation. The approximation assumes weak scattering of the incoming wave, i.e. we assume no attenuation of the incoming wave and only single scattering by the material. In the context of electron diffraction theory, this assumption is often referred as *kinematical diffraction theory*. In the first Born approximation, the scattered wave function is written as the Fourier transform of the scattering potential $V(\vec{r})$:

$$\Psi_{\text{scatt}}(\vec{r}) = \frac{-m_e}{2\pi\hbar} \frac{e^{i\vec{k}'\vec{r}}}{|\vec{r}'|} \int V(\vec{r}') \cdot e^{-i\vec{q}\vec{r}'} d\vec{r}'. \quad (1)$$

In this expression, m_e is the electron mass, \hbar the Planck constant, \vec{r} the cartesian coordinates and $\vec{q} = \vec{k}' - \vec{k}$ is the scattering vector, given by the difference of incoming and scattered wave vector \vec{k} and \vec{k}' , respectively. From now on, prefactors in Eq. 1 are ignored for the sake of simplicity. Since scattering from a crystal is considered, the scattering potential is equivalent to the crystal potential. The crystal potential can be separated in atomic $V_{\text{atoms}}(\vec{r})$ and bond $V_{\text{bond}}(\vec{r})$ potentials as follows:

$$V(\vec{r}) = V_{\text{atoms}}(\vec{r}) + V_{\text{bond}}(\vec{r}). \quad (2)$$

Contributions from bonds are ignored, since they constitute typically $< 1\%$ of $V(\vec{r})$ [25]. In a first step, we can use the crystal structure to write the atomic crystal potential as a product of the crystal basis potential with every unit cell. Thus we can write the atomic potential as the autocorrelation of basis potential $V_{\text{basis}}(\vec{r})$ with their unit cell positions:

$$V_{\text{atoms}}(\vec{r}) = \int_{-\infty}^{\infty} V_{\text{basis}}(\vec{r}) \sum_m \delta(\vec{r} - \vec{R}_m) d\vec{r} = V_{\text{basis}}(\vec{r}) \otimes \sum_m \delta(\vec{r} - \vec{R}_m), \quad (3)$$

with \vec{R}_m being the translation vector of the m^{th} unit cell. Eq. 3 is plugged in Eq. 1, giving:

$$\Psi_{\text{scatt}} \propto \int [V_{\text{basis}}(\vec{r}) \otimes \sum_m \delta(\vec{r} - \vec{R}_m)] e^{-i\vec{q}\vec{r}} d\vec{r} = \text{FT}[V_{\text{basis}}(\vec{r}) \otimes \sum_m \delta(\vec{r} - \vec{R}_m)]. \quad (4)$$

Using the convolution theorem, $\text{FT}(A \otimes B) = \text{FT}(A) \cdot \text{FT}(B)$ with $\text{FT}()$ being the Fourier transform. Hence we can rewrite Eq. 4 as:

$$\Psi_{\text{scatt}} \propto \text{FT}[V_{\text{basis}}(\vec{r})] \cdot \text{FT}[\sum_m \delta(\vec{r} - \vec{R}_m)]. \quad (5)$$

The right term is simplified by applying the Fourier integral to the delta function, that is known as the **shape factor**[22]:

$$\text{FT}[\sum_m \delta(\vec{r} - \vec{R}_m)] = \sum_m e^{-i\vec{q}\vec{R}_m}. \quad (6)$$

Plugging this expression into Eq. 5 gives:

$$\Psi_{\text{scatt}} \propto \text{FT}[V_{\text{basis}}(\vec{r})] \cdot \sum_m e^{-i\vec{q}\vec{R}_m}. \quad (7)$$

As the basis potential is the sum of all atoms in the basis, we can write the basis potential as an autocorrelation of the atomic potential and the atom positions of the basis (all atoms within the unit cell), analogous to what we did in Eq. 3:

$$V_{\text{basis}}(\vec{r}) = \sum_{\nu} V_{\nu}(\vec{r}) \otimes \delta(\vec{r} - \vec{\tau}_{\nu}), \quad (8)$$

where $\vec{\tau}_{\nu}$ is the position of atom ν in the basis and V_{ν} a potential from a single atom. We can substitute this expression in Eq. 7 and apply the convolution theorem once more. After simplifying the delta function in the Fourier integral we get:

$$\Psi_{\text{scatt}} \propto \sum_m \sum_{\nu} \text{FT}[V_{\nu}(\vec{r})] \cdot e^{-i\vec{q}(\vec{R}_m + \vec{\tau}_{\nu})}. \quad (9)$$

The Fourier transforms of the atomic potentials are equivalent to the atomic form factors $\text{FT}(V_{\nu}(\vec{r})) = f_{\nu}(\vec{q})$ and are not discussed in detail, since they are well known. Thermal atomic motions are taken into account by transforming $\vec{\tau}_{\nu} \rightarrow \vec{\tau}_{\nu} + \Delta\vec{\tau}_{\nu,m}(t)$, where $\Delta\vec{\tau}_{\nu,m}(t)$ is the atomic displacement of the ν^{th} atom in the m^{th} unit cell at a given time t . The index m accounts for the fact that atomic displacements are different in every unit cell. Since diffraction experiments usually record a time integrated signal, we perform an additional time averaging of $\Delta\vec{\tau}_{\nu,m}(t)$. The time-averaged scattering potential is given by:

$$\langle \Psi_{\text{scatt}} \rangle_t \propto \sum_m \sum_{\nu} f_{\nu}(\vec{q}) \cdot e^{-i\vec{q}(\vec{R}_m + \vec{\tau}_{\nu})} \langle e^{-i\vec{q}\Delta\vec{\tau}_{\nu,m}} \rangle_t. \quad (10)$$

The exponential term containing the atomic displacement can be simplified using the Bloch theorem:

$$\langle e^{-i\vec{q}\Delta\vec{\tau}_{\nu,m}} \rangle_t = e^{-\frac{1}{2}\langle (\vec{q}\Delta\vec{\tau}_{\nu,m})^2 \rangle_t}. \quad (11)$$

In some literature the dependence of atomic displacements on the unit cells m and basis atoms ν is simplified by using an atomic mean displacement $\Delta\vec{\tau}_\nu$ [25] (only m) or $\Delta\vec{\tau}$ [23] (both). From the resulting wave function we can determine the total scattering intensity via $I \propto \Psi_{\text{scatt}}^* \Psi_{\text{scatt}}$:

$$I(\vec{q}) \propto \sum_{m,m'} \sum_{\nu,\nu'} f_\nu(\vec{q}) f_{\nu'}(\vec{q}) e^{-i\vec{q}(\vec{R}_m - \vec{R}_{m'} + \vec{\tau}_\nu - \vec{\tau}_{\nu'})} \times e^{-\frac{1}{2}\langle(\vec{q}^2[\Delta\vec{\tau}_{\nu,m}^2 - \Delta\vec{\tau}_{\nu',m'}^2])\rangle_t} \quad (12)$$

Equation 12 represents the elastic scattering and inelastic phonon scattering intensity in momentum space. Using the atomic mean displacement, the last exponential term can be written as:

$$I(\vec{q}) \propto \sum_{m,m'} \sum_{\nu,\nu'} f_\nu(\vec{q}) f_{\nu'}(\vec{q}) e^{-i\vec{q}(\vec{R}_m - \vec{R}_{m'} + \vec{\tau}_\nu - \vec{\tau}_{\nu'})} \times e^{-\vec{q}^2\langle\Delta\vec{\tau}^2\rangle_t} \quad (13)$$

where $\langle\Delta\vec{\tau}^2\rangle_t$ is referred as the time-average **atomic mean square displacement** (MSD). This formulation is only useful if atomic motions should be calculated directly and not further used.

3.1.1 Scattering intensity and phonons

In order to combine DFPT calculations and experimental FED data, we have to bring Eq. 12 into a form that depends on the parameters accessible with DFPT. These parameters are the phonon frequencies $\omega_{\vec{k},j}$ and complex phonon polarization vectors $\vec{e}_{j,\nu,\vec{k}}$ of the j^{th} phonon branch and ν^{th} atom at the reduced scattering vector \vec{k} . In the limit of the harmonic approximation, the thermal atomic displacements $\Delta\tau_{m,\nu}$ can be written as a superposition of all phonon modes [27]:

$$\Delta\vec{\tau}_{m,\nu} = \text{Re} \frac{1}{\sqrt{\mu_\nu}} \sum_{\vec{k},j} \{a_{\vec{k},j} \vec{e}_{\vec{k},j,\nu} \times \exp[i\vec{k}(\vec{R}_m + \vec{\tau}_\nu) - i\omega_{\vec{k},j}t - i\phi_{\vec{k},j}]\}. \quad (14)$$

Where μ_ν is the atomic mass, $a_{j,\vec{k}}$ the phonon mode amplitude, $w_{j,\vec{k}}$ the mode frequency and $\phi_{j,\vec{k}}$ a random phase factor, which accounts for the fact that there are no phase relations between the modes.

Inserting equation 14 in the exponential term of equation 12 gives:

$$-\frac{1}{2}\langle(\vec{q}[\Delta\vec{\tau}_{m,\nu} - \Delta\vec{\tau}_{m',\nu'}])^2\rangle_t = M_\nu + M_{\nu'} - \sum_{\vec{k},j} \frac{|a_{\vec{k},j}|^2}{2\sqrt{\mu_\nu\mu_{\nu'}}} \left\{ (\vec{q} \cdot \vec{e}_{\vec{k},j,\nu})^* (\vec{q} \cdot \vec{e}_{\vec{k},j,\nu'}) \times \exp \left[i\vec{k} \cdot (\vec{R}_m - \vec{R}_{m'} + \vec{\tau}_\nu - \vec{\tau}_{\nu'}) \right] \right\}. \quad (15)$$

Here we used that summing over all random phases $\phi_{\vec{k},j}$ time averages to zero. M_ν is defined as the **Debye-Waller factor** (DWF):

$$M_\nu = \frac{1}{4\mu_\nu} \sum_{\vec{k},j} |a_{\vec{k},j}|^2 \left| \vec{q} \cdot \vec{e}_{\vec{k},j,\nu} \right|^2. \quad (16)$$

The phonon mode amplitudes can be directly related to the phonon mode populations by evaluating the kinetic energy of the phonon system in the picture of the harmonic oscillator system. Plugging the atomic displacement (Eq. 14) into the kinetic energy term gives:

$$\begin{aligned}\langle KE \rangle &= \frac{1}{2} \sum_{m,\nu} \mu_\nu \langle \dot{\vec{r}}_{\nu,m}^2 \rangle \\ &= \frac{N}{4} \sum_{\vec{k},j} |a_{\vec{k},j}|^2 \omega_{\vec{k},j}^2,\end{aligned}\quad (17)$$

where N is the number of unit cells. The total mean energy of the phonon system is equal to the sum over all phonon mode energies:

$$\langle E \rangle = 2\langle KE \rangle = \sum_{\vec{k},j} \hbar \omega_{\vec{k},j} \left(n_{j\vec{k}} + \frac{1}{2} \right). \quad (18)$$

Comparing equations 17 and 18 gives:

$$|a_{\vec{k},j}|^2 = \frac{2\hbar}{N\omega_{\vec{k},j}} \left(n_{j\vec{k}} + \frac{1}{2} \right). \quad (19)$$

Combining equation 15 with equation 19, we can write the scattering intensity in Eq. 12 as a function of lattice parameters, phonon frequencies, polarization vectors and phonon populations, giving:

$$\begin{aligned}I(\vec{q}) &\propto N \sum_m \sum_{\nu,\nu'} \{ f_\nu f_{\nu'} \exp(-M_\nu - M_{\nu'}) \\ &\quad \times \exp[-i\vec{q} \cdot (\vec{R}_m + \boldsymbol{\tau}_{\nu,\nu'})] \exp[P_{m,\nu,\nu'}(\vec{q})] \},\end{aligned}\quad (20)$$

with the phononic factor:

$$\begin{aligned}P_{m,\nu,\nu'}(\vec{q}) &= \frac{\hbar}{N\sqrt{\mu_\nu\mu_{\nu'}}} \sum_{\vec{k},j} \frac{(n_{\vec{k},j} + \frac{1}{2})}{\omega_{\vec{k},j}} (\vec{q} \cdot \vec{e}_{\vec{k},j,\nu})^* (\vec{q} \cdot \vec{e}_{\vec{k},j,\nu'}) \\ &\quad \times \exp[i\vec{k} \cdot (\vec{R}_m + \boldsymbol{\tau}_{\nu,\nu'})].\end{aligned}\quad (21)$$

The phononic factor accounts for all phonon contributions to the diffraction pattern. For a further simplification of the intensity, the phononic factor can be expressed in a Taylor series:

$$\exp(x) = 1 + x + x^2/2 + \dots, \quad (22)$$

$$I(\vec{q}) = I_0 + I_1 + I_2 + \dots \quad (23)$$

The first term of the series, I_0 , reflects the intensity from no interaction with phonons. The second term, I_1 , reflects the intensity from one-phonon scattering. All higher order terms are treated as multi-phonon scattering terms. Plugging the Taylor series in equation 20 gives:

$$I_0 \propto N \sum_{m,\nu,\nu'} \{ f_\nu f_{\nu'} \exp(-M_\nu - M_{\nu'}) \times \exp[-i\mathbf{q} \cdot (\vec{R}_m + \vec{\tau}_{\nu,\nu'})] \}, \quad (24)$$

$$I_1 \propto N \sum_{m,\nu,\nu'} \{f_\nu f_{\nu'} \exp(-M_\nu - M_{\nu'}) \exp[-i\vec{q} \cdot (\vec{R}_m + \vec{\tau}_{\nu,\nu'})] P_{m,\nu,\nu'}(\vec{q})\}, \quad (25)$$

$$I_2 \propto \frac{N}{2} \sum_{m,\nu,\nu'} \{f_\nu f_{\nu'} \exp(-M_\nu - M_{\nu'}) \times \exp[-i\vec{q} \cdot (\vec{R}_m + \vec{\tau}_{\nu,\nu'})] [P_{m,\nu,\nu'}(\vec{q})]^2\}. \quad (26)$$

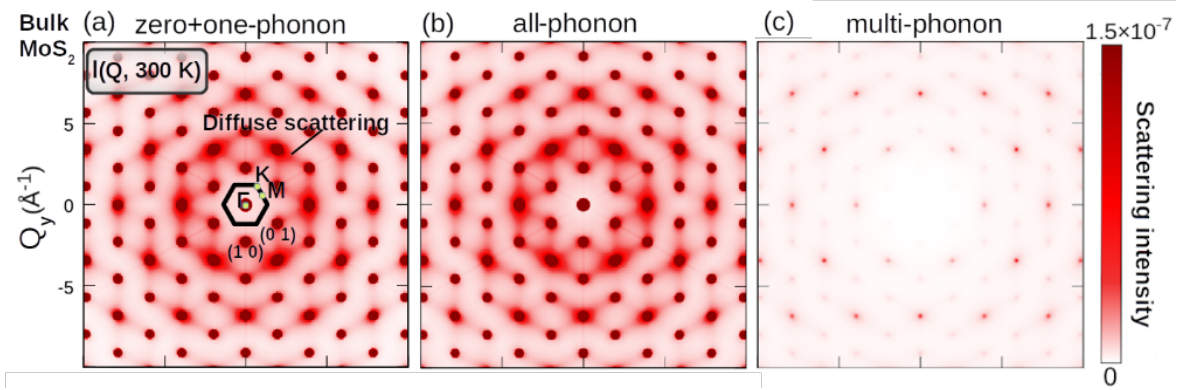


Figure 1: Calculated a) zero+one-phonon ($I_0(\vec{q}) + I_1(\vec{q})$), b) all-phonon ($I(\vec{q})$) and c) multi-phonon contribution ($I_{\text{all}}(\vec{q}) = I(\vec{q}) - I_0(\vec{q})$) of bulk MoS₂ for $T = 300$ K. Black hexagon indicates the first BZ with high symmetry points and Miller indices of Bragg reflections. Figure from [28].

The expressions of I_0 and I_1 are essential to understand the experimental signals presented in this thesis, and they are described in more detail in the next sub-sections. Figure 1 shows exemplary patterns of the calculated zero plus one-phonon contribution (a), all-phonon contribution (b) and multi-phonon contribution (c) of MoS₂.

3.1.2 Elastic scattering

The shape factor (first term) of equation 6, I_0 , can be simplified using the sum rule:

$$S(\vec{q}) = \sum_m \exp(i\vec{q} \cdot \vec{R}_m) = N \delta_{\vec{q}, \vec{G}}, \quad (27)$$

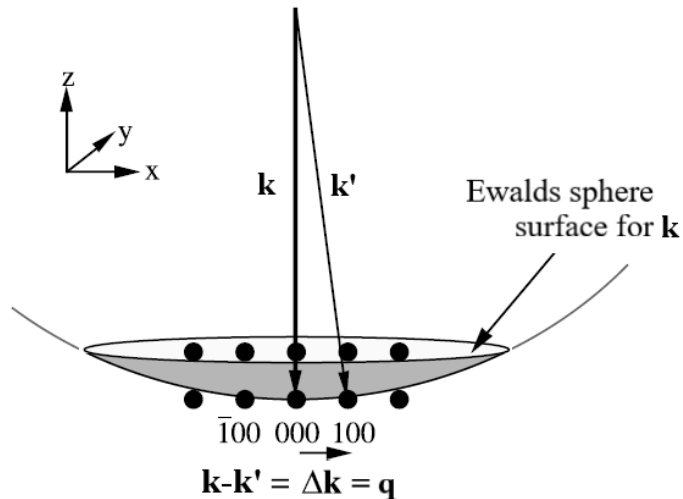
where \vec{G} is a reciprocal lattice vector. The sum rule is only valid for very large crystals due to peak narrowing [22]. A discussion of the shape factor for finite crystal dimensions can be found in Sec. 3.1.4. We find the **elastic scattering intensity**:

$$I_0(\vec{q}) \propto N^2 \sum_{\nu,\nu'} \{f_\nu f_{\nu'} \times \exp(-M_\nu - M_{\nu'}) \exp[-i\vec{q} \cdot (\vec{\tau}_\nu - \vec{\tau}_{\nu'})] \delta_{\vec{q}, \vec{G}_{hkl}}\}. \quad (28)$$

The elastic scattering term consists of the **structure factor**:

$$F(\vec{q}) = \sum_\nu f_\nu \exp(-i\vec{q} \cdot \vec{\tau}_\nu), \quad (29)$$

Figure 2: Ewald's sphere for an incoming and scattered electron beam with wave vector \mathbf{k} and \mathbf{k}' respectively, illustrating the Laue condition. Whenever the scattering vector $\mathbf{q} = \mathbf{G}$ (black dots) both beams interfere constructively and generate a Bragg reflection. Figure edited from [22].



and exponential terms $\sum_{\nu} \exp(-M_{\nu})$ containing the DWF. The $\delta_{\vec{q}, \vec{G}_{hkl}}$ term implies the Laue condition (Fig. 2), only producing non-zero intensities if $\vec{q} = \vec{G}_{hkl}$. The resulting peaks are known as **Bragg peaks**.

Using these expressions, we can also determine the more general and widely used expression of the elastic scattering intensity as a function of atomic MSD. Starting from Eq. 13 we can proceed with analog steps (for more details see [23]) giving the following expression:

$$I_0(\vec{q}) \propto N^2 \cdot F(\vec{q})F(\vec{q})^* \times e^{-\vec{q}^2 \langle \Delta \tau^2 \rangle_t} \delta_{\vec{q}, \vec{G}_{hkl}}. \quad (30)$$

The Bragg peak intensities depend on the phonon populations via the DWF. Due to the sum over all phonon modes in the phonon amplitudes, the DWF reflects the momentum and branch integrated phonon populations. An increase in temperature leads to an increase of phonon populations, which results in an increase of the DWF and thus in a decrease of Bragg peak intensities. The intensity loss of Bragg peaks is redistributed in a diffuse background between the peaks, described by the one- and multi-phonon contributions introduced in equations 25 and 26. The next sub-section focuses on I_1 as it is used in the branch- and momentum-resolved approach.

3.1.3 Inelastic scattering

In this thesis, we analyse the inelastic scattering signals assuming that they are well-described by the one-phonon contribution I_1 . Hence we neglect all higher-order multi-phonon processes. The intensity of multi-phonon interactions can be retrieved by calculating $I_{\text{multi}} = I(\vec{q}) - I_0 - I_1$ [26], but this goes beyond the scope of this thesis. Similar to the elastic scattering term, we can simplify the expression of I_1 . Evaluating Eq. 25 with the phononic factor gives:

$$I_1 \propto \hbar \sum_{m, \nu, \nu'} \frac{f_{\nu} f_{\nu'}}{\sqrt{\mu_{\nu} \mu_{\nu'}}} \exp(-M_{\nu} - M_{\nu'}) \exp \left[i(\vec{k} - \vec{q}) \cdot (\vec{R}_m + \vec{\tau}_{\nu, \nu'}) \right] \\ \times \sum_{\vec{k}, j} \frac{(n_{\vec{k}, j} + \frac{1}{2})}{\omega_{\vec{k}, j}} (\vec{q} \cdot \vec{e}_{\vec{k}, j, \nu})^* (\vec{q} \cdot \vec{e}_{\vec{k}, j, \nu'}). \quad (31)$$

The expression is further simplified using the sum rule in Eq. 27 and

$\vec{e}_{\vec{k}+\vec{G},j,\nu} = \vec{e}_{\vec{k},j,\nu} \exp(-i\vec{G} \cdot \vec{\tau}_\nu)$. Additionally we write the time dependency of the phonon populations and phonon frequencies so that $n_{j,\vec{k}} \rightarrow n_{j,\vec{k}}(t)$ and $\omega_{j,\vec{k}} \rightarrow \omega_{j,\vec{k}}(t)$. Generally phonon frequencies are time-dependent as they can change after photoexcitation due to anharmonic effects. Thus we can write the final compact form of the **one-phonon contribution (OPC)** to inelastic scattering with its temporal dependency:

$$I_1(\vec{q}, t) \propto N \sum_j \frac{n_{j,\vec{k}}(t) + 1/2}{\omega_{j,\vec{k}}(t)} |F_{1j}(\vec{q}, t)|^2, \quad (32)$$

where $|F_{1j}(\vec{q}, t)|^2$ is the **one-phonon structure factor (OPSF)** for phonon branch j :

$$|F_{1j}(\vec{q}, t)|^2 = \left| \sum_\nu e^{-M_\nu(\vec{q}, t)} \frac{f_\nu(\vec{q})}{\sqrt{\mu_\nu}} \left(\vec{q} \cdot \vec{e}_{j,\nu,\vec{k}} \right) \right|^2. \quad (33)$$

The sum over all branches j allows us to separate the individual branch contributions of the OPC. Phonon population changes are directly reflected in the individual sums and the DWFs of the OPSFs. Because phonon frequencies appear in the denominator of the OPC expression, low energy phonons generate more intensity for equal population changes than high energy phonons. The product between the scattering vector and phonon polarization vectors in the OPSF is the leading term in the OPC and generates most of the features in the inelastic diffraction pattern. The DWF produces an attenuation of the OPC for larger scattering vectors.

3.1.4 Thin film effect

In this section we rewrite the simplified shape factor $S(\vec{q})$ in Eq. 27 to account for finite crystal dimensions in the scattering intensity. So far we assumed very large crystal dimensions, which lead to sharp intensity maximas whenever the Laue condition is fulfilled. The scattering intensity introduced in Eq. 28 features a factor of $N^2 = (N_x^2 \cdot N_y^2 \cdot N_z^2)$, where N is the number of unit cells and $N_{i=x,y,z}$ the number of unit cells along axis i . In order to treat the electron scattering in the framework of kinematical scattering theory, the crystal thickness has to be reduced to a thickness smaller than the mean free path of the electrons [24]. This results in a drastic reduction of the number of unit cells along the electron beam axis.

In a lengthy derivation [22] it could be shown that the shape factor product $S(\vec{q})^* S(\vec{q})$ and the diffraction intensity can be written as:

$$I(\vec{q}) \propto S(\vec{q})^* S(\vec{q}) = \prod_{i=x,y,z} \frac{\sin^2(\pi q_i a_i N_i)}{\sin^2(\pi q_i a_i)}, \quad (34)$$

where q_i is a scattering vector component and a_i the lattice constant of direction i .

In the experimental setup we use samples that have large numbers of unit cells in the in-plane directions (x,y) and only a few unit cells in the beam direction (z). For large numbers of unit cells, the single in-plane terms converge to the know prefactors $N_x^2 \cdot N_y^2$,

giving the shape factor product:

$$I(\vec{q}) \propto S(\vec{q})^* S(\vec{q}) = N_x^2 \cdot N_y^2 \cdot \frac{\sin^2(\pi q_z a_z N_z)}{\sin^2(\pi q_z a_z)}. \quad (35)$$

The modification of the shape factor due to finite crystal dimensions is known as the

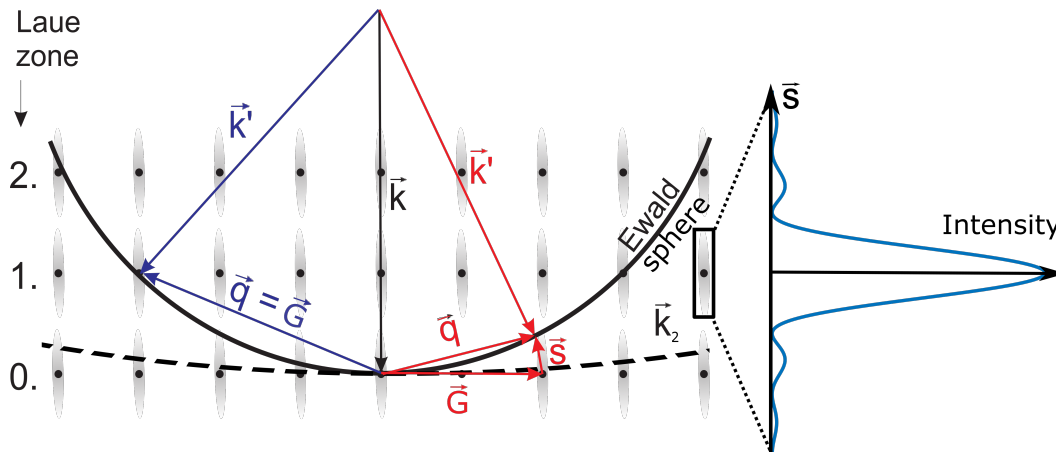


Figure 3: Ewald's sphere with the thin film effect. Blue scattering vectors indicate the case of a perfectly fulfilled Laue condition ($\vec{q} = \vec{G}$) in the first order Laue zone (FOLZ). Red scattering vectors show the case of the Ewald's sphere cutting the relrod ($\vec{q} = \vec{G} + \vec{s}$) in the zero order Laue zone (ZOLZ). The inset shows the intensity profile of a relrod (grey) as a function of deviation vector \vec{s} . The dashed line indicates an Ewald's sphere for higher electron energies $k_2 > k$. Figure edited from [29]

thin film effect. Its effect on the Ewald's sphere is shown in Fig. 3. The finite crystal dimensions lead to a softening of the Laue condition, allowing beams with $\vec{q} = \vec{G} + \vec{s}$, where \vec{s} is the deviation vector, to generate intensity. For thin films this leads to a strong softening of the Laue condition in one direction, which are often mentioned as 'relrods' in reciprocal space. The Ewald's sphere of high energy beams with electron energies in the keV-regime can thus cut many relrods and generate more Bragg peaks than a lower energy beam in the eV-regime. The experimental setup used in this work operates at electron energies of 80 - 100 keV. Thus the wave vector of the beam is much larger than the reciprocal lattice vectors, $\vec{G} \ll \vec{k}$.

3.2 The time-, momentum- and branch-resolved approach

The goal of this thesis is to study the time-, momentum- and branch- resolved phonon dynamics of MoS₂ with the approach first presented in Ref. [20]. For this, we combine the extracted time- and momentum-resolved inelastic scattering intensities from the experiment with the results of ab initio calculations. In this sub-section, we provide an overview of the approach, and its application to MoS₂ will be described in detail in Sec. 10.

Starting with Eq. 32, we replace the time dependence with the pump-probe delay $t \rightarrow \Delta t$. Additionally we make two approximations: i) we neglect the temperature dependence of the phonon frequencies. Such modulations arise from anharmonicities,

which are not expected for the temperatures changes in the experiment [30, 31]. Hence we can write $\omega_{j,\vec{k}}(\Delta t) \approx \omega_{j,\vec{k}}$. ii) We neglect temperature changes in the OPSF due to changes in the DWF's, giving $|F_{1j}(\vec{q}, \Delta t)|^2 \approx |F_{1j}(\vec{q})|^2$. A further discussion of this approximation is presented in Sec. 3.2.1. Thus the OPC can be written as:

$$I_1(\vec{q}, \Delta t) \propto N \sum_j \frac{n_{j,\vec{k}}(\Delta t) + 1/2}{\omega_{j,\vec{k}}} |F_{1j}(\vec{q})|^2. \quad (36)$$

Phonon dynamics are observed by considering the phonon population changes $\Delta n_{j,\vec{k}}$ in the one-phonon intensity differences $\Delta I_1(\vec{q}, \Delta t)$:

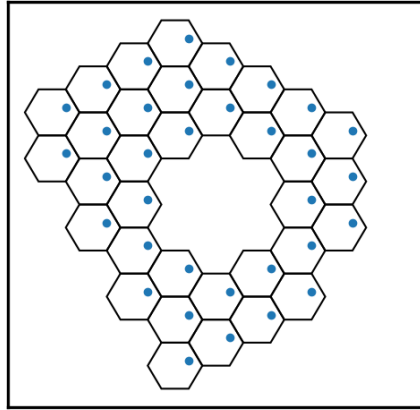
$$\Delta I_1(\vec{q}, \Delta t) = \lambda \cdot \sum_j \Delta n_{j,\vec{k}}(\Delta t) \frac{|F_{1j}(\vec{q})|^2}{\omega_{j,\vec{k}}}, \quad (37)$$

where λ summarizes all prefactors.

The idea of this approach is that the left side of Eq. 37 is available from the experiment and $|F_{1j}(\vec{q})|^2 / \omega_{j,\vec{k}}$ is calculated by ab initio calculations. In such case, λ is equivalent to a scaling factor that merges the magnitudes of experimental and calculated intensity differences. We will describe this merging procedure in detail for the case of MoS₂ in Sec. 10.4.

As the $\Delta n_{j,\vec{k}}$'s are redundant in every Brillouin zone (BZ), we can group the scattering vectors \vec{q} in groups with the same reduced reduced scattering vector \vec{k} . This gives a set $i \in [1, \dots, M]$ of scattering vectors $\vec{q}_i = \vec{k} + \vec{G}_i$, where \vec{G}_i is the reciprocal lattice vector from the nearest Bragg peak reflection. The positions of an exemplary scattering vector set \vec{q}_i are shown in Fig. 4. The number of BZ's M is limited by the experimental conditions (for instance the size of the detector or magnetic lens settings).

Figure 4: Positions of a scattering vector set \vec{q}_i with similar reduced scattering vectors \vec{k} for the MoS₂ data set. BZ's are indicated by black hexagons.



For every reduced scattering vector \vec{k} we can then write a linear equation system with every row consisting of Eq. 37 at the scattering vectors \vec{q}_i :

$$\vec{I}_{\vec{k}}(\Delta t) = \vec{F}_{\vec{k}} \vec{n}_{\vec{k}}(\Delta t), \quad (38)$$

where:

$$\vec{I}_{\vec{k}}(\Delta t) = \frac{1}{\lambda} \left[\Delta I(\vec{k} + \vec{G}_1, \Delta t), \dots, \Delta I(\vec{k} + \vec{G}_M, \Delta t) \right]^T, \quad (39)$$

$$\vec{n}_{\vec{k}}(t) = \left[\Delta n_{1,\vec{k}}(t), \dots, \Delta n_{N,\vec{k}}(t) \right]^T, \quad (40)$$

$$\vec{\bar{F}}_{\vec{k}} = \begin{bmatrix} |F_{11}(\vec{k} + \vec{G}_1)|^2 / \omega_{1,\vec{k}} & \dots & |F_{1N}(\vec{k} + \vec{G}_1)|^2 / \omega_{N,\vec{k}} \\ \vdots & \ddots & \vdots \\ |F_{11}(\vec{k} + \vec{G}_M)|^2 / \omega_{1,\vec{k}} & \dots & |F_{1N}(\vec{k} + \vec{G}_M)|^2 / \omega_{N,\vec{k}} \end{bmatrix}_{M \times N}. \quad (41)$$

The matrix $\vec{\bar{F}}_{\vec{k}}$ has the size $M \times N$, where N is the number of phonon branches. As a solution, we get the phonon population change $\Delta n_{j,\vec{k}}(\Delta t)$ for every phonon branch j , reduced scattering vector \vec{k} and pump-probe delay Δt (branch-, momentum- and time-resolution respectively).

From linear Algebra we know that a solution can only exist if $M > N$. Hence we have to consider more BZs than the material has phonon branches. In our case, $N = 18$ since MoS₂ has 6 atoms in the primitive unit cell. Solving the equation system is similar to finding a best phonon population change $\Delta n_{j,\vec{k}}(t)$ for every branch, such that the sum of all one-phonon branch contributions matches the observed signal $\Delta I_1(\vec{k}, \Delta t)$ best. This approach uses the \vec{q} -dependence of $|F_{1j}(\vec{q})|^2$ and assumes that the magnitudes of branch contributions can be well separated in momentum space. Usually the more BZs are considered the more different are the branch contributions and the more different are the columns. A problem arises if the OPSFs of different phonon branches have similar magnitude ratios for the scattering vector set \vec{q}_i . Then we cannot distinguish the branch contributions at that reduced scattering vector \vec{k} . The effect of similar branch contributions, or columns in the equation system, is formally described by the effects of multicollinearity and are further discussed extensively in Sec. 4.2 and 6. We will see throughout this thesis that multicollinearity is a major limitation of the branch-resolved approach. In the context of the experiments, this implies that if only a few non- or less-multicollinear branches show strong phonon population changes. We can thus better assign the populations changes to the branches, as they can be better distinguished. This situation is in general more likely in highly non-equilibrium situations than in near-thermal equilibrium, where all branches show population changes.

3.2.1 Approximations

The central approximation of the method in Ref. [20] is to treat the OPSF as a time independent function, $F_{1,j}(\vec{q}, t) \approx F_{1,j}(\vec{q}, t = t_0)$. This allows to transform the intensity changes of the one-phonon contribution $\Delta I_1(\vec{q}, \Delta t)$ into the equation system of Eq. 38. The general assumption is that the relative changes in phonon populations due to the laser pulse excitation, $\Delta n_{j,\vec{k}}(\Delta t)$, are much larger than the changes in the OPSF, $\Delta F_{1,j}(\vec{q}, \Delta t)$. The time dependence of the OPSF is equivalent to a lattice temperature dependence. As can be seen in Eq. 33, the OPSF depends directly on the lattice temperature via the DWF and decreases if the lattice temperature increases. Since we observe that the total inelastic signal increases in the experiments, $\Delta n_{j,\vec{k}}$ has to be the dominating term that drives the net increase in inelastic intensity. This observation underpins the validity of the approximation.

Due to the known $1/w_{j,\vec{k}}$ dependence, changes of the DWF are larger if the populations

of acoustic modes change compared to when the populations of optical modes change. As a consequence, the approximation is more valid in non-equilibrium states, where most population changes appear in the optical branches [12], and gets less valid towards thermal equilibrium.

The validity of the approximation can be controlled by the absorbed fluence. A higher absorbed fluence results in a higher temperature difference between the equilibrium states and thus the approximation is less valid. At the same time, decreasing the fluence also decreases the SNR in the experiments. Hence a trade-off has to be found between absorbed fluence and SNR, which could be interesting to explore in future experiments.

The question remains whether the approach in Ref. [20] under- or overestimates the phonon populations. Here we express the OPC differences (Eq. 37) as a function of temperature T , which is equivalent to the pump-probe delay dependence, $\Delta I_1(\vec{q}, \Delta t) \rightarrow \Delta I_1(\vec{q}, \Delta T)$. The OPC difference without the constant OPSF approximation can be written as:

$$\begin{aligned} \Delta I_1(\vec{q}, \Delta T) &= I_1(\vec{q}, T_2) - I_1(\vec{q}, T_1) \\ &= \lambda \sum_j \frac{n_{j,\vec{k}}(T_2) |F_{1,j}(\vec{q}, T_2)|^2 - n_{j,\vec{k}}(T_1) |F_{1,j}(\vec{q}, T_1)|^2}{w_{j,\vec{k}}}, \end{aligned} \quad (42)$$

with $T_2 > T_1$ and thus:

$$|F_{1,j}(\vec{q}, T_2)|^2 < |F_{1,j}(\vec{q}, T_1)|^2. \quad (43)$$

For now on we neglect the \vec{q} (\vec{k}) dependence for the sake of simplicity. Using Eq. 43 and the relation $n_j(T_1) < n_j(T_2)$ the comparison between the exact denominator of Eq. 42 and the denominator simplified with the constant OPSF approximation gives:

$$\begin{aligned} n_j(T_2) |F_{1,j}(T_2)|^2 - n_j(T_1) |F_{1,j}(T_1)|^2 &< \Delta n_j(\Delta T) |F_{1,j}(T_2)|^2 \\ &< \Delta n_j(\Delta T) |F_{1,j}(T_1)|^2. \end{aligned} \quad (44)$$

This shows that the approximation of a constant OPSF, whether set to the initial or elevated temperature, always overestimates the one-phonon contribution, thus leads to an underestimation of the phonon population changes $\Delta n(\vec{q}, \Delta t)$. Furthermore, since $\Delta n(\Delta T) |F_{1,j}(T_2)|^2 < \Delta n(\Delta T) |F_{1,j}(T_1)|^2$, using the OPSF at the elevated temperature gives the best approximation.

In the context of the experiment, we can interpret the data in a simplifying two-temperature model (TTM) [12] as a set of intensity differences:

$$D = \{\Delta I(\Delta T_1^{\text{eff}}), \dots, \Delta I(\Delta T_m^{\text{eff}})\} \quad (45)$$

at different elevated effective lattice temperatures, where m is the number of pump-probe delay points. Each temperature difference is the difference between the initial temperature (300 K) and the elevated temperature corresponding to a pump-probe delay Δt . Using the TTM results, a best approximation for each pump-probe delay could be obtained by setting the OPSF temperature to the corresponding elevated temperature. Here we simply use a single temperature for the entire set of intensity differences. Since the focus lies on the observation of highly non-equilibrium states, the best constant OPSF approximation is given by the OPSF $|F_{1,j}(T_1)|^2$ at the initial temperature

of D . The underestimation of phonon population changes is then increasing for increasing lattice temperature (pump-probe delays). Setting it to the final temperature of D would result in an overestimation for early pump-probe delays which later evolves to an underestimation for nearly equilibrium states.

In fact, to generalize the approach to both non-equilibrium and equilibrium states, it could be useful to ramp up the OPSF temperature with a biexponential function based on the time constants retrieved from Bragg peak analysis commonly performed in FED experiments and by us in Sec. 8 [32, 33]. At the current stage, this dynamic approximation is not implemented and the calculations presented in this work are all based on the constant OPSF approximation set to the initial temperature.

4 Regression theory

In order to achieve a branch resolution, we have to solve the equation system Eq. 38. Since the system has more rows than columns, it is overdetermined. Such overdetermined problems are usually solved with optimization procedures as no unique solution exists. This chapter presents the mathematical background used in this thesis to solve and understand linear regression problems [34–36].

4.1 Linear overdetermined regression problems

A linear regression problem is defined as a system of n linear equations:

$$\sum_{j=1}^p x_{ij}\alpha_j = y_i \quad \text{with } i = 1\dots n. \quad (46)$$

Where x_{ij} are the predictors and y_i is the response of the i th observation, with the coefficients α_j being unknown with $j = 1\dots p$. This can be written in matrix form:

$$X\vec{\alpha} = \vec{y}, \quad (47)$$

with X being a real $n \times p$ -matrix, $\vec{\alpha}$ a $p \times 1$ -vector and \vec{y} a $n \times 1$ -vector.

In this work, we consider only cases with $n > p$. In that case the equation system is overdetermined and has infinite solutions. Additionally the equations mostly contradict each other and subsequently an exact solution can not be determined. It is then only possible to find a best solution, which minimizes the residuals.

4.2 Least squares method

A suitable approach to solve $n > p$ problems is the least squares optimization method. Using the matrix formulation of equation 47, the residuals can be written as:

$$\vec{r} = \vec{y} - X\vec{\alpha}. \quad (48)$$

The principle of the least square method is to minimize the sum of the squared residuals S :

$$S = \sum_i r_i^2 = \vec{r}^T \vec{r} = \vec{y}^T \vec{y} - 2\vec{\alpha}^T X^T \vec{y} + \vec{\alpha}^T X^T X \vec{\alpha}, \quad (49)$$

in relation to the coefficients α_i . The necessary condition for $S(\vec{\alpha})$ to be a minimum is that the Gradient of S disappears, $\nabla S(\vec{\alpha}) = 0$. This leads to the so called *normal equation*:

$$(X^T X)\vec{\alpha} = X^T \vec{y}. \quad (50)$$

A detailed derivation can be found in [35, 36]. With $A = X^T X$ being a symmetric $p \times p$ -matrix and $\vec{b} = X^T \vec{y}$ being a p -vector, the equation can be written as:

$$A\vec{\alpha} = \vec{b}. \quad (51)$$

This gives a quadratic equation system, which can be solved with the standard algorithms of linear algebra. The solution can be written as:

$$\vec{\alpha} = A^{-1}\vec{b}, \quad (52)$$

presuming that the inverse of A exists. The previous step relies on the calculation of the inverse A^{-1} and fails if an inverse does not exist.

If A is singular matrix and subsequently has no inverse, the least square method cannot be applied. The biggest problem in least square problems comes from the more common case of nearly singular matrices, which are called ill-posed problems. Ill-posed problems lead to unstable solutions with very high variance and often have non unique solutions. This behaviour can be understood by considering the diagonalized form of A . Since A is a real symmetric matrix, it can be decomposed as the following matrix product [35]:

$$A = U \times D \times U^T, \quad (53)$$

where U is a orthonormal matrix fulfilling $UU^T = U^TU = \mathbb{1}$ and D is a diagonal matrix with the eigenvalues λ_i as the diagonal elements D_{ii} .

The inverse is then given by:

$$A^{-1} = U \times D^{-1} \times U^T, \quad (54)$$

with D^{-1} being the inverse diagonal matrix. The diagonal elements of D^{-1} are simply given by $D_{ii}^{-1} = 1/\lambda_i$. In the case of $\lambda_i = 0$, D_{ii}^{-1} gets infinite and the inverse A^{-1} cannot be determined. If λ_i gets very small the diagonal elements become very large. Thus small deviations in the calculation λ_i will introduce a high uncertainty in the calculation of the inverse. In conclusion, A is invertable if all eigenvalues λ_i 's are greater than zero, in which case A becomes positive definite. A matrix A is positive definite if a vector $\vec{x} \notin 0$ exists, which fulfills:

$$\vec{x}^T A \vec{x} > 0. \quad (55)$$

If one or more eigenvalues are zero, A is positive semi definite, which is the case if $\vec{x}^T A \vec{x} = 0$.

With the definiteness condition we can now show, that a multicollinear matrix is also singular. A matrix X is considered multicollinear if more than two columns of X are linearly related to each other. Multicollinearity is given if a vector $\vec{\alpha} \notin 0$ exists such that $X\vec{\alpha} = 0$. If this is plugged in the definiteness condition, equation 55 can be rewritten as:

$$\vec{\alpha}^T A \vec{\alpha} = \vec{\alpha}^T X^T X \vec{\alpha} = (X\vec{\alpha})^T X \vec{\alpha} = 0, \quad (56)$$

showing that the more X becomes multicollinear, the more A becomes semi positive definite and subsequently becomes singular.

4.3 Detection of multicollinearity

As near multicollinearity is a major problem for the least squares methods, how can it be detected? There are several methods for detecting multicollinearity in a linear equation system, such as the variance inflation factor (VIF) [34] or looking at the elements

of the variance-covariance matrix [34], that are strongly affected by multicollinearity. In this work the variance inflation factor is used, which returns a value for every column of an equation system. The value indicates the presence of multicollinearity in relation to all other columns, but does not give the information of which linear combinations of columns of X are causing it.

Correcting multicollinearity goes always hand in hand with eliminating the columns in the matrix X which are causing it. In our specific application, since the columns are given by the OPSF, an elimination or merging of columns is only possible if the physics of the OPSF is preserved. Therefore the reduction of multicollinearity relies on simplification of the physical model and not on a detection of linear combinations. The knowledge of the strength of multicollinearity and thus the use of the VIF is then sufficient, since it tells that a simplification of the physical model is required.

The fundament of the VIF is the coefficient of determination R^2 , which is defined by:

$$R^2 = 1 - \frac{\sum_i (y_i - \hat{y}_i)^2}{\sum_i (y_i - \bar{y}_i)^2} \in [0, 1], \quad (57)$$

where y_i is the observed data of the regression problem $\vec{y} = X\vec{\alpha} + \vec{\epsilon}$ and \hat{y}_i are the estimated solutions of $\vec{y} = X\vec{a}$ with \vec{a} being the estimate of $\vec{\alpha}$. R^2 is used as a general goodness of how much the model fits the solution. The upper sum represents the summed squared residuals and vanishes if the model totally fits the data. The weakness of the R^2 coefficient is that nearly constant values of y_i make the lower sum disappear and R^2 not defined. The VIF of the j -th column is then defined as:

$$\text{VIF}_j = \frac{1}{1 - R_j^2} \in [0, \infty], \quad (58)$$

where R_j^2 is the coefficient of determination of the j th column regressed against all other variables. In terms of the original regression problem $\vec{y} = X\vec{\alpha}$, R_j^2 is the coefficient of determination of the problem:

$$\vec{x}_j = [\vec{x}_1 \dots \vec{x}_{j-1} \vec{x}_{j+1} \dots \vec{x}_p] \vec{\alpha}', \quad (59)$$

where \vec{x}_j are the columns of X and $\vec{\alpha}'$ is the reduced coefficient vector. This is equal to the multicollinearity condition of the previous section. If the column j gets multicollinear to all other columns, R_j^2 becomes one and thus VIF_j becomes large. In the case of no multicollinearity $R_j^2 = 0$ and thus $\text{VIF}_j = 1$.

4.4 Least square algorithms

This sub-section gives a short overview of the least square algorithm used in this project. All of the used algorithms were already implemented in the *Python*-packages *SciPy* or *Scikit-learn*.

Non-negative least square (NNLS) problems are categorized as least square problems with inequality constraints. The problem is defined as:

$$\min_{\vec{\alpha}} \|\vec{y} - X\vec{\alpha}\| \quad \vec{\alpha} \geq 0. \quad (60)$$

The equation system is solved by minimizing the residuals with the constraint $\vec{\alpha} \geq 0$. The non-negative least squares algorithm used in this project is based on the pseudocode from [37], which is included in the *SciPy*-package.

5 Molybdenum disulfide

Molybdenum disulfide (MoS_2) belongs to the group of transition-metal dichalcogenides (TMDCs). TMDCs gained enormous interest due to their interesting properties, which make them possible candidates for various applications in the fields of electronics and opto-electronics such as photodiodes, photovoltaic cells and light-emitting devices [38–40]. In particular, their strong light-matter interaction [41] makes them suitable candidates for light-controlled devices. Such devices can indeed be realized and controlled via coupling to femtosecond light pulses, including transient band-structure modulation [42] and band gap renormalization [43]. Device applications strongly rely on the knowledge of complex and diverse interaction mechanisms between electrons and lattice and their out-of-equilibrium dynamics. To gain insights into these interactions, we study the phonon dynamics in a photo-excited thin film of MoS_2 by employing FEDS.

5.1 Crystal structure

Bulk MoS_2 is a layered material, like graphite, and belongs to the family of 2D-materials. The primitive unit cell contains 2 layers, where each layer consists of three-atom-thick sulfur-molybdenum-sulfur (S-Mo-S) atom stacks, as shown in Fig. 5. The layers are bonded by weak van der Waals interactions, whereas the intralayer bonds are dominated by ionic and covalent interactions. Each single layer forms a honeycomb structure described by a hexagonal lattice. Lattice vectors are:

$$\vec{a}_1 = a \cdot \hat{e}_x, \quad \vec{a}_2 = -\frac{a}{2} \cdot \hat{e}_x + \frac{\sqrt{3}a}{2} \cdot \hat{e}_y, \quad \vec{a}_3 = c \cdot \hat{e}_z, \quad (61)$$

where a is the in-plane, c the out-of-plane lattice constant and \hat{e}_i the Euclidean vectors. Depending on the stacking order, there are three polytypes 1T, 2H and 3R [44]. In this work we study the most common polytype 2H- MoS_2 , which is characterized by a slide shift between two layers giving the stacking order AbA BaB AbA. For 2H- MoS_2 the lattice constants are $a = 3.15 \text{ \AA}$ and $c = 12.30 \text{ \AA}$ [44].

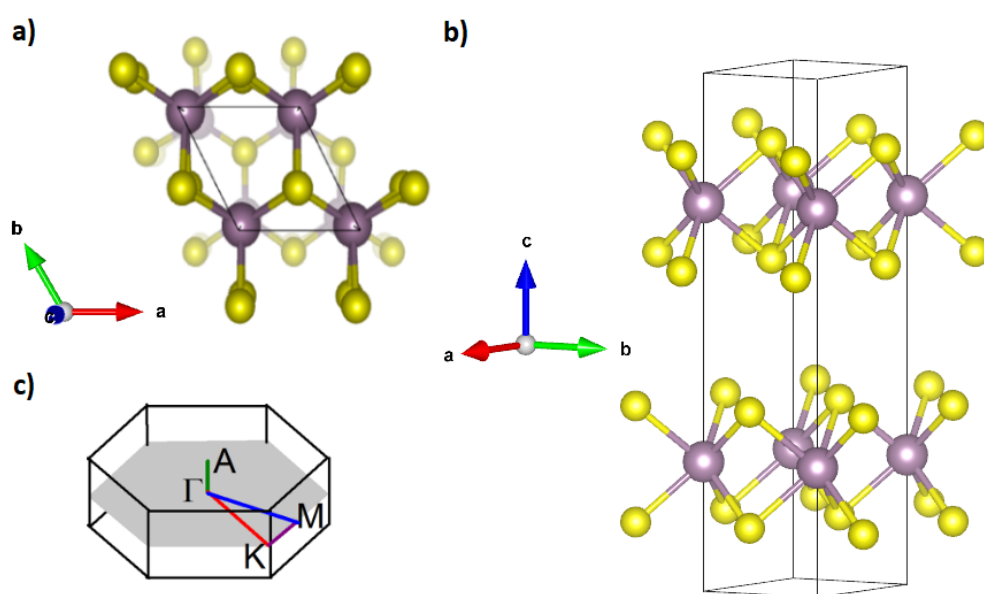


Figure 5: a) Top view (shaded atoms indicate lower layer) and b) Side view of the MoS₂ crystal structure with primitive unit cell. Mo and S atoms are indicated by purple and yellow balls respectively. The crystal structures were generated using the VESTA suite [45]. c) First Brillouin zone of MoS₂ with high-symmetry points labeled (Fig. from [46]).

5.2 Electronic band structure

MoS₂ offers a diverse electronic structure. Besides its indirect band gap and multiple valleys in the conduction band, MoS₂ transforms to a direct band gap semiconductor for monolayer crystals [47], unlike graphene. The electronic band structure of bulk MoS₂ over a high-symmetry path is shown in figure 6. Bulk MoS₂ is a semiconductor with an experimentally measured indirect band gap of 1.3 eV [41, 48] between Γ and its conduction band minimum (CBM) at Λ_{\min} . A direct band gap transition at K is possible if excitation energies are greater than 1.95 eV [49]. Λ_{\min} is located at half the distance between Γ and K. The conduction band offers additional valleys at K and between Γ and M. Especially the K-valley is very close to the CBM, showing an energy difference of only a few meV [50]. For decreasing number of layers, an increasing of the CBM and the highest valence band at K has been observed [50, 51], building out a direct band gap at K for monolayer crystals [52]. The measured energy difference of the valence band maximum (VBM) at Γ and the highest valence band at K is 0.6 eV [53].

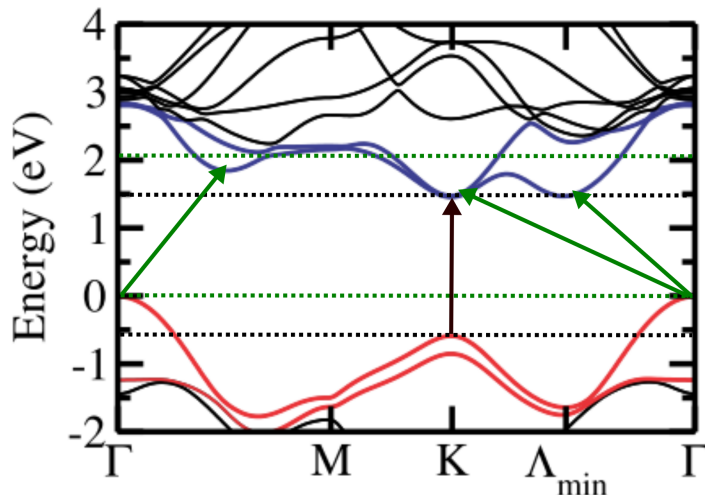


Figure 6: Electronic band structure of bulk MoS₂ (graphics used and modified from [50]) obtained by DFT calculations using the hybrid functional of Heyd, Scuseria, and Ernzerhof (HSE06) and semiempirical D2 method. The dashed lines indicate the electronic excitation windows achieved by our experimental pump photon energy of 2.14 eV. The green and black arrows indicate possible indirect and direct transitions, respectively. The blue bands show the lowest conduction bands and the red bands show the highest valence bands.

With a pump photon energy of 2.14 eV, we are able to drive multiple indirect and direct electronic transitions between the valence and conduction bands, shown as the green and black arrows in Fig. 6, respectively. Note that the calculated electronic band structure shown in this figure overestimates the direct and indirect band gap, compared to the experimental values. Especially the direct K-K transition is 0.19 eV smaller than the experimental gap, indicating that the transition has more available phase space than shown in the figure. Indirect phonon assisted transitions are possible from Γ to most parts of the lowest conduction bands, starting from the Γ -M-valley along the M-K- Λ_{\min} high symmetry line.

5.3 Phonon dispersion

The phonon dispersion of MoS₂ retrieved by density functional perturbation theory (DFPT) calculations along the high-symmetry point line $\Gamma - K - M - \Gamma$ is shown in figure 7. The phonon frequencies and polarization vectors were determined by DFPT as implemented in the *Quantum Espresso* package [54]. All calculations used in this work were performed by Dr. Marios Zacharias⁴. For calculations on MoS₂, we used a fully relaxed primitive unit cell and Hartwigsen-Goedecker-Hutter pseudopotentials [55]. The electronic wave function was determined on a $10 \times 10 \times 3$ \vec{k} -grid by using the plane wave self consistency field module of *Quantum Espresso*. A high accuracy of the wave function was achieved by using an energy cut-off of $E_{cut} = 120$ Ry and a convergence threshold of 1×10^{-9} Ry/Bohr. The dynamical matrices were calculated on a $8 \times 8 \times 2$ \vec{q} -grid using a consistency threshold of 1×10^{-14} .

MoS₂ has $p = 6$ atoms in the primitive unit cell and subsequently $r = 3 \cdot p = 18$

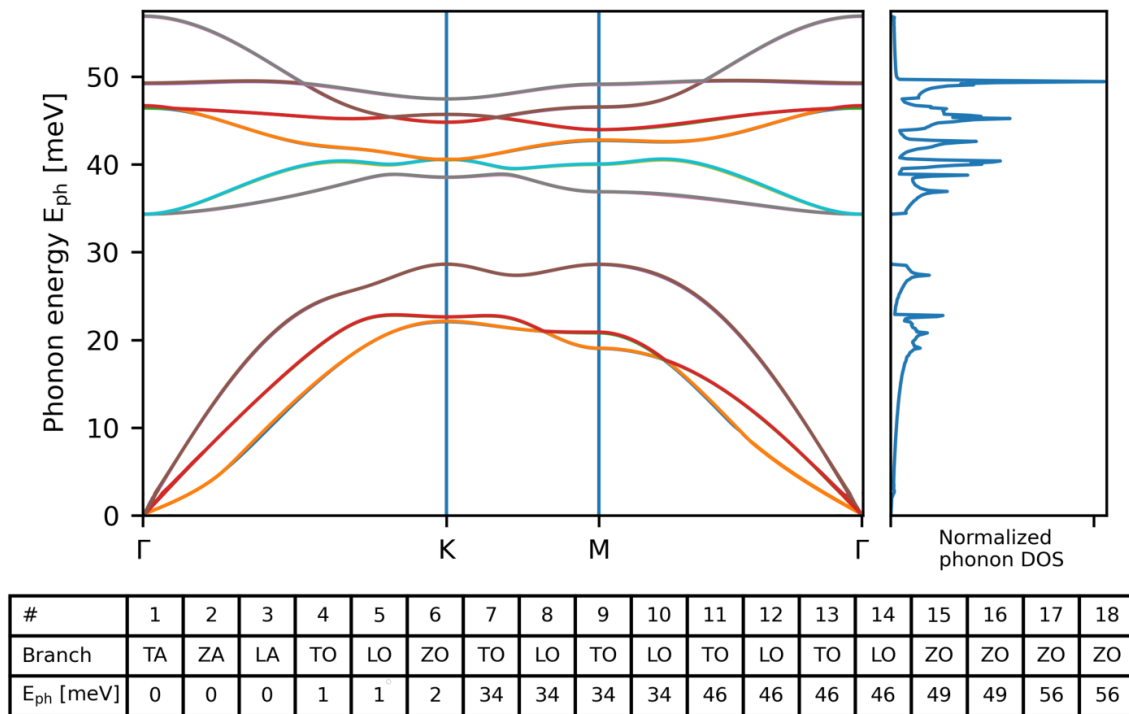


Figure 7: Phonon dispersion of MoS₂ along the $\Gamma - K - M - \Gamma$ path with normalized density of states. The bottom table shows the phonon mode energies at Γ with corresponding branch names and polarization.

phonon branches, 3 acoustic and 15 optical branches. The most remarkable feature of its phonon dispersion is the energy gap between the 6th and 7th branch, separating the branches in 6 low-energy and 12 high-energy branches.

The low-energy section consists of three acoustic and three optical branches, divided in three two-times degenerate pairs. In the high-energy section, all 12 optical branches are two-times degenerate, resulting in 6 overlaid branches. For the determination of the

⁴Currently affiliated at the Cyprus university of technology, previously a postdoctoral researcher at the Fritz-Haber Institut der Max-Planck Gesellschaft

phonon polarization at Γ and the OPSF calculations, phonon polarization vectors are required. The mean polarization of all atoms in the unit cell is shown in the appendix Fig. 43.

The general agreement of all phonon branches with the experimental and theoretical studies carried out by Ref. [46] is very good.

5.4 One-phonon contribution calculations

The branch-resolved approach introduced in Sec. 3.2 (Eq. 38) requires the knowledge of phonon frequencies $w_{j,\vec{k}}$, the OPSFs of every branch $|F_{1j}(\vec{q})|^2$, as well as the OPC differences $\Delta I(\vec{q}, \Delta t)$ (see Sec. 10.4). As can be seen in Eq. 33, calculations of $|F_{1j}(\vec{q})|^2$ at thermal equilibrium require the atomic scattering factors $f_\nu(\vec{q})$, the phonon frequencies $w_{j,\vec{k}}$, phonon polarization vectors $\hat{e}_{j,\nu,\vec{k}}$ and the DWF $M_\nu(\vec{q}, t)$. For calculating the DWF at thermal equilibrium, phonon modes were populated according to Bose-Einstein statistics at a given temperature. Phonon frequencies and polarization vectors were provided by the DFPT calculations, whereas atomic scattering factors were used from the *NIST* database for atomic form factors. A dense \vec{k} -grid for the DFPT calculations, which is additionally extrapolated, is required due to the following reasons. Merging DFPT and experimental data requires a similar resolution of both data sets. A typical resolution of our experiment is in the range of 0.01\AA (see Sec. 7.4.1). Additionally, the DWF depends on a sum over all phonon frequencies and polarization vectors. Due to the high computational effort to carry out such calculations, they had to be performed on a HCP cluster.

With the phonon frequencies and the branch-resolved OPSFs we are able to calculate the OPC maps $I_{1,j}(\vec{q})$ (Eq. 32) in thermal equilibrium, as shown in Fig. 8. To account for the finite coherence of the electron beam we apply an additional smearing of the OPSF and OPC by convolving them with a 2D-Gaussian kernel. The width of the kernel is adapted to the width of the Bragg peaks accessible by the experiment. Each map in Fig. 8 represents the OPC of the one of the 18 branches of MoS_2 to the diffuse scattering signal. OPC maps are strongly dominated by the shape of the OPSFs, that reflect the n-fold symmetry of the crystal across the entire diffraction pattern, whereas phonon frequencies are redundant in every BZ. Branches 7,8,9 and 10 are completely inactive and do not contribute to the inelastic scattering signal. The $1/\omega$ -dependence of the OPCs is strongly reflected in the intensity, showing that low-energy branches have higher intensities than high-energy branches.

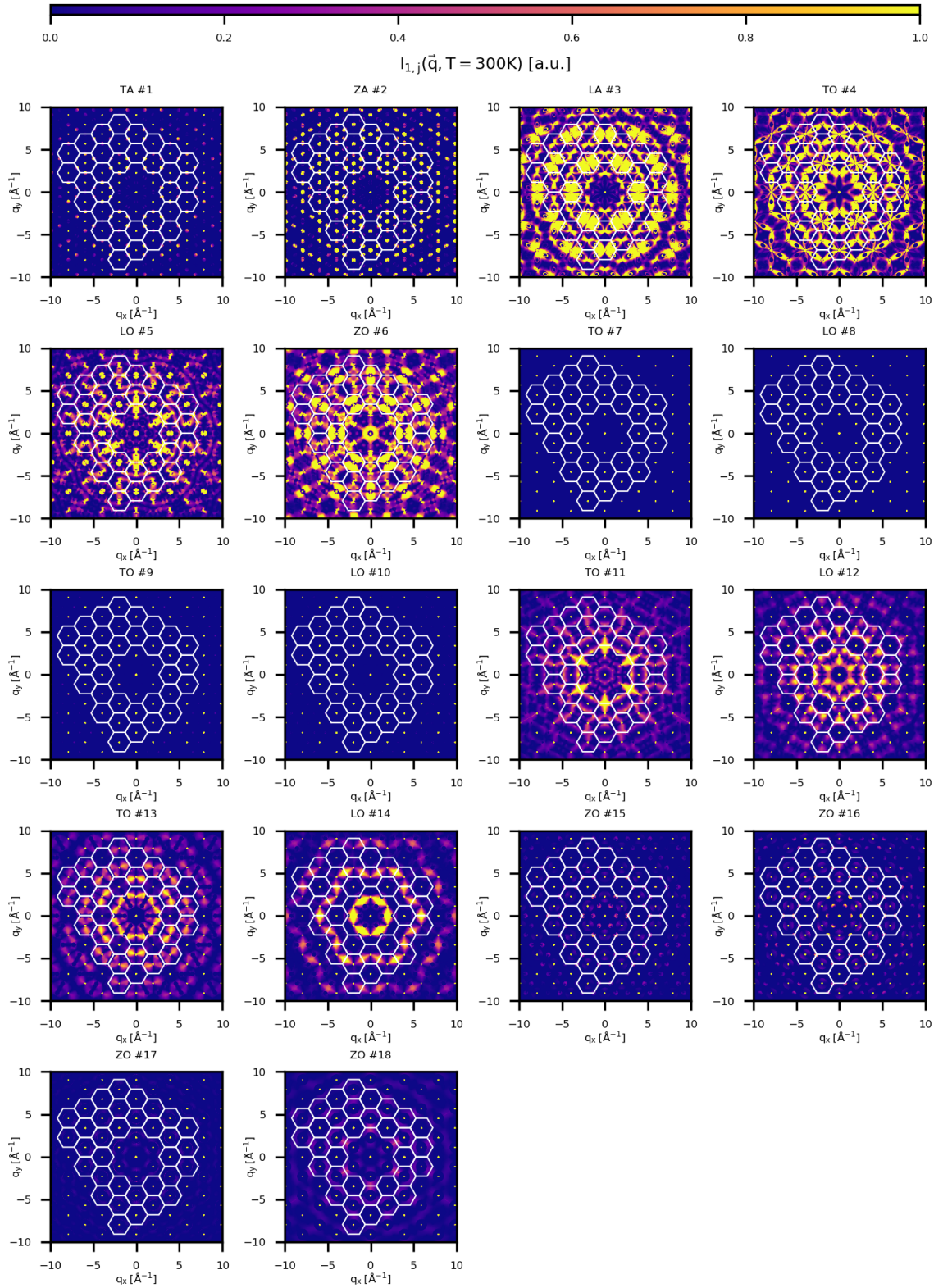


Figure 8: Branch-resolved one-phonon contribution maps of MoS₂ at $T = 300$ K, $I_{1,j}(\vec{q}, t)$, in the diffraction plane probed by the experiment. White hexagons mark the Brillouin zones available in the experiment. Bragg peaks are intense spots in the middle of every BZ. All maps are normalized to the same factor.

6 Self-consistency and the role of multicollinearity

Before applying the optimization approach introduced in Chapter 3.2 to the experimental data, this Chapter describes how multicollinearity can be detected in our specific application. In particular, we describe a self-consistency scheme that we have developed to test the stability of the optimization procedure. For this test, the inelastic intensity difference $\Delta I_{\text{exp}}(\vec{q}, \Delta t)$ on the left side of the equation system (Eq. 38) is replaced by the calculated OPC difference, $\Delta I_{1,\text{model}}(\vec{q}, T_1, T_2)$. This gives the following equation:

$$\Delta I_{1,\text{model}}(\vec{q}, T_1, T_2) = \lambda \cdot \sum_j \frac{\Delta n_{j,\vec{k}}}{w_{j,\vec{k}}} |F_{1,j}(\vec{q}, T)|^2, \quad (62)$$

where $\Delta I_{1,\text{model}}(\vec{q}, T_1, T_2) = I_1(\vec{q}, T_2) - I_1(\vec{q}, T_1)$ is the difference of the one-phonon contributions in thermal equilibrium with temperatures T_1 and T_2 . As a constant OPSF is only an approximation and would depend on temperature changes as well, we have to choose an OPSF temperature T which gives the best approximation. In Chapter 3.2.1 it is shown that setting the OPSF temperature to $T = T_2$ is the best choice.

Now both sides of the equation system depend only on the DFT calculations. Since $\Delta I_{1,\text{model}}(\vec{q}, T_1, T_2)$ is calculated in thermal equilibrium, the resulting phonon population changes are expected to be $\Delta n_{j,\vec{k}} \leq \Delta n_{j,\vec{k}}^{\text{BE}}(T_1, T_2)$, where $\Delta n_{j,\vec{k}}^{\text{BE}}(T_1, T_2)$ is the difference of the BE-statistics at T_1 and T_2 . Indeed, as shown in Chapter 3.2.1, the results should underestimate the true population changes. Hence, we expect the retrieved elevated temperatures from $\Delta n_{j,\vec{k}}, \tilde{T}_2$, to be lower than T_2 . Thanks to this procedure, the areas of the BZ where the least squares solver is not working properly can be identified. They correspond to areas with strong deviations from the expected temperature. These areas should be equivalent to those with high multicollinearity received by the VIF test (see Chapter 4.3). Additionally, the self-consistency test provides a measure of how much the constant-OPSF-approximation for a given ΔT underestimates the true phonon population changes and the resulting elevated temperature.

6.1 Determination of phonon temperatures

From phonon population changes we can invert the Bose-Einstein statistics to calculate the elevated temperature T_2 . With the initial temperature T_1 we get the following equation for the phonon population change $\Delta n_{j,\vec{k}}(\Delta t)$ at wave vector \vec{k} , pump probe delay Δt and branch index j :

$$\begin{aligned} \Delta n_{j,\vec{k}}(\Delta t) &= n_{j,\vec{k}}(T_2) - n_{j,\vec{k}}(T_1) \\ &= \frac{1}{\exp\left[\frac{\hbar\omega_{j,\vec{k}}}{k_B T_2}\right] - 1} - n_{j,\vec{k}}(T_1). \end{aligned} \quad (63)$$

In this case the initial temperature $T_1 = 300$ K is known and we can rewrite Eq. 63 to get T_2 as a function of $\Delta n_{j,\vec{k}}(\Delta t)$:

$$T_2 = \frac{\hbar\omega_{j,\vec{k}}}{k_B} \left[\frac{1}{\log\left(\frac{1}{\Delta n_{j,\vec{k}} + n_{j,\vec{k}}(T_1)} + 1\right)} \right]. \quad (64)$$

6.2 Self-consistency test on graphene

Before testing the implementation of the least squares solver on MoS₂, we do a first test on graphene. Graphene, with its 6 phonon branches, is a much simpler system than MoS₂ and we expect it to be less susceptible to multicollinearity. It is also very close to graphite, the only material which has been examined by this approach at the current stage [20]. *Ab initio* calculations on graphene (space group P6/mmm) were performed⁵ using the PBE generalized gradient approximation [56] to density functional theory, as implemented in the *Quantum Espresso* software package [54]. For the self-consistent field calculations we used a plane-wave basis set on a 10x10x1- \vec{K} -grid with a cutoff energy of $E_{cut} = 80$ Ry and projector-augmented wave (PAW) pseudopotentials. Interatomic force constants are determined by applying DFPT [57] using a 8x8x1- \vec{q} -grid in the BZ. Eigenfrequencies and eigenvectors, necessary for the calculation of the one-phonon contribution $I_1(\vec{q}, T)$, were obtained by using standard Fourier-interpolation on a 50x50x1- \vec{q} -grid.

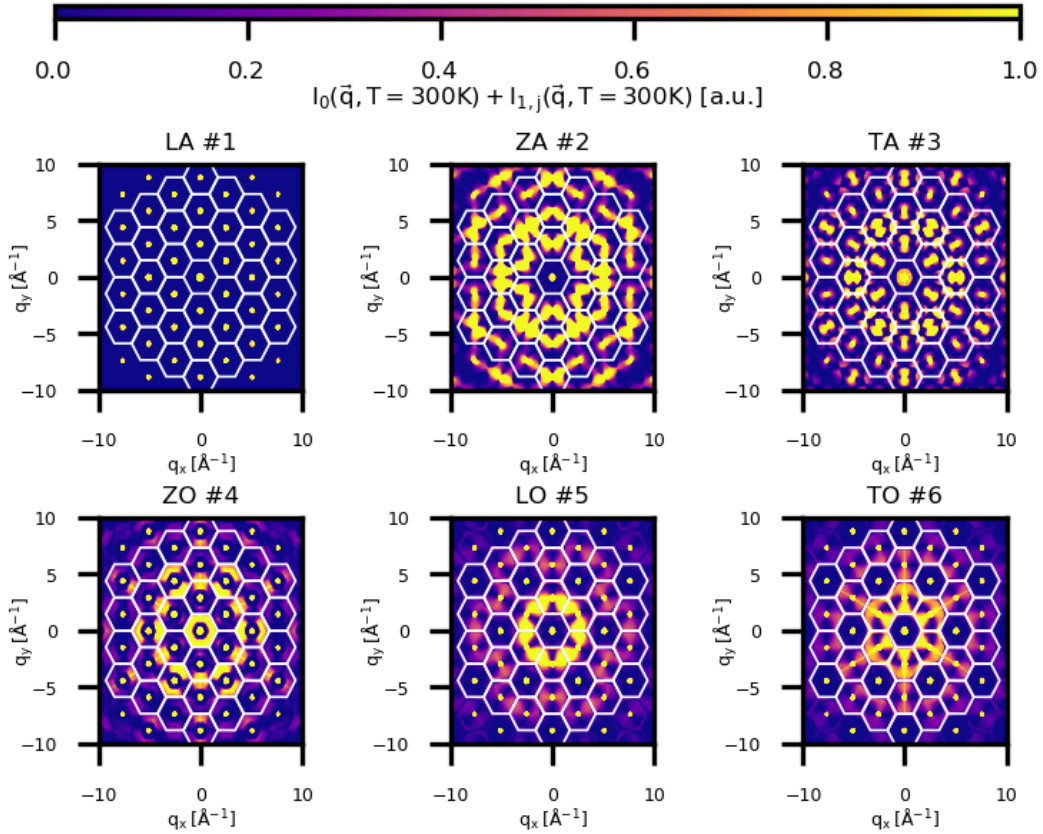


Figure 9: Branch-resolved one-phonon contribution maps with Bragg peaks, $I_0(\vec{q}, T) + I_{1,j}(\vec{q}, T)$, at a temperature of $T = 300$ K. The BZs are indicated by white hexagons. Branches are sorted according to their energy at Γ , starting with the lowest energy.

Figure 9 shows the calculated branch-resolved OPC-maps $I_{1,j}(\vec{q}, T)$ with Bragg peak

⁵Calculations were performed by Dr. Marios Zacharias, currently affiliated at the Cyprus University of Technology

intensities $I_0(\vec{q}, T)$. Bragg peak intensities are limited to Γ with their width determined by a smearing parameter. The first LA-branch is completely inactive and does not contribute to inelastic one-phonon scattering. Hence the system can be reduced to five in-plane active branches. Before carrying out the self-consistency test, we probed the multicollinearity of the resulting OPSF-matrix $\bar{\bar{F}}_{\vec{k}}$ (Eq. 41), to see how regions with high multicollinearity affect the least-square solver. The columns of $\bar{\bar{F}}_{\vec{k}}$ are probed for multicollinearity by calculating the variance inflation factor (VIF), as described in Chapter 4.3.

The resulting VIF maps $VIF_j(\vec{k})$ for all branches of graphene are shown in figure 10. Every map represents the VIF of one column of the OPSF-matrix for all available reduced scattering vectors \vec{k} (Sec. 4.3). One column of the OPSF-matrix is given by the OPSF contribution of one branch. The column length is determined by the number of BZs analyzed. This means, that every column is only related to a single OPSF branch contribution. In fact, the most direct form of multicollinearity, multiple collinearity, occurs if different branch contributions have the same features in the OPC maps at a reduced scattering vector \vec{k} . Such similarities emerge when phonon branches have similar energies and polarization vectors.

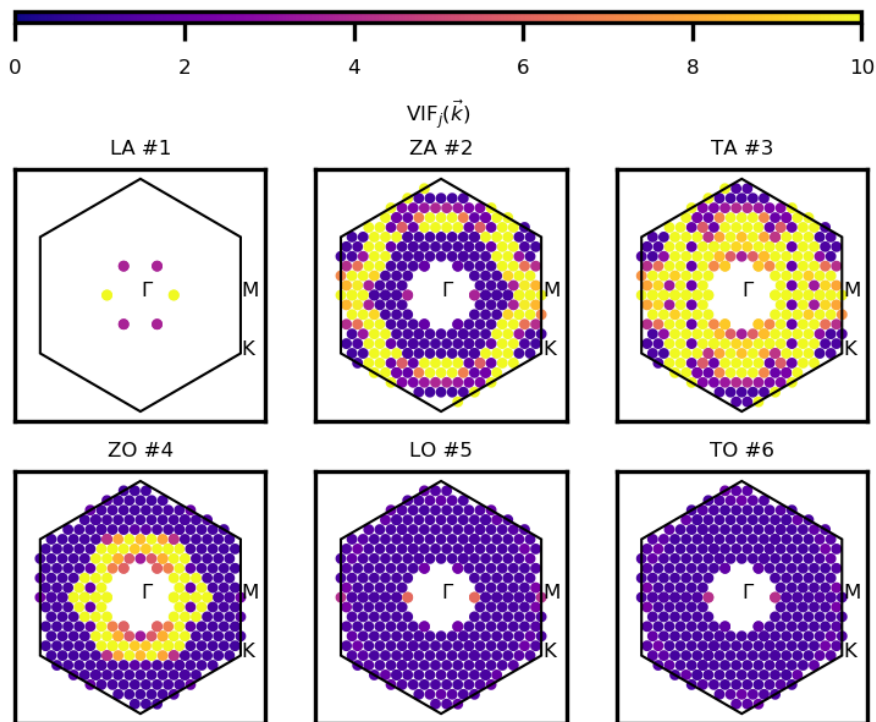


Figure 10: Variance inflation factor $VIF_j(\vec{k})$ of the OPSF-matrix $\bar{\bar{F}}_{\vec{k}}$ for all branches of graphene. Brillouin zones are indicated by black hexagons. Collinear Bragg peak contributions ($\vec{k} < 0.45 \text{ \AA}^{-1}$) are cut out, such that the VIF shown is only affected by the OPC. $VIF(\vec{k}) > 5$ values are treated as highly multicollinear. Empty fields indicate areas where the VIF is not defined. [58]

In the context of our experiment, effects of multicollinearity can be explained in a

non-mathematical way. The branch-resolved approach separates the branch contributions in diffuse intensity by their $|F_{1,j}(\vec{q}, T)|^2/w_{j,\vec{k}}$ -patterns. A separation of contributions is only possible when the different branch contributions are sufficient different in all considered BZs. Similarities in the OPSF contributions or, in other words, indistinguishable diffuse signals, generate multicollinearity in $\vec{F}_{\vec{k}}$.

Figure 10 shows that three out of the six phonon branches of graphene exhibit high multicollinearity. We cannot define a VIF in most parts of branch 1 since it has no OPC in most areas. Furthermore, the shape of high-VIF points (VIF > 5) in branch 3 is equal to the sum of high-VIF points of branches 2 and 4. Since these branches are the only branches with high multicollinearity, it follows that branches 2 and 3 are mostly collinear in the outer regions of the BZ and branches 3 and 4 are mostly collinear in the regions close to Γ . The effect of multicollinearity on the solution of Eq. 62 gets visible by applying the self-consistency test on the non-binned system solved with the NNLS algorithm. The mode-resolved elevated temperatures $T_{2,j}(\vec{k})$ retrieved from the phonon population changes are shown in Fig. 11.

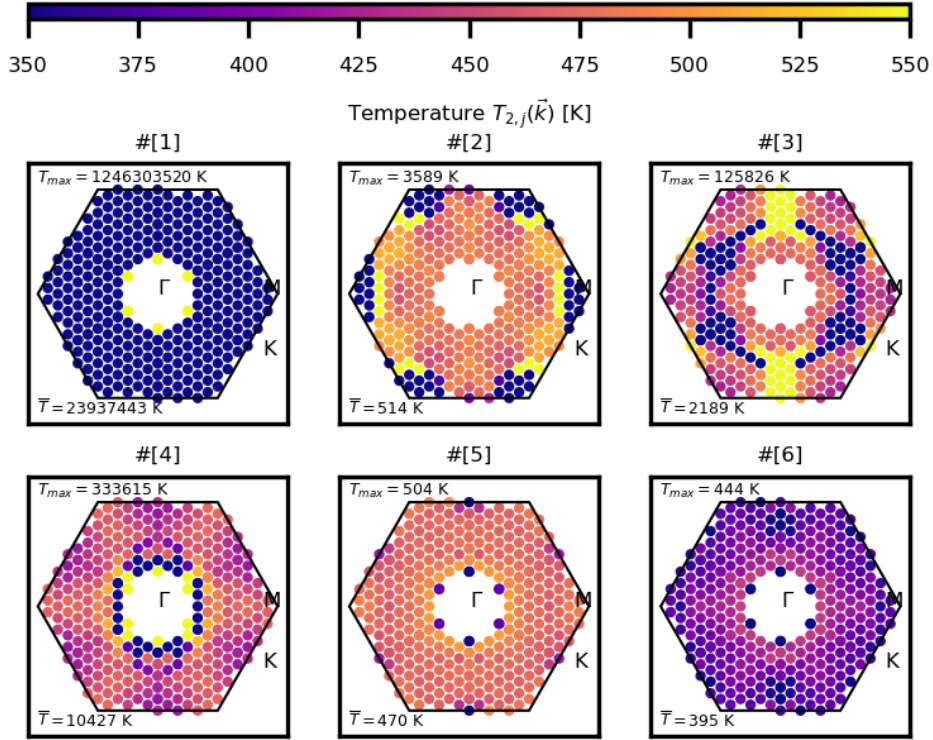


Figure 11: Mode-resolved phonon temperatures $T_{2,j}(\vec{k})$, calculated from the phonon population changes obtained by the self-consistency test on graphene with an initial temperature $T_1 = 300$ K and an elevated temperature $T_2 = 500$ K. The equation system was solved with a standard NNLS algorithm as implemented in the *SciPy*-package [37]. The first BZ is indicated by black hexagons. Maximum temperature and average branch temperature are shown in the insets.

If there was no multicollinearity, all active phonon branch areas should have an elevated temperature a few Kelvin lower than $T_2 = 500$ K. The temperature should be

constant over the entire first BZ and all branches, as shown in the previous section. In practice, we observe deviations from a constant temperature, which we attribute to multicollinearity and additional unknown instabilities from the least squares solver. The hotspots in the first branch, which are found close to Γ , are attributed to multicollinearity induced by the Bragg peaks, which haven't been cut out perfectly. Branches 2,3 and 4 show extreme temperature fluctuations in the areas of the first BZ that are most affected by multicollinearity, underpinning its devastating effect on the solution. Areas with mostly no multicollinearity show roughly constant temperatures in a range between 420 K and 520 K. The best solutions are retrieved for branches 5 and 6, which have the lowest VIF values. The elevated temperatures at the edges of the BZ of branch 6 are attributed to the fluctuations of branches 2 and 3, since instabilities in some branches can be transferred in the same areas of different branches, due to the equation system itself. In conclusion, the self-consistency test shows that even for a very simple system like graphene, multicollinearity has an tremendous effect on the solutions of Eq. 62 and makes a physical interpretation impossible. Testing the equation system for multicollinearity should always be one of the first steps in applying this approach to different materials.

A consequence of these findings is that the more branches contribute to the inelastic scattering signal, the more multicollinearity is imported to the equation system. Given that most materials are more complex than graphene, these findings can be expected to hold for a wide range of materials. In general, the method is most suitable for materials which have a clear separation in branch properties. But how can it be applied to materials with many atoms in the unit cell and thus many phonon branches? A standard approach in case of strong multicollinearity is to redefine the model. As multicollinearity indicates a redundant model, it can be reduced by reducing the amount of columns in the model (in our case $\bar{\bar{F}}_{\vec{k}}$). In the next sub-section, we describe how equations 62 are simplified, by binning branches together.

6.3 Branch binning

The only possibility to reduce multicollinearity in the equation system is to reduce the number of columns in the matrix $\bar{F}_{\vec{k}}$. For the physical system, this is equivalent to reducing the number of branches. In this work, the number of branches is reduced by binning highly collinear and multicollinear branches into what we refer to as *effective branches*. If $[j, \dots, k]$ is a set of highly multicollinear branch indices, we can write their OPC changes as:

$$\Delta I_{1,m}(\vec{q}, T) = \sum_{l \in [j, \dots, k]} \Delta I_{1,l}(\vec{q}, T) = \sum_{l \in [j, \dots, k]} \frac{\Delta n_{l,\vec{k}}(T)}{\omega_{l,\vec{k}}} |F_{1,l}(T, \vec{q})|^2. \quad (65)$$

Replacing $\Delta n_{l,\vec{k}}(T)$ with an effective phonon population change $\Delta n_{m,\vec{k}}^{\text{eff}}(T)$ and $\omega_{l,\vec{k}}$ by an effective frequency $\omega_{m,\vec{k}}^{\text{eff}}$, we can rewrite equation 65 as:

$$\Delta I_{1,m}^{\text{eff}}(\vec{q}, T) = \frac{\Delta n_{m,\vec{k}}^{\text{eff}}(T)}{\omega_{m,\vec{k}}^{\text{eff}}} \sum_{l \in [j, \dots, k]} |F_{1,l}(T, \vec{q})|^2. \quad (66)$$

This reduces the phonon population changes of the individual branches to a single effective branch population, which is modulated by the sum of their OPSFs. To derive a temperature change from $\Delta n_{m,\vec{k}}^{\text{eff}}(T)$, we use the effective frequency $\omega_{m,\vec{k}}^{\text{eff}}$. In this work, $\omega_{m,\vec{k}}^{\text{eff}}$ is defined as the arithmetic mean of branch frequencies:

$$\omega_{m,\vec{k}}^{\text{eff}} = \frac{1}{n} \sum_{l \in [j, \dots, k]} \omega_{l,\vec{k}}, \quad (67)$$

where n is the number of binned branches. Since equation 65 is not equivalent to equation 66, it creates a deviation from the original problem and has to be used with caution. Replacing branch frequencies with their mean value increases the influence of branches with frequencies higher than the mean value, and decreases it for branches with lower frequencies, due to the $1/\omega$ -dependence in equation 65. In the ideal case, the frequencies of the binned branches should be almost identical to each other in order to minimize the deviations as described. Indeed in the case of almost identical frequencies, Equation 66 converges towards equation 65. Such considerations are also important for the physical interpretation of the resulting phonon dynamics, since phonon frequencies are the driving terms in electron-phonon coupling models [12, 52, 59].

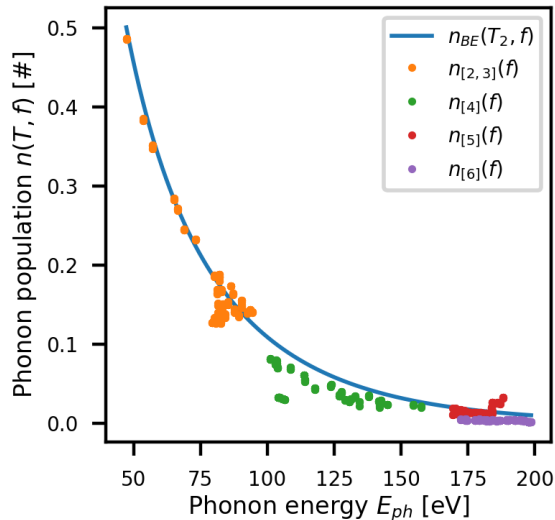
6.4 Self-consistency test with binned phonon system

In this section, branch binning was applied as described in section 6.3 to graphene. We tested different variations of binning the highly multicollinear branches 2 (ZA), 3 (TA) and 4 (ZO), shown in figure 10. The \vec{k} -grid, Γ -cutoff and integration window size used were identical with those in the previous sections.

It turned out that a binning of branches 2 (ZA) and 3 (TA) gave the best result, in terms of the deviation from phonon population changes calculated with Bose-Einstein statistics. The comparison of the Bose-Einstein statistics and the calculated phonon

populations is shown in Fig. 12. Binning all three branches to one branch resulted in a very uneven distribution of phonon populations and temperature changes, which is attributed to the different frequencies of these three branches.

Figure 12: Comparison between Bose-Einstein statistics at $T_2 = 500$ K (blue line) and phonon populations retrieved from the self-consistency test for every effective branch (dots). The phonon frequency range is reduced due to the cut Γ -area.

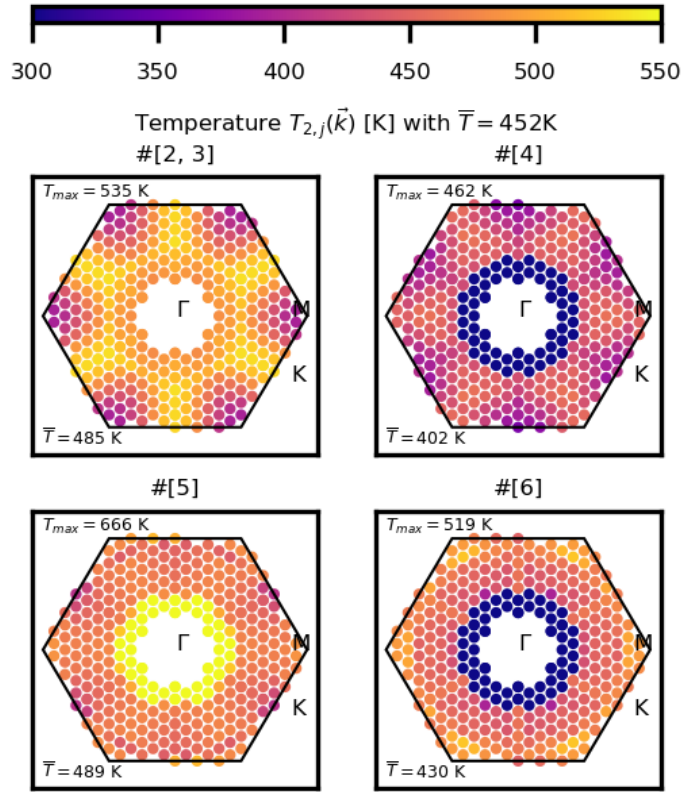


The phonon populations retrieved by the self-consistency test show a good agreement with the Bose-Einstein-statistics. From this plot, we can also conclude that the systematic underestimation of phonon populations, discussed in Chapter 3.2.1, does not lead to drastic departure from the exact populations. A complete interpretation of the results is only possible if also the resulting temperatures are considered. The temperatures of the binned phonon system obtained by the self-consistency test are shown in figure 13. The overall branch-averaged temperature is $\bar{T} = 452$ K, which is 25 % lower than the elevated temperature T_2 , which is consistent with the phonon populations. In addition to the effect of the constant-OPSF-approximation, discussed in Chapter 3.2.1, an underestimated temperature might also be a result of the branch binning. The effective branches could also lead to a shift of optical phonon populations to acoustic populations, which would result in a smaller temperature change.

A comparison with the VIF shows that the remaining highly collinear regions of branches 3 (TA) and 4 (ZO) close to Γ still induce temperature fluctuations in that area. In general, we observe that the collinearity between two branches in a given region of the BZ also affects the same area in other branches. Aside from the region close to Γ , most of the other branch areas look well equilibrated in a temperature range between 400 K and 500 K, especially branches 4 (ZO) and 5 (TO). Effective branch [2,3] and 6 still display some small temperature fluctuations around M and K. In addition, a comparison of branch area temperatures with phonon populations shows that the higher the phonon frequencies are, the more unstable the temperatures get. Due to the exponential decaying behaviour of the Bose-Einstein-statistics, small deviations of phonon populations lead to much larger changes in temperature for optical branches than for acoustic branches.

In conclusion, we see that even with a simplification of the phonon system down

Figure 13: Effective-branch resolved temperatures $T_j(\vec{k})$ obtained by the self-consistency test on graphene with an initial temperature $T_1 = 300$ K and $T_2 = 500$ K. The equation system was solved with a standard NNLS algorithm as implemented in the *SciPy*-package [37]. The first BZ is indicated by black hexagons. The maximum temperature and average branch temperature are shown in the insets. The binned branches are indicated by the labels.



to four effective branches, it is not possible to get reliable results over the entire first BZ. As long as multicollinearity exists, it will always create regions in the first BZ that cannot be trusted. In Ref. [20], which initially presented this approach, it is not clear whether the authors were aware of the effects of multicollinearity. The authors present the phonon population changes retrieved by the NNLS for non-equilibrium as well as equilibrium timescales and only for 3 out of 5 active branches. A temperature is only calculated for the A'_1 mode of the TO2 branch. Hence it is not possible to see if all branches are fully equilibrated at 100 ps pump-probe delay. Moreover, as seen in this section, strong deviations in one branch could significantly affect population changes in the same k -area in a different branch. Due to the limited amount of branches shown in the paper, that aspect remains also unclear. Regarding the equilibrium temperature reached by the A'_1 mode, which decays to the effective lattice temperature, it is not mentioned whether the effective temperature is consistent with the temperature obtained by analyzing the Bragg peaks.

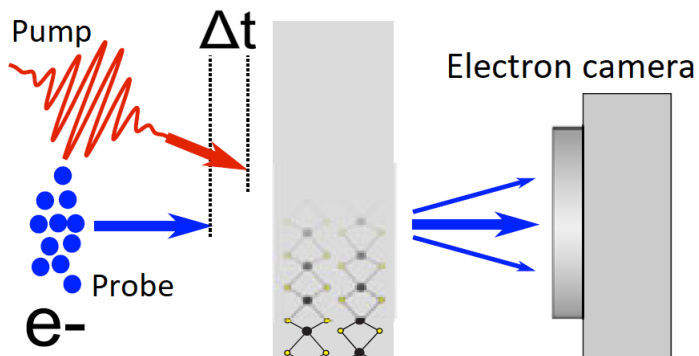
7 Experimental methods

7.1 Experimental setup

To investigate the lattice dynamics of MoS₂, we use an electron diffractometer based on the pump-probe technique. This technique is known as femtosecond electron diffraction (FED) [7, 11, 60]. A schematic illustration of a FED experiment is shown in Fig. 14. The optical pump pulse photoexcites electrons in the crystal, before an electron pulse probes the crystal structure. The temporal distance between the two pulses is given by the pump-probe delay Δt , that can be set by tuning the optical path length of the pump or probe pulse. By recording a set of diffraction patterns for different pump-probe delays, we are able to investigate the lattice dynamics of non-equilibrium states after photoexcitation.

A detailed schematic of the experimental setup at FHI is shown in Fig. 15. The

Figure 14: Schematic illustration of a FED experiment. Optical pump pulse and electron probe pulse arrive at the crystal sample with a pump-probe delay Δt . Scattered electrons are recorded with an electron camera. Modified graphics from [21].



Titan:Saphir-Laser generates ultrashort laser pulses with a pulse width of 50 fs and a repetition rate of $f = 4$ kHz, that are split by a beam splitter into pump and probe pulses. The path of the optical pump pulses is indicated by the red and spectrally colored line and is first coupled into a commercial optical parametric amplifier (OPA) that allows a modulation of the pump pulses central wavelength within a range of 250 – 2500 nm. The pump pulses pass through various optical elements to modify the beam size and intensity and are finally fed in the vacuum system. In this experiment, we only used the "pump" path and not the "side pump" path. As shown in Fig. 16, the pump pulses hit the sample from the backside with a slight tilt of the beam relative to the probe axis. This induces a slight broadening of the absorbed beam, as the wave fronts hit the sample at different times. Additionally the spatial beam width is enlarged to ensure a constant illumination.

The probe pulses pass through a home-built nonlinear optical parametric amplifier (NOPA) and are modulated to a central wavelength of 500 – 520 nm. This wavelength is needed to emit photoelectrons in a two-photon absorption process from the gold cathode of the electron gun, shown in Fig. 16. After compression of the pulses with a prism compressor setup, the probe pulses pass a delay stage, that allows an adjustment of the optical path down to to a few micrometers. The resulting smallest possible time delay increment is in the range of a few femtoseconds and thus smaller than the pulse widths.

Finally, the optical probe pulses are fed in the ultra high vacuum (UHV) chamber ($\simeq 10^{-8}$ mbar) and hit the gold cathode. The emitted electrons are accelerated towards the

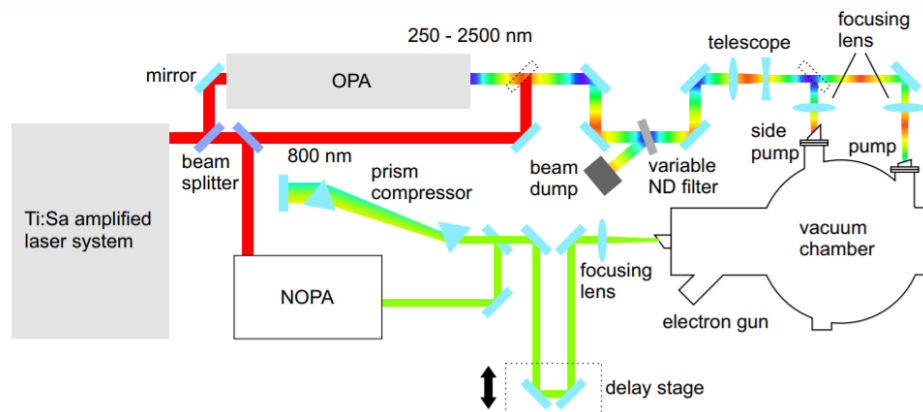
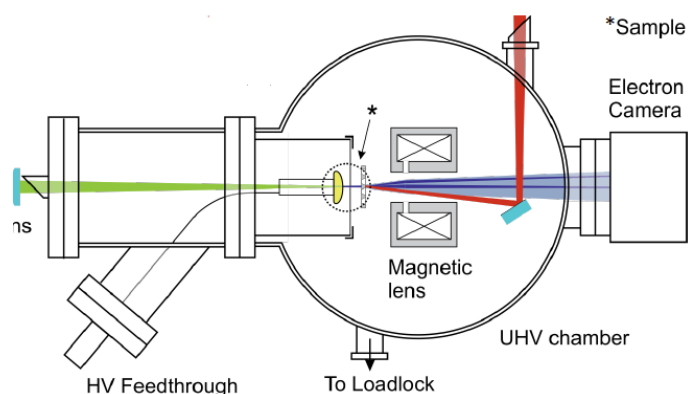


Figure 15: Detailed schematic illustration of the optical setup of the FED instrument at FHI. Used with friendly permission from Daniela Zahn [61].

Figure 16: Schematic illustration of the FED vacuum chamber at FHI with beam paths. The optical pump beam, probe and electron probe beams are indicated by the red, green and blue lines, respectively. The electron probe beam is a modified graphics from [21].



anode by a high voltage electrostatic field, allowing electron energies up to 100 keV. The anode consists of a Si wafer with a small hole in its center to let the electrons go through. The electron probe pulses leave the anode and hit the sample shortly afterwards, to reduce pulse broadening of the electron pulse due to Coulomb interactions [62]. The probe pulses are then focused by a magnetic lens on the electron camera (TVIPS TemCam F416). The width of the electron pulses is estimated to be 150 fs [7] and determines our time resolution.

7.2 Sample preparation

A thin film MoS₂ was produced by mechanical exfoliation from a bulk crystal (*HQ-Graphene* using the viscoelastic stamping [63] and floating techniques [8]. The stamp was built by putting a piece of PDMS (*Sylgard 184 Silicone Elastomer* from *Dow Corning*) on a small glass plate, mounting it with scotch tape. A small crystal piece was then placed on the upwards pointing sticky side of the scotch tape. This gives a stamp in the following material order from bottom to top: glass, PDMS, tape and the crystal flake. The elasticity of the PDMS ensures that the crystal does not break, if light force is applied and should be chosen thick enough.

In the next step a piece of water soluble glue (*Crystalbond 555*) is melted on a second glass plate, building the stamp pad. After the glue has melted, the stamp is placed on top of the stamp pad with the crystal side brought into contact with the glue. The crystal flake should be covered entirely by the glue, without touching the glass bottom. When the glue has cooled and turned solid, stamp and stamp pad are ripped apart. In the ideal case, a part of the crystal flake remains partially in the glue. The remaining crystal is then exfoliated down until the crystal appears transparent under white light conditions.

If the crystal flake has reached its final thickness, it is cut out and transferred into a water bath. In the transfer process, it is very important that the flake floats at the water surface and does not sink, otherwise it is lost. After a few minutes the glue has completely dissolved and the flake is fished out with a standard TEM copper grid. The crystal flake used in the experiment is shown in figure 17 a). The area used for diffraction was chosen due to its homogeneity.

The knowledge of the crystal thickness is important for calculating the absorbed fluence. The fluence is later used in the merging process of model and experimental data. To ensure that the kinematical approximation is still valid, the sample thickness also should be smaller than the mean free path of the electrons, which is usually in the order of a few tens of nanometers.

The thickness was estimated by comparing the white light microscope images with two crystal flakes of the same crystal with a known thickness 17. Based on the crystal area color in a), which is a little lighter than the flake in c), the crystal thickness is expected to be between 40 nm and 50 nm.

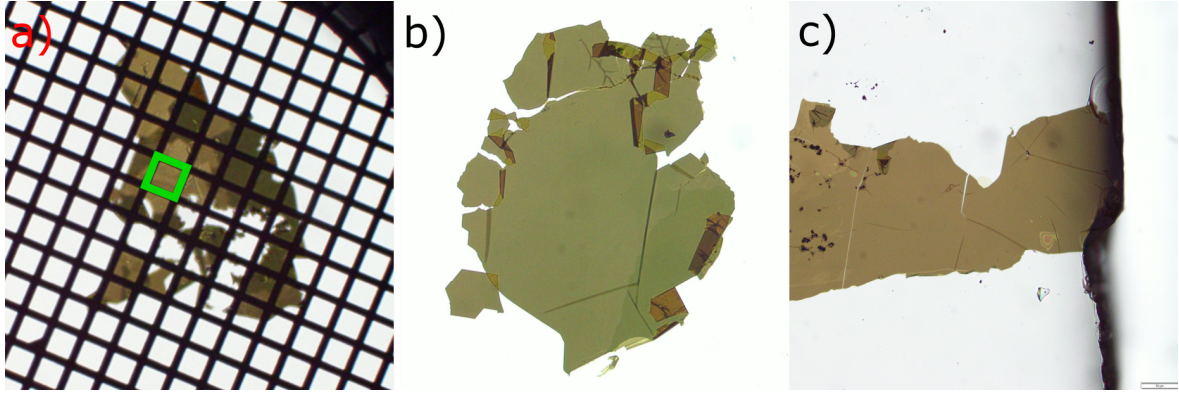


Figure 17: Light microscope images of the MoS₂ crystal flakes under white light conditions. a) Crystal flake used in the experiment. The green square marks the area probed by the electron pulse with a width of 100 μm . b) Another MoS₂ flake with a thickness of (26.5 ± 0.5) nm. The flake shown in c) has a thickness of (49 ± 2) nm.

7.3 Pump parameters

As seen in Chapter 5, bulk MoS₂ is an indirect band gap semiconductor with a gap of 1.29 eV [41, 64] between Γ and the CBM, which is located between Γ and K. Additional valleys are at K with a few meV difference and between Γ and M. The central wavelength of the pump pulse was set to 580 nm, which is equal to a photon energy of ~ 2.14 eV. This photon energy is large enough to excite electrons to all three valleys, but is small enough to suppress electron multiplication [65], which occurs mainly if the energy difference of excited electrons and the CBM is larger than the band gap. The relaxation of excited electrons is then expected to mainly take place via electron phonon scattering.

The pump pulse power was set to $P = (20 \pm 1)$ mW, measured outside the UHV chamber, with a repetition rate of $f_{rep} = 4$ kHz. Inside the UHV chamber the pump pulse is reflected by a prism silver mirror from *Thorlabs Inc*⁶. The resulting loss is estimated from the reflectance to be $L = 1 - R(@580 \text{ nm}) = 2.5\%$. Pump and probe pulse widths are calculated by fitting the averaged intensity profiles with a Gaussian function, resulting in $FWHM_{pump} = 300 \mu\text{m}$ and $FWHM_{probe} = (100 \pm 10) \mu\text{m}$.

A good estimation of the absorbed fluence is necessary due to the following reasons. First if the absorbed fluence and specific heat capacity are known, the temperature change due to the laser excitation can be estimated, which allows additional consistency checks with the elevated phonon branch equilibrium temperatures. Second the absorbed fluence should be small enough to neglect nonlinear effects, to verify that the energy transfer between the lattice and electron system occurs mainly via electron-phonon coupling.

The absorbed fluence $F_{abs} = A \cdot F_{in}$ is calculated by the approach presented in [66], where A is the absorptance and F_{in} the incident fluence at the sample. In this approach the incident fluence is given by the pump-probe overlap profile multiplied with the laser

⁶https://www.thorlabs.de/newgrouppage9.cfm?objectgroup_id=905&pn=MRA10-P01

pulse energy $E_{pulse} = \frac{P}{f_{rep}}$ and the setup loss. The absorbed fluence is then given by:

$$F_{abs} = A \cdot F_{in} = A \cdot (1 - L) \frac{E_{pulse}}{\pi(w_{pump}^2 + w_{probe}^2)}, \quad (68)$$

with $w_i = \text{FWHM}_i / \sqrt{2 \log 2}$. The absorptance A is calculated with the transfer-matrix method and *IMD* software [67], which is based on the Fresnel equations. The refractive index and extinction coefficient for MoS₂ at 580 nm were used from Ref. [68]. Both methods lead to identical results. Fluence calculations were performed assuming the sample thicknesses estimated in the previous section. The results are displayed in table 1.

With the energy density $u = F_{abs}/d$, where d is the sample thickness, and the specific heat capacity $C_{V,p}$ [69–71] under constant volume or pressure, the temperature change of the lattice can be estimated via:

$$\Delta T = \frac{u}{\rho C_{V,p}}. \quad (69)$$

With ρ being the material density. The thickness d , heat capacity $C_{V,p}$ and material density are assumed as perfect without uncertainty. The resulting temperature changes are displayed in table 1.

Thickness d [nm]	25	40	50
Absorbed fluence F_{ab} [mJ/cm ²]	0.96 ± 0.07	1.29 ± 0.09	2.04 ± 0.14
Temperature change ΔT [K]	226 ± 10	190 ± 13	240 ± 17

Table 1: Absorbed fluence F_{ab} and resulting temperature change in thermal equilibrium for fixed thicknesses d for MoS₂.

For the thickness interval $d = [40, 50]$ nm, a temperature change of $\Delta T = [190, 240]$ K is expected and used as a reference for the elevated phonon area temperatures in thermal equilibrium. The temperature change is first decreasing and then increasing, due to the ratio between absorbed fluence and thickness. That is related to the change in the increase of absorptance, due to multilayer effects.

The absorbed fluence is similar or lower compared to other FED experiments measuring monolayer MoS₂ (4.4 mJ/cm² @400 nm [72], 1.46 mJ/cm² @ 515 nm [73]), or few-layer TMDCs TiSe₂ (up to 5.7 mJ/cm²) and is expected to be well in the linear regime.

7.4 Data processing

Diffuse scattering signals are 10^3 to 10^5 orders of magnitude smaller than elastic scattering signals. Due to their higher susceptibility to noise, the successful extraction of such small signals requires a more complex averaging of signals as well as noise and distortion corrections. In this section, we describe the computational aspects related to data processing. As the code is the first implementation of a streamlined inelastic analysis for the work group, this section is also intended to be used as a guide. All scripts for the analysis of elastic and inelastic scattering data were implemented in a streamlined fashion using the *Python* environment *Jupyter*. In our case "streamlined"

means, that every script relies only on the outputs of the previous scripts, except for some calculation parameters loaded from a configuration file. The first script needs the crystallographic information file (CIF-file) [74] of the material to be analysed, as well as the Bragg peak positions on the detector with corresponding Miller indices. These positions are determined manually, thanks to a GUI software also programmed as part of this project. A *Windows* executable of the GUI can be found in the software archive. The benefit of using *Python* is its large library, allowing an easy integration of e.g. Matlab or C++ functionality. The main packages used in the calculations are the *numpy*, *scipy* and *scikit-ued* package [75]. A download link for all software programmed as part of the project can be found here ⁷.

An overview of all applied corrections and averaging steps is shown in Fig. 18. Some of these steps will be discussed in detail in subsections 7.4.1 and 7.4.2. Starting with the electron diffraction data in form of a set of diffraction pattern images, we apply two corrections. First, the background (BG) correction, where a previously recorded image with laser-background is subtracted, accounting for leaking laser light on the detector and thermal noise. The image is taken with switched on pump arm, but switched off probe arm (electrons). Second, every image is weighted with a flat field image accounting for the different sensitivity of the detector areas. After applying both corrections, the Bragg peak positions with corresponding Miller indices are marked on an exemplary diffraction pattern. The peak positions on every image are redefined by applying a center-of-mass method to the areas around the Bragg peak positions. Using the peak positions on the detector and the calculated positions based on the CIF-file, we have developed a distortion correction procedure, which we apply to every pattern in the data set. This procedure is described in detail in Sec. 7.4.1. The resulting fit parameters precisely map the entire diffraction pattern on the detector to reciprocal space, allowing an exact extraction of diffuse scattering intensities. Next, each Brillouin zone is sampled by a grid, as described in Sec. 7.4.2. Scattering intensities are extracted by integrating over circular areas with a defined radius and are later normalized to the estimated total number of electrons in every diffraction pattern. That normalization is necessary, since the total number of emitted electrons at the cathode varies through the measurement and thus affects the scattering intensities. Additionally, intensities of different scans with identical pump-probe delays are averaged. We also use the rotational symmetry of the diffraction pattern relative to the zero order to apply a rotational averaging of scattering intensities. That step enhances the SNR by a factor of \sqrt{n} , where n is the n -fold symmetry of the pattern.

So far all the data processing steps were applied on the entire image. As can be seen in Figure 18, the analysis procedure is then split into the elastic part, which uses the intensities at Γ , and the inelastic part which uses all parts of the BZ except the cut Γ -area.

In the elastic scattering analysis (dark orange in Figure 18), the temporal evolution of relative Bragg peak intensities $I_{0,r}^{hkl}$ are fitted, giving a set of parameters that describes the evolution of the entire phonon system. For more details see Chapter 8. The inelastic analysis is split into a momentum-resolved (green) and a branch- and momentum-resolved analysis (blue). In the momentum-resolved analysis, we import the concept

⁷<https://cloud.fhi-berlin.mpg.de:8443/getlink/fiH6PfwcSVmMM9oQxNgzBpri/>

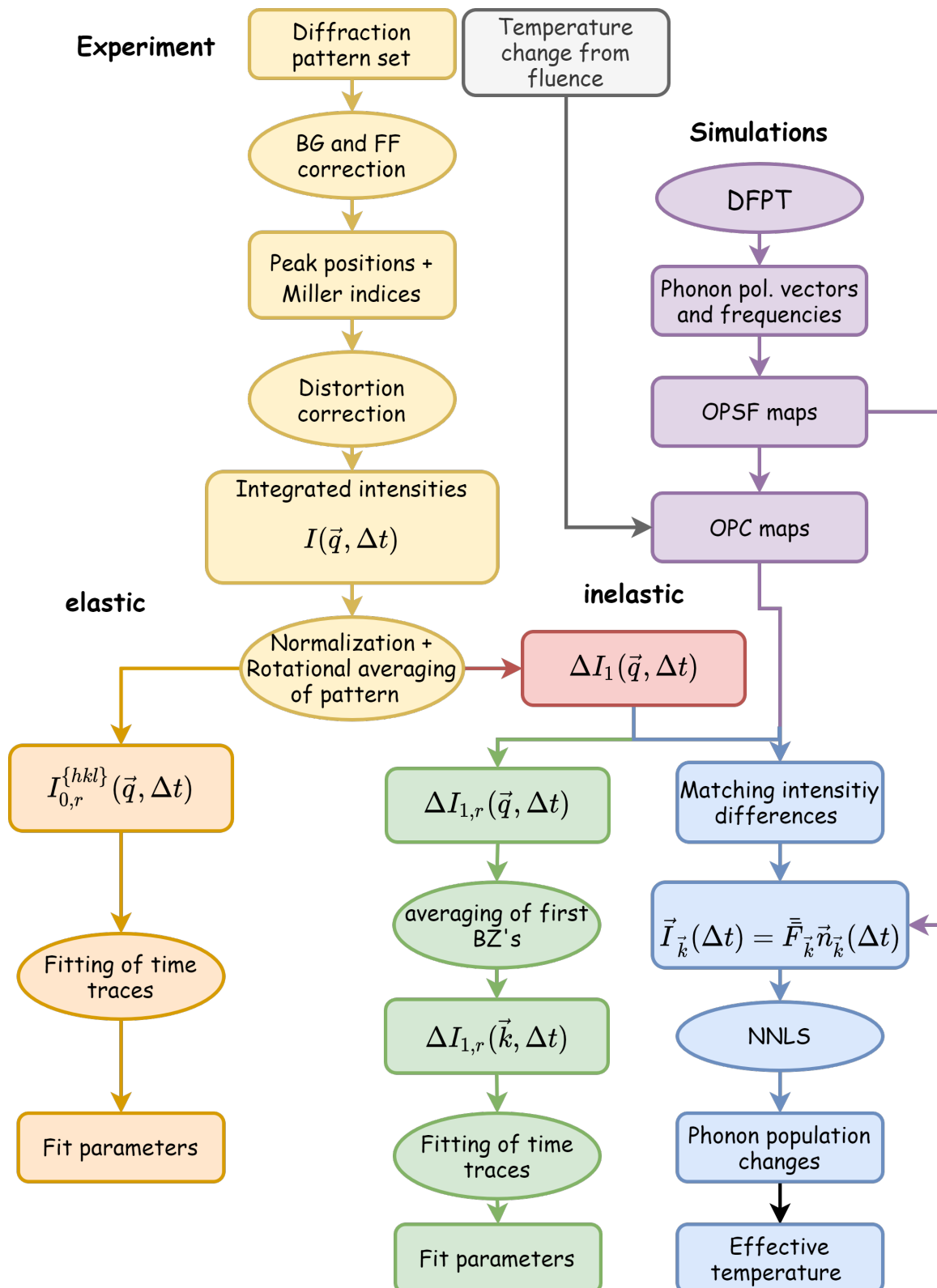


Figure 18: Schematic illustration of the data processing. Squared boxes indicate data and circles indicate methods. Colors mark individual analysis lines.

of the elastic analysis by fitting the temporal evolution of the inelastic intensity differences. Before fitting, the amount of data is reduced by averaging over all BZ's. That step reduces the inelastic signal of many BZ's $\Delta I_{1,r}(\vec{q}, \Delta t)$ to the inelastic signal within a single BZ, $\Delta I_{1,r}(\vec{k}, \Delta t)$. This will be described in detail in Chapter 9.2.

The branch- and momentum- resolved analysis requires the OPSF and OPC difference maps from the DFPT calculations (purple), for details see Chapter 5.3). The OPC difference maps require an initial and a final temperature (see Sec. 10.4), where the initial temperature is given by the experimental conditions and the final temperature has to be estimated from the absorbed fluence (grey), see Chapter 7.3. In the first step of the branch- and momentum- resolved analysis, calculated (OPC difference) and experimental intensity differences are matched by calculating a scaling factor. Afterwards, the equation system of the branch-resolved approach (Eq. 38) is solved handing out the phonon population changes, which can be reformulated as effective phonon mode temperatures. In the next subsections, we provide details about the distortion correction procedure and the sampling of the BZs.

7.4.1 Reciprocal space mapping of diffraction patterns

A key requirement for analyzing time- and momentum-resolved phonon population dynamics is to match the calculated one-phonon structure factors and experimental intensities in reciprocal space. A first step is to map the raw diffraction pattern, in pixels, to reciprocal space units, accounting for experimental distortions. This aim of this section is to describe the procedure for this mapping. From the experiment, we have access to sampling points of the continuous diffraction signal, as recorded by the electron camera. The entire data set consists in a series of diffraction pattern images. Each sampling point is represented by a pixel with a certain intensity value and scattering vector \vec{q} . Due to fluctuations in the electron pulses and magnetic field of the lens, nearly every pixel of every image corresponds to a slightly different scattering vector \vec{q} .

A link between pixels and \vec{q} -space is established by combining pixel positions and reciprocal space positions of Bragg peaks \vec{G}_{hkl} . The reciprocal positions of Bragg peaks with respect to the center of the zero order are nothing less than the scattering vectors:

$$\vec{G}_{hkl} = h \cdot \vec{b}_1 + k \cdot \vec{b}_2 + l \cdot \vec{b}_3, \quad (70)$$

determined by reciprocal lattice vectors \vec{b}_i and Miller indices (hkl).

To map reciprocal space on the diffraction patterns, we first determine the position of the zero order beam, by calculating the mean position of the lowest order Bragg peaks surrounding the zero order, e.g. (100). These pixels are least influenced by the squeezing of the magnetic lens and are most suited for calculating the center position. Using the mean value presumes Bragg peak pairs, hence none of the closest peaks should be covered by the beam block.

Next we find the peak positions of every Bragg peak. Peak positions can be calculated in two different ways. One option is to fit the surrounding areas of every peak with a 2D-Pseudo-Voigt function, which is commonly used to fit X-ray and electron diffraction peaks [32, 75]. This method is expensive in terms of computation time and has the tendency to deform strongly non-symmetric peaks. The second option is to use a center of mass method, which uses intensities as weights. We implemented both options, and deviations between both methods were around 0 px to 2 px.

If only Bragg peaks of the zero-order Laue zone (ZOLZ) are considered, scattering vectors \vec{q} consist of two components, $q_x(x, y)$ and $q_y(x, y)$. These components are functions of the pixel coordinates (x, y) . In the ideal case of no magnetic lens distortions, both functions are tilted planes cutting the origin, with a constant increase. Their tilt is dependent on the orientation of the diffraction pattern with respect to pixel coordinate system of the camera. In practice, however, the presence of the magnetic field results in an unequal squeezing of Bragg peaks to the field center. This effect is referred as a combination of barrel and elliptical distortions[76]. With a centered electron beam, higher order Bragg peaks are squeezed more to the center than lower order Bragg peaks. This results in a tilt of the plane edges.

To perform the reciprocal space mapping, the goal is to find a function for $q_x(x, y)$ and $q_y(x, y)$, that gives the distortion-corrected scattering vector \vec{q} for every pixel position and subsequently allows a partitioning of the diffraction pattern in Brillouin zone areas (e.g. Γ), necessary to carry out our time- and momentum-resolved approach. Peak

position errors are assumed to be insignificantly small.

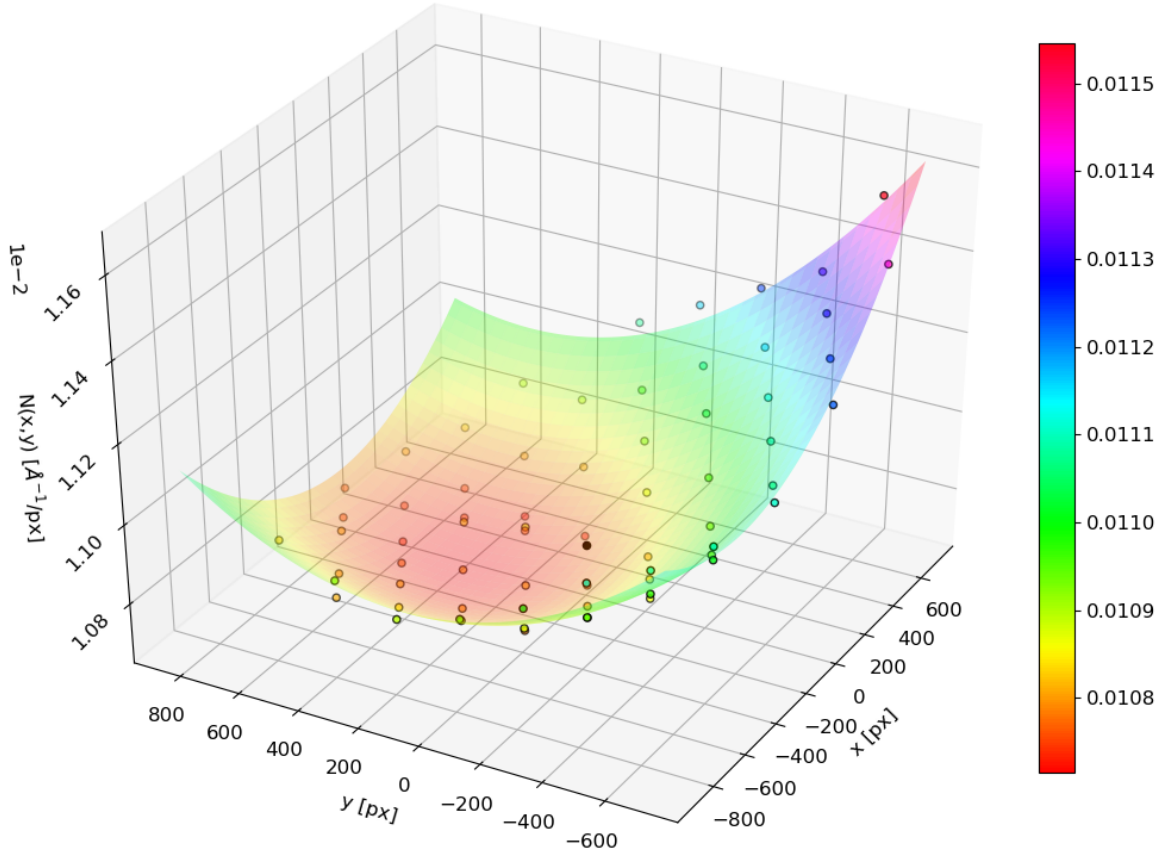


Figure 19: Conversion factor $N(x, y)$ of an exemplary MoS_2 diffraction pattern as a function of pixel coordinates. The colormap gives the $N(x, y)$ values and dots represent the experimental data (Bragg peak positions) with values indicated by the colormap. The black dot indicates the position of the transmitted beam (zero order).

Before determining $q_x(x, y)$ and $q_y(x, y)$ we study the diffraction pattern distortion. For this we define r_{hkl} as the distance between the center of the diffraction pattern and Bragg peak with Miller indices (hkl) in pixels. We can then determine the conversion factor $N(x, y) = |\vec{G}_{hkl}|/r_{hkl}$, which translates between pixel and reciprocal coordinates. This allows us to characterize the image resolution in reciprocal coordinates at every pixel position. We note that $N(x, y) = \text{const.}$ would correspond to the case of an ideal, unsqueezed, diffraction pattern.

Figures 19 and 20 show the resolution $N(x, y)$ as a function of pixel position for an exemplary MoS_2 diffraction pattern. For this data, $N \approx 0.010 \rightarrow 0.015 \text{ \AA}^{-1}/\text{px}$, yielding a momentum resolution of $\approx 0.01 \text{ \AA}^{-1}$ for the area of interest (this does not take into account electron beam coherence effects, which further limit the effective momentum resolution of the experiment). We found the experimental data to be well-fitted with the function $N(x, y) = a(x^2 + y^2) + b + cx + dy + exy$, represented by the surfaces in Figs. 19 and 20.

The first term, $a(x^2 + y^2)$, is rotationally symmetric and depends on r_{hkl}^2 . The param-

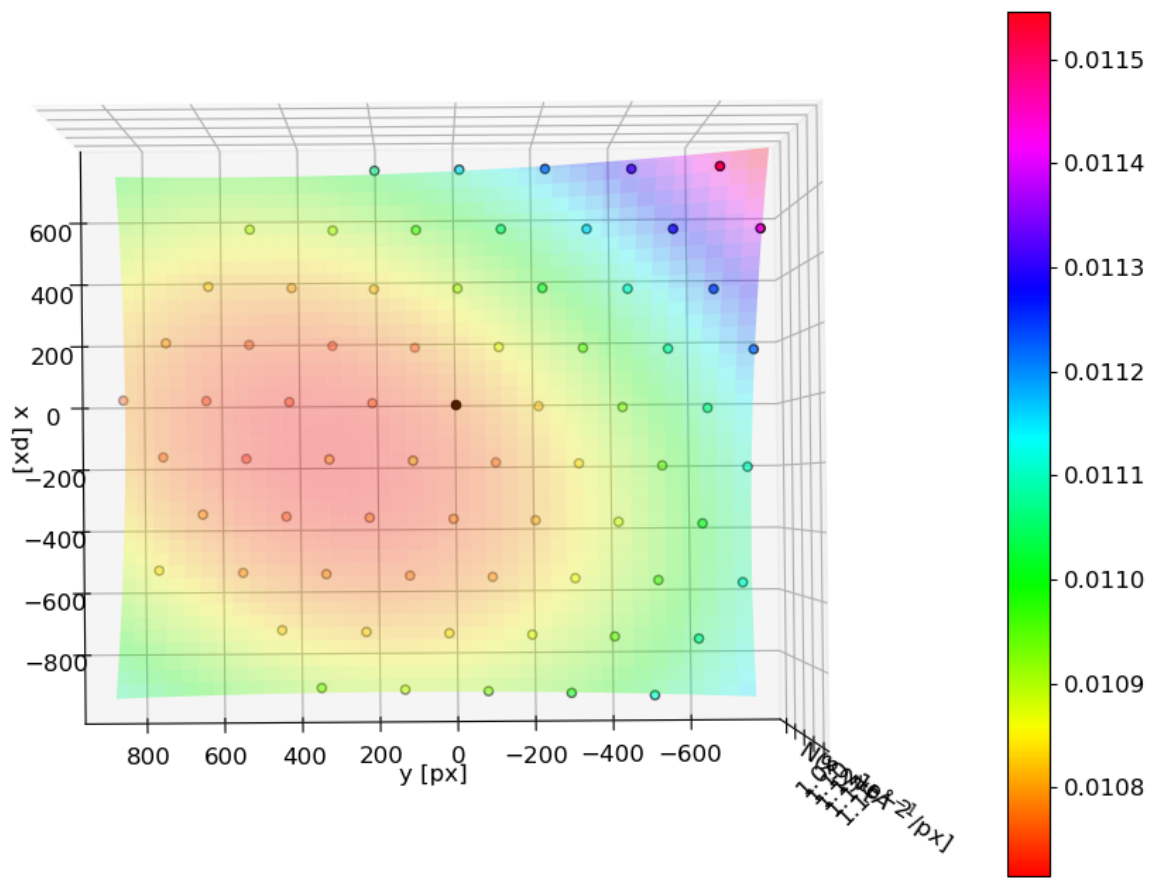


Figure 20: Top view of the conversion factor $N(x, y)$ shown in Fig. 19.

eter b is a constant offset. The terms cx and dy are tilted planes, resulting in a shift of the lens center relative to the zero order. The last term, exy , introduces a 2-fold symmetry to the model to account for elliptical shapes. Figure 20 reveals a clear shift of the center of best resolution from the zero order indicated by the black dot. We account this to a shift of the beam axis relative to the magnetic lens center. Equipotential surfaces have an elliptical shape, which is probably a result of the not perfectly circular pieces of the magnetic lens, resulting in a deviation from the rotational symmetry. In conclusion, elliptical and barrel distortion are governing the diffraction pattern. Both distortions are accounted to effects of spherical aberration [76].

Finally, the scattering vector components $q_x(x, y)$ and $q_y(x, y)$ are determined by fitting them separately to the Bragg peak positions $G_{x,hkl}$ and $G_{y,hkl}$. The following empirical fit function was used:

$$q_i(\acute{x}, \acute{y}) = a_i \cdot \text{sign}(\acute{x})\acute{x}^2 + b_i\acute{x} + c_i(\acute{x}^2 + \acute{y}^2) + d_i\acute{y}\acute{x} \quad (71)$$

where $\acute{x} = x \cos(\theta_i) - y \sin(\theta_i)$ and $\acute{y} = x \sin(\theta_i) + y \cos(\theta_i)$ are the rotated image coordinates and $i \in [x, y]$. The first term $a \cdot \text{sign}(\acute{x})\acute{x}^2$ induces a tilt of the plane edges in respect to their sign. The last terms are similar to those of the conversion factor.

The fitting is performed for every diffraction pattern (≈ 2500 images for MoS_2) for

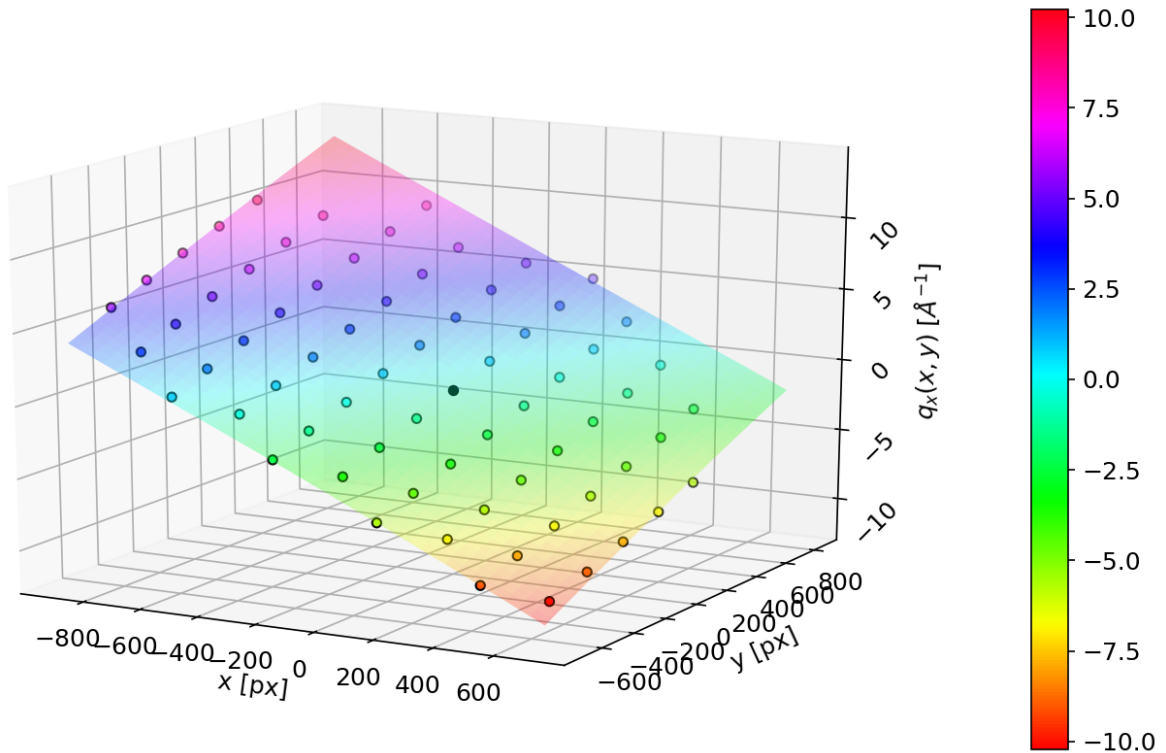


Figure 21: Evolution of $q_x(x, y)$ for an exemplary pattern of MoS_2 , showing a slightly curved plane.

both scattering vector components i , giving two sets of parameters $\{a_i, b_i, c_i, d_i, \theta_i\}$ for every diffraction pattern. An exemplary fit of $\vec{q}_x(x, y)$ with residuals is shown in Fig. 21 and 22 respectively.

A good agreement of the fit model through the data set is indicated by the coefficient

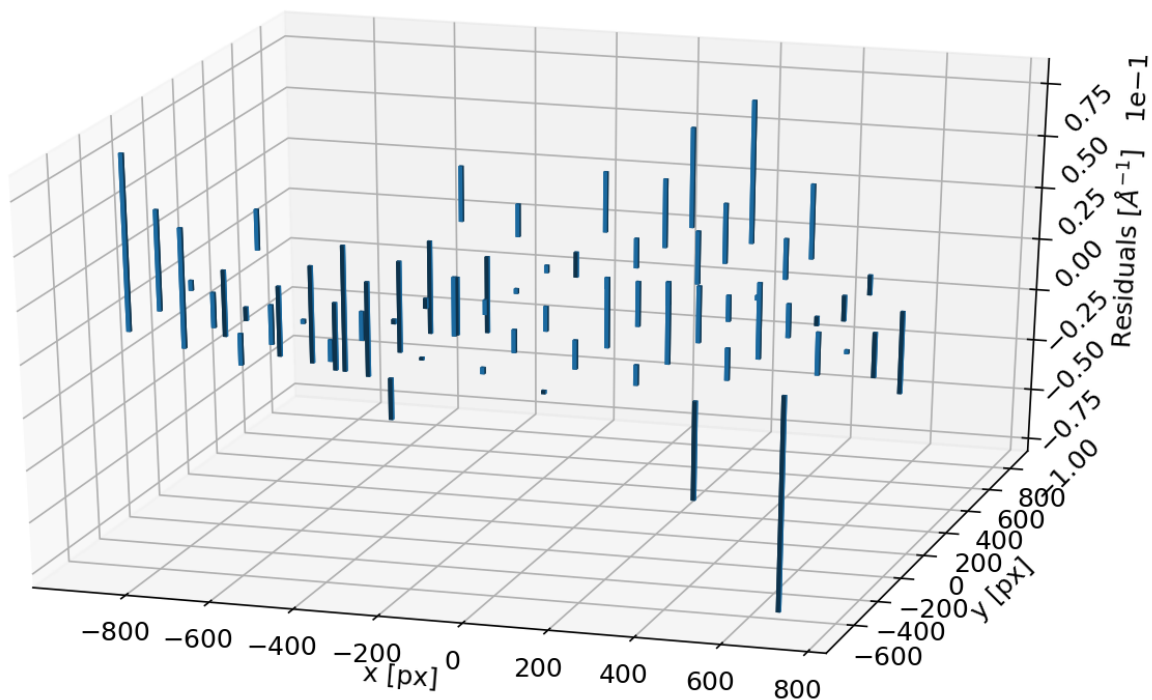


Figure 22: Residuals of the fit indicating stronger deviations for high order Bragg peaks. The mean residual of 0.024 \AA^{-1} corresponds to a mean deviation of ~ 2 px in image coordinates.

of determination of $R^2 > 0.99$ and a total mean residual of 3 px. We now have determined the reciprocal space of all diffraction patterns within the data set, allowing a distortion corrected extraction of scattering intensities over a wide range of scattering vectors as required for the momentum- and branch-resolved approach (Chapter 3.2). Note that the distortion correction does not account for effects introduced by the electron coherence, which result in a smearing of the diffraction pattern and thus in an overlap of electrons with different scattering vectors at \vec{q} .

Instead of compressing and stretching the images to a uniform reciprocal space, intensities are integrated over certain windows. The original information of an image is then conserved. Using the same window size for every peak position introduces an integration error. As the resolution varies over the whole diffraction pattern, every position must be integrated with a different window size to ensure that all windows cover the same reciprocal area. For small window sizes those changes are < 1 px and can be ignored.

7.4.2 Sampling of the first Brillouin zone

After converting the raw diffraction pattern to reciprocal space units, as discussed in the previous section, a crucial step is to merge the calculated OPSF $F_{1,j}(t_0, \vec{q})$ and experimental diffraction patterns, which are defined on different \vec{q} -grids. In this work, calculations of $F_{1,j}(t_0, \vec{q})$ are performed on a linear grid to construct OPSF maps as shown in Chapter 5.4. As a consequence, the sampling of the experimental diffraction pattern must be adapted to the sampling of $F_{1,j}(t_0, \vec{q})$. Ideally, both experimental and theoretical intensities should be calculated on the same grid.

One option is to use the same linear grid for the experiment as used for calculating $F_{1,j}(t_0, \vec{q})$. This gives the best match between both grids, but leads to different sampling point distributions in every BZ. Thus the number of scattering vectors \vec{q} inside the selected BZs with the same reduced scattering vector $\vec{k} = \vec{q} - \vec{G}$ is drastically reduced. A rotational averaging of intensities is then only possible under certain approximations and binning of grid positions.

Instead, in this work, the intensity of the first BZ is sampled based on a Monkhorst-Pack grid [77] as shown in Figure 23. The advantage of a Monkhorst-Pack grid is a uniform sampling of the entire first BZ and supercells, which allows the construction of diffraction maps and additionally conserves rotational symmetry for rotational averaging. The disadvantage of this sampling method is that it creates a mismatch between the linear OPSF grid and intensity grid. As a consequence, the linear grid of the OPSF is chosen with a finer spacing than the intensity grid to minimize the deviation.

Intensities are collected by integrating over windows. The intensity integration window is controlled by the size of Monkhorst-Pack grid and is always chosen small enough to reduce overlap between two windows.

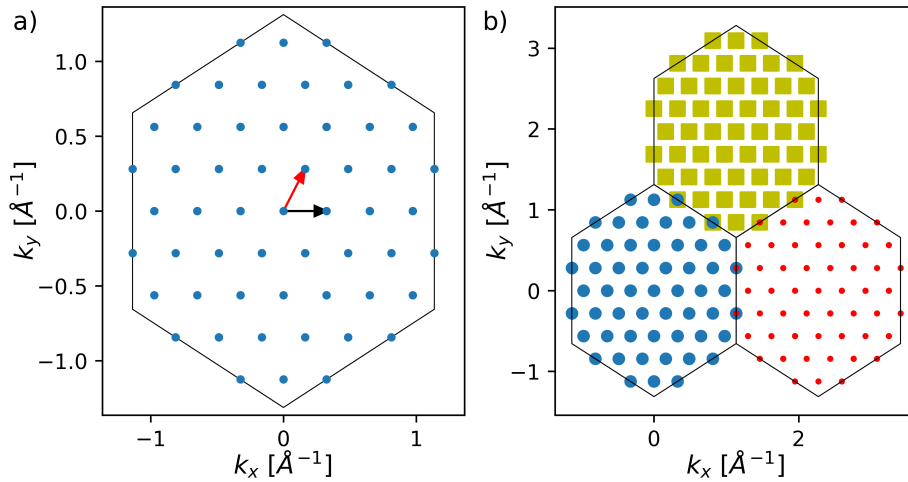


Figure 23: Brillouin zone (black line) sampling of the hexagonal in-plane lattice of MoS₂ based on a 7x7-Monkhorst-Pack grid. Intensities are integrated at positions indicated by markers. a) Single BZ with the corresponding Monkhorst-Pack lattice vectors given by arrows. Monkhorst-Pack vectors are reciprocal lattice vectors divided by $n = k - 1$ with k being the number of sampling points in the corresponding direction. b) Three neighbouring BZs showing the overlap and uniformity of the sampling.

8 Elastic scattering analysis

In this section, the relaxation of the phonon system is studied by analyzing the time dependence of Bragg peak intensities, i.e. the elastic scattering signals. As described in section 3.1.2, Bragg peak intensities depend on the atomic displacement via the Debye-Waller factor, which involves a sum over all phonon modes at reduced scattering vector \vec{k} . Due to the sum, it is not possible to retrieve a momentum- or branch-resolved view from analyzing Bragg peak dynamics, in contrast to inelastic intensity measurements. The benefit of analyzing Bragg peak dynamics clearly lies in the high SNR and the consequent stability of intensities, due to large elastic cross sections. Because of the lower SNR of the inelastic scattering intensities, elastic scattering should be always used as a fundament for interpreting the inelastic scattering results and checking their consistency.

8.1 Results

In total, 48 in-plane Bragg peaks were analyzed and grouped into 8 peak families as shown in figure 24 a). The intensities were extracted by summing counts in circular areas around the Bragg peak centers, which have been determined by a center-of-mass method using the peak intensity distributions. Relative Bragg peak family intensities were calculated by averaging over all individual peak contributions and normalizing them to their negative pump-probe delay intensities.

Figures 24 b) and c) show the relative intensity evolution of the Bragg peak families up to 300 ps. The temporal evolution can be divided in three different phases. In the first phase, all peak intensities at negative pump-probe delays start at a constant level. In the second phase, the peak intensities drop exponentially for a few picoseconds after the pump pulse excited the material. After 15 ps every Bragg peak reached a new constant level at a reduced intensity, that holds up to 300 ps pump-probe delay. In good agreement with the DWF theory (Sec. 3.1.2), the loss of intensity increases with increasing Bragg scattering vector \vec{g}_{hkl} .

In terms of Debye-Waller theory, we interpret the three phases as follows. The first phase represents the phonon system in thermal equilibrium at the initial temperature T_1 . The atomic displacement given by the sum over all phonon modes (Eq. 14) stays constant and thus also the temporal evolution of the Bragg peaks. The exponential decrease of peak intensities of the second phase is explained by the increase of the atomic displacement, due to electron-phonon coupling and the subsequent relaxation of the phonon system.

Within the first few femtoseconds after photo-excitation of the electron system, electron thermalization occurs, creating a hot Fermi-Dirac distribution. The electron thermalization for few-layer MoS₂ occurs within ≈ 20 fs [78] and is treated as instantaneous as our temporal resolution is > 150 fs. The subsequent cooling of the hot Fermi-Dirac distribution occurs via electron-phonon scattering. The energy transfer from photo-excited electrons (holes) with excess energy compared to the conduction (valence) band minimum (maxima) to the phonon system occurs through electron-phonon coupling

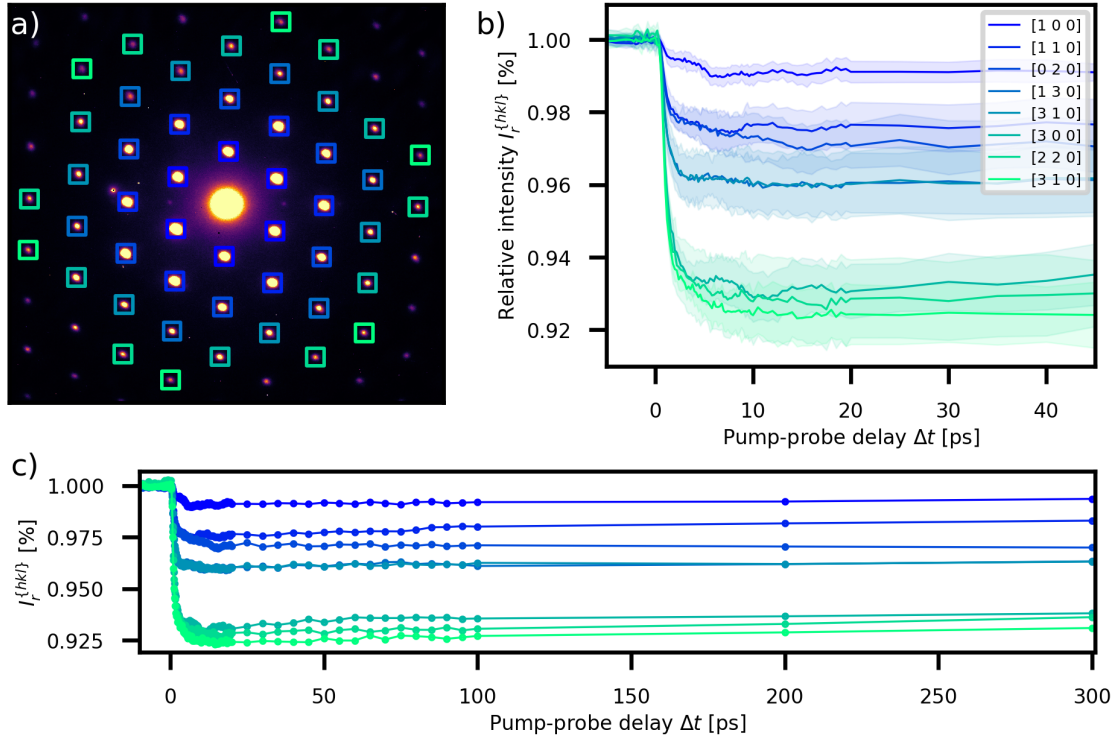


Figure 24: Bragg peak dynamics of MoS₂ at a pump wavelength of $\lambda = 580$ nm and an absorbed fluence of $F_{ab} = (1.29 \pm 0.09)$ mJ/cm². a) An exemplary diffraction pattern with the analyzed Bragg peaks indicated by squares with the electron pulse set along the [001] zone axis. Bragg peaks of the same family $\{hkl\}$ have the same color. b) Average relative intensities $I_r^{\{hkl\}}(\Delta t)$ of the different Bragg peak families as a function of pump-probe delay Δt . Shaded area around the lines indicates the standard deviation over different scans. Bragg peaks are sorted according to their scattering vector length. c) Same Bragg peak intensities but with extended pump-probe delay range.

(EPC). Electronic transitions with phonon emission are determined by the e-ph matrix elements. These elements can be very heterogeneous and certain phonon modes get coupled more strongly to the electrons. In addition to variations in the strength of e-ph matrix elements, there are phase space constraints for e-ph scattering processes, dictated by the excitation conditions and the shape of the electronic band structure. As shown in previous works [12, 52], electrons couple most strongly to optical branches. The generation of hot phonons creates a non-equilibrium phonon distribution, that thermalizes via phonon-phonon (ph-ph) scattering. We refer this process as phonon-phonon coupling (PPC), where the energy transfer from hot to cold phonons is determined by the PPC constants.

Due to the increase of phonon populations by EPC, the atomic displacement is increased (see Eqs. 16 and 19). The $1/\omega_{j,\vec{k}}$ -dependence of phonon amplitudes implies that optical phonons increase the atomic displacement less than acoustic phonons. The subsequent relaxation of non-equilibrium phonon populations into acoustic branches, thus typically leads to stronger changes in atomic displacement than the electron-phonon coupling.

The third phase of the intensity evolution is attributed to the restoration of the Bose-Einstein distribution of the phonon system at an elevated temperature $T_2 > T_1$ due to ph-ph coupling. Based on the DW-theory, the drop of intensity increases with increasing scattering vector. This shows a perfect agreement with intensities shown in 24.

Figure 24 c) verifies that Bragg peak intensities stay constant for large pump-probe delays and no interesting lattice dynamics happen on that timescale. A cooling of the lattice would result in an increase of the Bragg peak intensities, which is not visible on the timescale probed in the experiment.

8.2 Quantification of lattice dynamics

The lattice dynamics are quantified by fitting the relative intensity averaged over all Bragg peak families. Using Eq. 30 gives:

$$\bar{I}_r(\Delta t) = \frac{1}{n} \sum_{\vec{q}=\{\vec{G}_{hkl}\}} e^{-\vec{q}^2[\langle\Delta\bar{\tau}^2(\Delta t)\rangle_t - \langle\Delta\bar{\tau}^2(\Delta t < 0)\rangle_t]} \delta_{\vec{q}, \vec{G}_{hkl}} \quad (72)$$

with \vec{q} running over all reciprocal lattice vectors \vec{G}_{hkl} of the corresponding Bragg peaks, n the number of peaks and $\langle\Delta\bar{\tau}^2(\Delta t)\rangle_t - \langle\Delta\bar{\tau}^2(\Delta t < 0)\rangle_t$ the changes in atomic MSD. For increasing phonon populations the MSD is increasing and thus intensities are decreasing. The average relative intensities are then fitted with a biexponential function convolved with a Gaussian kernel to account for the finite pulse width of the electron pulse. The Gaussian kernel is set to a fixed FWHM of $s = 150$ fs, corresponding to the estimated electron pulse duration. We used the parameterization of the fit function as follows:

$$f(\Delta t) = \Theta(\Delta t - t_0) \left[A_1 \left(1 - \exp \left[-\frac{(\Delta t - t_0)}{\tau_1} \right] \right) + A_2 \left(1 - \exp \left[-\frac{(\Delta t - t_0)}{\tau_2} \right] \right) \right] + c, \quad (73)$$

where $\Theta(\Delta t - t_0)$ is the step function, $A_i, i \in [1, 2]$ the amplitudes and τ_i the time constants. t_0 addresses a slight shift of the excitation and c is an offset.

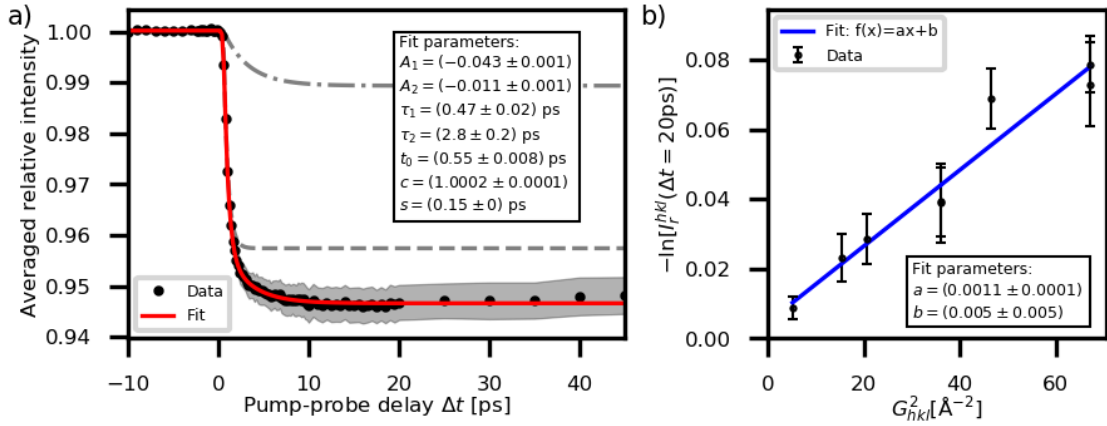


Figure 25: a) Time evolution of the averaged relative intensities $\bar{I}_r(\Delta t)$ as a function of pump-probe delay for multilayer MoS₂. The shaded area shows the error propagated from standard deviations. The red line indicates the biexponential fit with parameters shown in the inset and the dashed lines represent the single exponential terms. Parameter s is fixed. b) Transient decrease of Bragg peak intensities at $\Delta t = 20$ ps as a function of the square of the reciprocal lattice vector \vec{G}_{hkl} . The solid line represents a linear fit with equal weights.

The fit results are shown in Fig. 25 a), revealing one fast decrease of \bar{I}_r with $\tau_1 = (470 \pm 20)$ fs and a larger amplitude $A_1 = -0.043 \pm 0.001$ and slow increase

$\tau_2 = (2.8 \pm 0.2)$ ps with a smaller amplitude $A_2 = -0.011 \pm 0.001$. Later pump-probe delays have not been included in the fit, because of the slight increase of relative intensity, which is accounted to the onset of cooling of the crystal back to the pre-excitation conditions. The coefficient of determination $R^2 = 0.9997$ shows a very good agreement of model and data.

Based on the time constants we assign the first term to EPC and the second term to PPC, as used in previous works [21, 32, 33]. The time constant of EPC shows a good agreement with the time constant of 0.6 ps extracted from ultrafast optical experiments and ab initio molecular dynamics simulations [78] for multilayer MoS₂. At the time of writing, PPC time constants have only been reported for (supported) monolayer MoS₂ and were measured to be in the range of a few picoseconds (~ 3.5 ps [73]). Studies without explicit calculation of time constants report phonon equilibration within ~ 2 ps [72] and ~ 5 ps [52]. These studies are in good agreement with our measurements despite their different excitation conditions.

A very interesting feature of the fit result is the amplitude difference of both processes. The fast process, related to EPC, generates more atomic displacement than the slower process related to PPC. This is in contradiction with the picture of electrons coupling mainly to optical phonons and then decaying into acoustic phonons via PPC. This also differs from recent studies of other materials, where the amplitude of the fast process was found to be smaller than that of the slow process [32, 79]. Due to the $1/\omega_{j,\vec{k}}$ -dependence of phonon amplitudes, we tentatively explain the observed amplitudes by electrons coupling also strongly to acoustic modes with larger amplitudes in addition to optical modes. This behaviour will be analyzed in more detail by looking at the diffuse scattering intensities (Chapter 9).

Figure 25 b) shows the validation of the kinematical scattering approximation. In case of a perfectly fulfilled kinematical approximation, the negative logarithm of the relative peak intensities I_r^{hkl} at hot but near-thermal equilibrium (long pump-probe delays) is expected to depend linearly on the squared reciprocal lattice vectors G_{hkl}^2 and to cut the origin [80] (see Eq. 72). Deviations in the offset are accounted to multiple scattering of electrons, due to the finite thickness of the sample, which mainly results in an intensity redistribution from intense Bragg peaks to surrounding Bragg peaks [22].

The linear fit shown in 25 b) gives a small offset with a magnitude lower than the signal, indicating that the sample is thin enough to be treated in the context of kinematical approximation.

8.3 Breathing modes in MoS₂

Additionally to the DW-effect, peak dynamics exhibit an oscillation with a magnitude lower than the total intensity loss, which is not explained by the error margins. Oscillations are only visible in some Bragg peak dynamics, in particular in peaks with parallel lattice planes of peak families $\{030\}$, $\{120\}$ and $\{-240\}$. The analysis of these oscillations focused on the four peaks with the highest SNR, to ensure fit stability, as shown in Fig. 26. All observed oscillations are in phase. The pump-probe delay range for the fit has been cut to the time range where oscillations were visible (5 ps to 20 ps). A best fit was achieved by fitting the peak dynamics with a single exponential function convolved with a Gaussian kernel and subsequently fitting the residuals with an oscillating function. The parameterization for the exponential fit is:

$$f(\Delta t) = \Theta(\Delta t - t_0) \cdot A \left(1 - \exp \left[-\frac{(\Delta t - t_0)}{\tau} \right] \right), \quad (74)$$

similar to the biexponential fit parameterization (see Eq. 73). Residuals were fitted with:

$$r(\Delta t) = \Theta(\Delta t - t_0) \cdot f_{\text{gauss}}(\mu, \sigma) \cdot A_{\text{osc}} \sin \left(\frac{2\pi(\Delta t - \phi)}{T} \right) + c, \quad (75)$$

where A_{osc} is the oscillation amplitude, T the oscillation period and ϕ a phase shift. The Gaussian kernel is defined by the center μ and standard deviation σ .

The exponential fits show a very good agreement with the data, indicated by $R^2 > 0.979$. The pump-probe overlap t_0 was set to the value retrieved by analyzing the mean intensity from the previous section. Time constants τ obtained by the exponential fit are $\tau_{[300]} = (0.59 \pm 0.30)$ ps, $\tau_{[030]} = (0.57 \pm 0.30)$ ps, $\tau_{[120]} = (0.38 \pm 0.40)$ ps and $\tau_{[-240]} = (0.54 \pm 0.30)$ ps respectively.

The residuals of the $[300]$ and $[030]$ peaks show a wave packet shape, whereas the $[120]$ and $[-240]$ residuals show a damped oscillation, as presented in previous works studying coherent lattice dynamics in FED experiments [81, 82]. The damped oscillation shape is reached by shifting the center of the Gaussian kernel to smaller pump-probe delays. Peak $[030]$ reveals a small phase shift of the oscillation at 3 ps, which could not be explained by the fit model. Despite the low signal compared to the Debye-Waller dynamics, fits show a good agreement with the model. All fit parameters are shown in the appendix B. Here we focus on the extracted oscillation periods, which are $T_{[300]} = (8.4 \pm 0.5)$ ps, $T_{[030]} = (8.8 \pm 0.3)$ ps, $T_{[120]} = (7.6 \pm 0.2)$ ps and $T_{[-240]} = (7.6 \pm 0.1)$ ps, respectively. A position shift of Bragg peaks relative to the center of the diffraction pattern, that could possibly explain the oscillation, has not been observed.

The oscillations are best described through the strong excitation of lowest order longitudinal acoustic phonons. Those phonons are coherent breathing modes, which lead to an oscillation of the c-axis lattice constant [82–84]. The coherence of the phonons is underpinned by the in-phase oscillation and similar period of all Bragg peak signals. Furthermore, this effect modulates the crystal thickness with the period of the breathing mode, leading to an anisotropic oscillation of the crystal lattice. On a microscopic level, the effect on the Bragg peak intensities is best described in the context of diffraction theory by a change in the shape factor (Eq. 35) similar to Ref. [81]. The shape

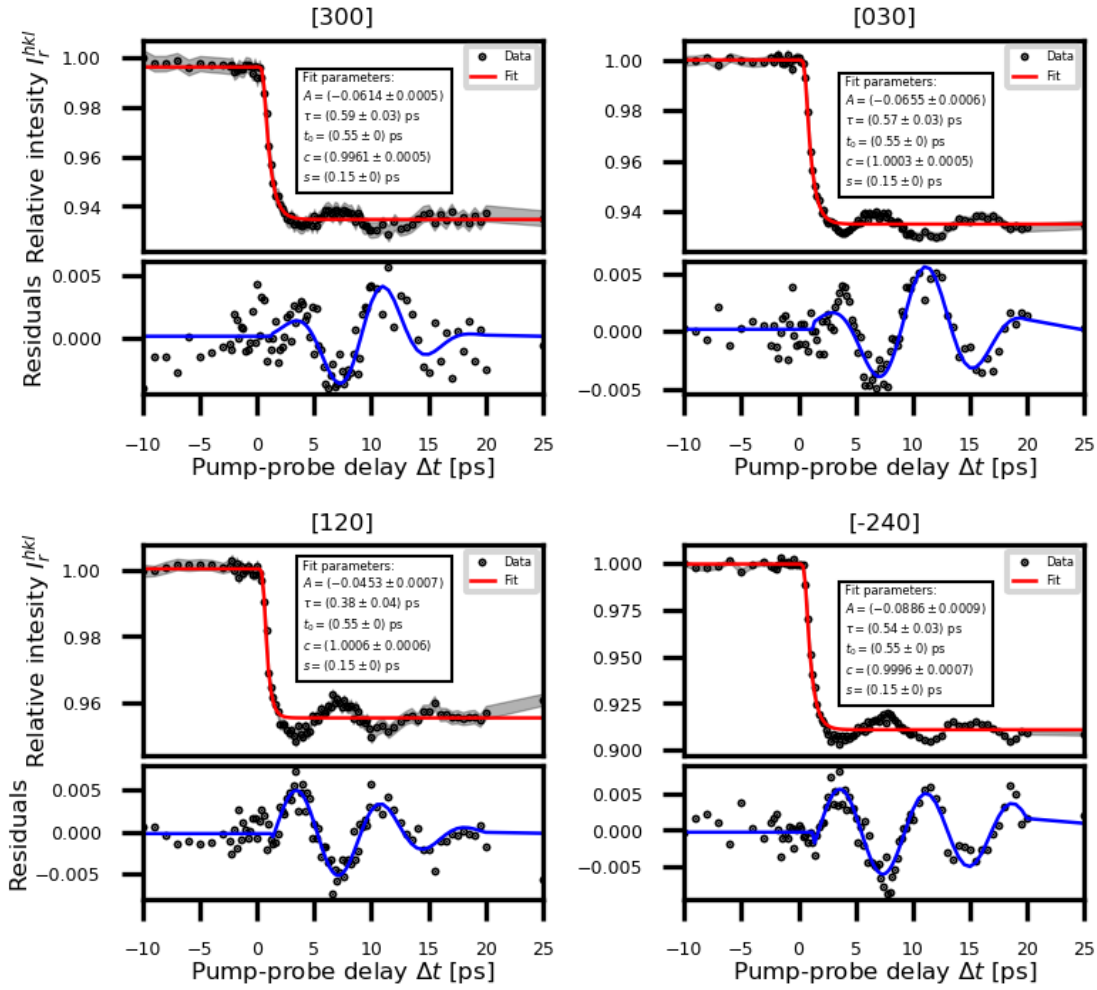


Figure 26: Bragg peak dynamics $I_r^{hkl}(\Delta t)$ of peaks [300], [030], [120] and [-240] respectively with residuals and their equal weighted fit. Shaded area around data points indicates the error based on the standard deviation. A deviation of zero indicates fixed parameters.

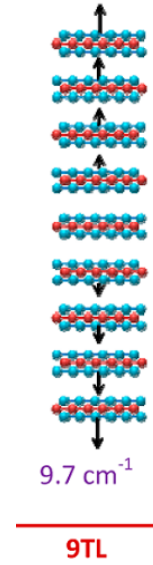
factor directly links Bragg peak intensities and lattice constants. Within the thin film effect (Eq. 35), Bragg peak intensities are only sensitive to the out-of plane direction. An oscillation of the out-of plane lattice constant $a_z = c \rightarrow c(\Delta t)$ thus introduces an oscillation in the reldods:

$$I_r(\vec{q}, \Delta t) = \frac{I(\vec{q}, \Delta t)}{I(\vec{q}, \Delta t < 0 \text{ ps})} \propto \frac{S(\vec{q}, c(\Delta t)) * S(\vec{q}, c(\Delta t))}{S(\vec{q}, c) * S(\vec{q}, c)}, \quad (76)$$

which modulates the intensity of Bragg peaks. Calculations of Eq. 76 for the [-240]-peak showed that we get similar intensity oscillations for lattice constant oscillation amplitudes in the order of 0.5 to 0.01 mÅ.

We show that the occurrence of coherent lattice oscillations may relate to the macroscopically large occupation of a single phonon mode close to Γ [86]. The weighted mean of the obtained periods is $\bar{T} = (7.7 \pm 0.8)$ ps, corresponding to a breathing mode

Figure 27: Illustration of the lowest order breathing mode B_{2g}^2 in MoS₂ from first principle calculations. Along the [001]-axis, longitudinal breathing mode shifts the layers such that, the c-axis lattice constant decreases and increases periodically. Black arrows indicate an increasing c-axis lattice constant. Image used from [85].



frequency of 0.13 ± 0.20 THz [$(4.3 \pm 0.5) \text{ cm}^{-1}$], is in good agreement with the B_{2g}^2 breathing mode from previous studies [85]. From the Gaussian envelope we can calculate a dephasing time, describing the decay of the coherent phonon population ($e^{-t/\tau_{\text{de}}}$) via $\tau_{\text{de}} = \sqrt{2}\sigma$, giving a weighted mean of $\tau_{\text{de}} = (6.5 \pm 0.6)$ ps. A recent study showed phonon dephasing times for different modes in bulk MoS₂ between 5.7 and 8.6 ps [87], but for different modes. The real space displacement of the crystal planes is shown in figure 27. Higher order breathing modes can be excluded, because they do not modulate the c-axis lattice constant by the same magnitude for every unit cell.

Assuming a freestanding crystal along the c-axis with open boundary conditions, we can calculate the sample thickness from the oscillation parameters, to see if it is consistent with our estimated thickness. Using the properties of the lowest order phonon mode, we can write its wavelength as $\lambda = 2d$, where d is the crystal thickness along the c-axis. For low energy phonons, the dispersion relation is linear and the velocity of sound is given by [22]:

$$v = \frac{w}{k} = \frac{\lambda}{T}. \quad (77)$$

Replacing the wavelength, we can write the thickness as function of breathing mode period and velocity of sound:

$$d = \frac{vT}{2}. \quad (78)$$

Using the measured cross-plane longitudinal sound velocity of MoS₂ from previous studies [88], $v = 7.11$ km/s, we find a thickness of $d = (27.3 \pm 0.3)$ nm. This shows a disagreement with the thickness of 40 to 50 nm estimated by light transmission, but the value is still in the overall expected thickness range.

The question remains of how the coherent phonon population influences the observed peak dynamics. Despite their influence on the rellods, coherent breathing modes should not directly influence the MSD and thus Debye-Waller dynamics. Only their decay into incoherent phonons should create a change in MSD, based on the decay channel. Since the observed breathing mode has a very low energy and momentum, decay channels are expected to be heavily constrained by energy and momentum conservation. A com-

parison of the timescales of DW-dynamics and damping of the oscillation shows, that the decay of coherent phonons is almost a magnitude slower than the DW-dynamics. In conclusion, we treat the effects of decaying coherent phonon modes on the DW-dynamics as insignificantly small.

9 Inelastic scattering analysis

The analysis is continued by extracting the inelastic scattering signals from diffraction patterns. This method is often mentioned as femtosecond electron diffuse scattering (FEDS) [17, 18, 20, 79] and provides momentum resolution additionally to time resolution. The momentum resolution is restricted to the 2D-BZ, determined by the reciprocal lattice vectors spanning the diffraction pattern. A detailed view of the inelastic scattering theory was given in Sec. 3.1.3. Diffuse scattering intensities $I_{\text{diff}}(\vec{q}, \Delta t)$ of MoS₂ are extracted by integrating intensities at every sampling point \vec{k} of each BZ. In the following text we neglect multi-phonon scattering and treat the intensities as one-phonon scattering intensities $I_1(\vec{q}, \Delta t)$. The key challenge in extracting inelastic diffraction intensities is to deal with their low SNR and the spatial distortions of the diffraction patterns. A detailed description of all corrections applied was discussed in Sec. 7.4.

9.1 Overview of inelastic signals

Diffuse scattering intensities sit on the large background arising from the tail of the transmitted electron beam. Thus an analysis of relative intensities, as used for Bragg peak intensities, would not work for the inelastic intensities. In this section, we focus on the extraction of intensity differences, which are mostly free from transmitted beam and Bragg peak tails. The resulting intensity difference maps $\Delta I_1(\vec{q}, \Delta t) = I_1(\vec{q}, \Delta t) - I_1(\vec{q}, \Delta t < 0)$ are shown in Fig. 28 for selected pump-probe delays.

On these maps, blue areas indicate decreasing intensities at the Bragg peak positions, which were analyzed in the previous section. We now focus on the areas with increasing intensity, indicated by the red signal. These areas contain the diffuse scattering signals and correspond to Eq. 37. Intensity difference maps reveal rising intensities at the BZ edges (K-M) for 600 fs pump-probe delay, which become stronger at 1 ps delay, outlining the hexagon shape of every BZ. At 2 ps and 5 ps delay, the signal intensity rises further, but also dissipates to the BZ centers. After 20 ps, no obvious changes are observed in the diffuse scattering signals.

The results shown in Fig. 28 directly demonstrate the non-thermal character of lattice thermalization in MoS₂. Based on the OPSF and OPC calculations in Sec. 5.4, we attribute the characteristic shape of strong intensity rises, which are best visible at 20 ps, to the shape of the OPSF contributions. A direct comparison of calculated intensity differences for the thermal equilibrium case is presented in Fig. 36. The OPSF features are reflecting the six-fold crystal symmetry of MoS₂ through the entire diffraction pattern, similar to the observed diffuse scattering signals. At larger pump-probe delays, characteristic features of the OPSF in the intensity difference start losing their strength, but are not completely disappearing.

The difference maps at 0.6, 1, 2 and 5 ps thus reflect the transient non-equilibrium states of the phonon system after photo-excitation. The strong rise of intensity differences at the BZ edges at 0.6 ps and 1 ps pump-probe delays reflects the non-equilibrium phonon populations generated by EPC. The dissipation of these diffuse scattering signatures into OPSF features is best explained by the relaxation of the phonon system

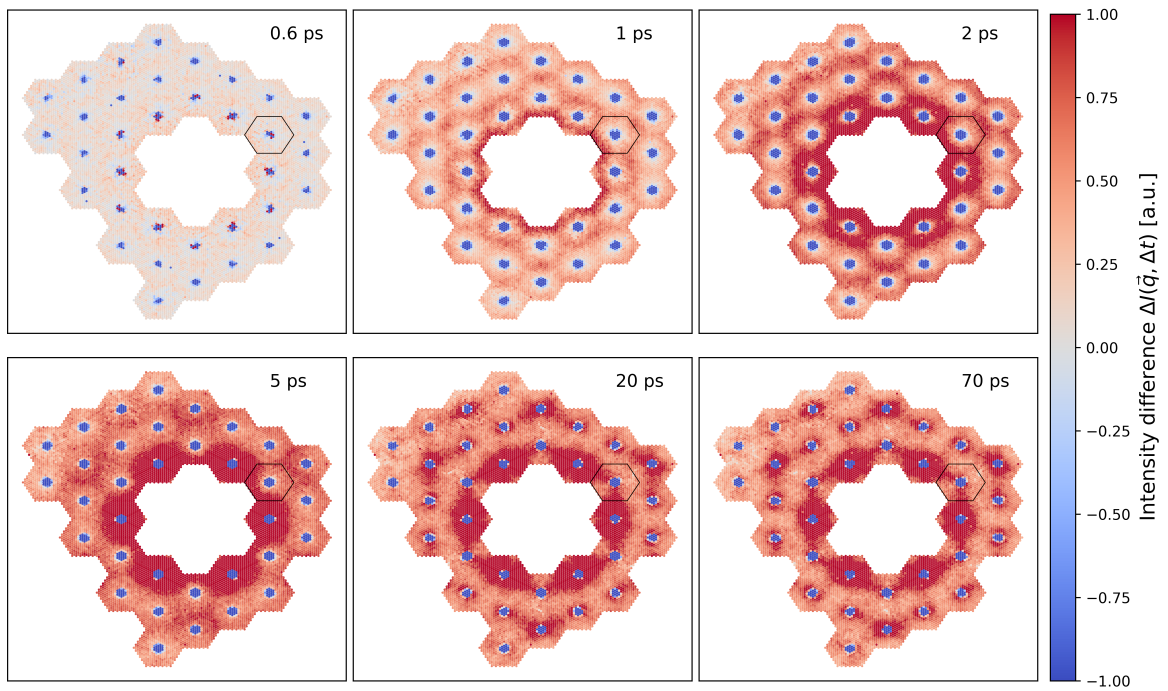


Figure 28: Overview of the evolution of the intensity differences $\Delta I_1(\vec{q}, \Delta t)$ of MoS₂ for selected BZs. The raw difference patterns were rotationally averaged (6-fold) for visualization purposes. Every BZ shown on the patterns will be sampled with a rotationally symmetric \vec{k} -grid based on a 18x18 Monkhorst-Pack grid (Fig. 23) with an integration window width of 6 pixels. Diffraction patterns are taken along the [001]-zone axis. Black hexagons mark exemplary first BZ.

into an equilibrium state with an elevated temperature via PPC. Since the OPSF features are best visible at 20 ps, we assign this state to a new thermal equilibrium of the phonon system, consistent with the observed elastic timescales. The slight decrease of the OPSF features for longer pump-probe delays is explained by the subsequent cooling of the lattice.

9.2 Quantification of inelastic signals

Due to the product of phonon population changes and OPSF in the individual branch contributions (see Eq. 37), it is not possible to obtain a detailed view of the phonon dynamics occurring from their population changes. A quantification of phonon dynamics across the available parts of the BZ is achieved by analyzing the relative intensity differences:

$$\Delta I_r(\vec{q}, \Delta t) = \frac{\Delta I(\vec{q}, \Delta t)}{\Delta I(\vec{q}, \Delta t = 20 \text{ ps})}, \quad (79)$$

and fit their individual evolution with a biexponential function, as used in the elastic scattering analysis (Eq. 73). Intensity differences are relative to their equilibrium intensity at 20 ps. Neglecting higher order phonon scattering and changes in the transmitted beam, we can rewrite the relative intensity differences as a function of OPC differences:

$$\Delta I_r(\vec{q}, \Delta t) \approx \frac{\Delta I_{1,\vec{q}}(\Delta t)}{\Delta I_{1,\vec{q}}(\Delta t = 20 \text{ ps})} = \sum_j \Delta n_{j,\vec{k}}(\Delta t) \frac{|F_{1,j}(\vec{q}, T)|^2}{\omega_{j,\vec{k}} \cdot I_{1,\vec{k}}(\Delta t = 20 \text{ ps})}. \quad (80)$$

In this expression, we neglected temperature-dependent changes in the OPSF $|F_{1,j}(\vec{q}, T)|^2$ and changes in the phonon frequencies $\omega_{j,\vec{k}}$. The observed signal at a reduced scattering vector \vec{k} is then the sum over all branches j of phonon population changes weighted with their OPSF and frequencies ($|F_{1,j}|^2/\omega_{j,\vec{k}}$), determining the sensitivity of the individual branches. Similar to the elastic signals, we get a better sensitivity for acoustic modes than for optical modes.

In theory, the changes in intensities $\Delta I(\vec{q}, \Delta t)$ are driven by the changes in phonon populations $\Delta n_{j,\vec{k}}(\Delta t)$. Since all properties of phonons can be described inside the 1.BZ [23, 89], it is also possible to describe all phonon population changes within the 1.BZ. Hence every BZ around every Bragg peak should reflect redundant population changes, fully described by the reduced scattering vector \vec{k} . Furthermore, population changes inside every BZ should reflect the crystal's n-fold symmetry, 6-fold symmetry for MoS₂.

In practice, however, we do not observe fully sixfold symmetric relative intensity differences $\Delta I_r(\vec{q}, \Delta t)$ in most BZs. We explain this by the different SNR within the different parts of the BZ. The strength of our signal is defined by the weights $|F_{1,j}(T, \vec{q})|^2/\omega_{j,\vec{k}}$ of the individual branches j , with $\omega_{j,\vec{k}}$ being also redundant for every BZ similar to $\Delta n_{j,\vec{k}}(\Delta t)$. In contrast, the OPSF $|F_{1,j}(T, \vec{q})|^2/\omega_{j,\vec{k}}$ introduces a dependence on the scattering vector \vec{q} , conserving the n-fold symmetry of the entire diffraction pattern, but not the n-fold symmetry of the individual BZs. In principle this should not be relevant for relative intensity difference evolutions. But if the signal drops below the noise level in some areas due to low OPSF magnitudes in most branches, this leads to a low SNR in these areas. Hence some parts of the BZ are more sensitive to the same phonon population changes than others.

In the recent literature, analysis of the time-resolved diffuse scattering intensities focused on individual BZs with strong diffuse scattering signals along a chosen \vec{k} -path [18, 19, 21]. In this work, a different approach is used. It is assumed that inelastic signals of most k-points within a given BZ, provided they are far enough from the zone center, are strong enough to exhibit an undistorted diffuse signal. Additionally we

assume that this condition is valid for most of the analyzed BZs. These assumptions are supported by the strong OPSF-features observed in Fig. 28, indicating that we are able to extract useful diffuse scattering signals in most parts of the diffraction pattern and not only along specific \vec{k} -paths.

Based on that, an additional 6-fold rotational averaging of the individual BZ signals is applied, owing to the 6-fold symmetry observed in the relative intensity differences, see Fig. 26. Furthermore, it is possible to average over all BZs and reduce the relative intensity difference evolution to the evolution of a single BZ. This step is similar to rotationally average the weights of the branch contributions.

Let $\{\vec{k}_m\}$ be a set of n-fold rotationally symmetric reduced scattering vectors. Then we can write the n-times rotationally averaged intensity difference $\Delta\bar{I}_p(\vec{k}, \Delta t)$ within the BZ p as:

$$\begin{aligned}\Delta\bar{I}_p(\vec{k}, \Delta t) &= \frac{1}{n} \sum_{m=1}^n \Delta I_p(\vec{k}_m, \Delta t) \\ &= \frac{1}{n} \sum_{m=1}^n \sum_j \Delta n_{j,\vec{k}}(\Delta t) \frac{|F_{1,j,p}(\vec{k}_m)|^2}{\omega_{j,\vec{k}}} \\ &= \sum_j \frac{\Delta n_{j,\vec{k}}(\Delta t)}{\omega_{j,\vec{k}}} \frac{1}{n} \sum_{m=1}^n |F_{1,j,p}(\vec{k}_m)|^2.\end{aligned}\tag{81}$$

This method has the disadvantage, that low-signal areas are averaged with high-signal areas. But it provides a more robust extraction of the inelastic signals, due to the sheer amount of available BZs. Additionally, a complete view of diffuse scattering signals across the entire BZ is achieved. A more sophisticated analysis could be developed in the future by only averaging BZ areas which have signals higher than a defined limit. In total, 30 BZs were used, excluding 4 of the outermost available BZs (e.g. [4-40]) due to their low signal, to calculate the relative intensity difference evolution. The time-resolved inelastic signal at each k-point on the grid was fitted with a biexponential function (Eq. 73), using a fixed electron pulse with of $s = 150$ fs and a global pump-probe overlap $t_0 = 0.517$ ps, obtained by first fitting all time traces with a variable overlap and taking the average. The resulting amplitudes and time constants across the BZ are shown in Fig. 29.

9.2.1 Phonon dynamics around the Brillouin zone edges

To analyze the momentum-resolved phonon dynamics, we proceed to a partitioning of the BZ into two zones, indicated by the dashed hexagon on Fig. 29. The first zone includes areas around the BZ edges, that have a positive amplitude A_1 corresponding to the fast time constant τ_1 and a negative amplitude A_2 corresponding to the slow time constant τ_2 . That zone includes the high-symmetry points K and M and spans from the BZ edges to roughly half the Γ -M distance. The CBM at Λ_{\min} is not included. Inside the first zone, the fit amplitudes shown in Fig. 29 a) and b) display a qualitatively similar behaviour, with slightly higher amplitudes around the K point and lower magnitudes below M. Both fit amplitudes decrease to the edge of the first zone

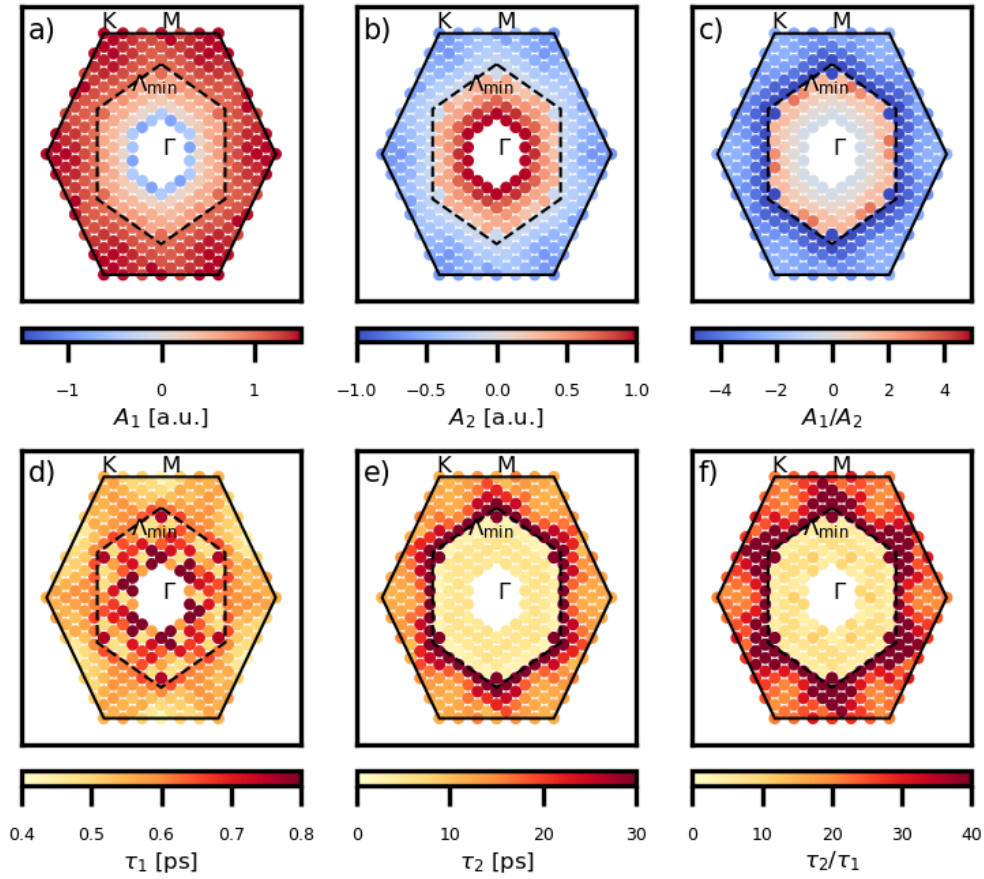


Figure 29: a), b) Amplitudes and d), e) time constants of biexponential fitted relative inelastic intensity differences $\Delta I_{1,r}(\vec{k}, \Delta t)$ for sampling points based on a 18x18 Monkhorst-Pack grid. c) and f) show the ratios of amplitudes and time constants respectively. The dashed hexagon shows the separation between the outer first zone and the second inner zone. Redundant values inside the BZ are displayed, due to the 6-fold symmetry of MoS₂.

(going towards the zone center). The fast time constant τ_1 shows decreased magnitudes around M and rather constant magnitudes in the rest of the first zone. The slow time constant τ_2 shows the inverted behaviour compared to τ_1 , with higher magnitudes below M and lower magnitudes around K. Both areas exhibit an increase to the edge of the first zone towards Γ .

Exemplary fits of sampling points inside the first zone are shown in Fig. 30 a), b) and c). The fits of the high-symmetry points K and M are shown in a) and b), respectively. Both fits reveal a strong rise of $\Delta I_r(\Delta t, \vec{k})$ in the first few picoseconds after photoexcitation, modeled by a positive amplitude A_1 and a fast time constant τ_1 in the order of a few hundred femtoseconds. The subsequent decay of $\Delta I_r(\Delta t, \vec{k})$ is modeled by the second exponential term with a negative amplitude A_2 and a slower time constant τ_2 in the order of a few picoseconds. A comparison of the fit amplitudes A_1 and A_2 reveals that $A_1 > A_2$ for K and M. A constant elevated level of $\Delta I_r(\Delta t, \vec{k})$ is reached after ~ 40 ps. This is qualitatively consistent with the raw diffuse scattering signals observed in Fig. 28.

Since all areas in the first zone show a positive A_1 and a negative A_2 , variations in the evolution can be modeled by the ratios of amplitudes and time constants, shown in Fig. 27 c) and f) respectively. The A_1/A_2 ratio decreases from the BZ edges to the edge of the first zone, indicating that the drop of $\Delta I_r(\Delta t, \vec{k})$ after the first fast increase gets smaller for areas closer to Γ .

Additionally, the ratio τ_2/τ_1 increases in the same areas, showing that lower amplitude ratios result in slower dynamics of the second exponential term. Variations are mainly caused by τ_2 , since τ_1 shows only little variations in the first zone, covering values from 0.4 ps to 0.6 ps. Larger values are observed around K being almost constant around the K- Γ line inside the first zone. Lower values are observed around M, which are increasing with increasing distance to M. In contrast to τ_1 , the slow time constant τ_2 covers a spectrum from 11 ps to values greater than 100 ps, which is the fit boundary. These large values can be observed visually by looking at the exemplary fits.

An exemplary fit for regions with small A_2 and large τ_2 is shown in Fig. 30 c). The inset shows that the sampling point is close to the inner edge of the first zone, where A_2 is almost zero. After the initial increase of $\Delta I_r(\Delta t, \vec{k})$ follows a small decrease, reaching a constant level for pump-probe delays > 100 ps. Compared to the high-symmetry points K and M, the second exponential time constant $\tau_2 = (36 \pm 8)$ ps is significant slower. Whereas τ_1 shows only a small increase of 100 fs. Very large values of τ_2 at the inner edge of the first zone are accounted to the almost mono-exponential evolution of $\Delta I_r(\Delta t, \vec{k})$. If A_2 is negative but very close to zero, the decay appears to be almost constant and is thus modeled with a very large time constant with high variance.

A link between momentum-resolved lattice dynamics and relative intensity differences $\Delta I_r(\Delta t, \vec{k})$ is established by the dependence on phonon population changes. The weights of individual branch contributions $|F_{1,j}|^2/\omega_{j,\vec{k}}$ can be used to set boundaries in the interpretation, since non-active branches ($|F_{1,j}|^2 \approx 0$) do not contribute to the observed signal and acoustic contributions are better visible.

The two time constants in the exponential fits are assigned to two different processes leading to a rise and decay of phonon populations in the first zone. Based on the elastic analysis, we assign the fast rise to EPC and the second slower decaying term to PPC.

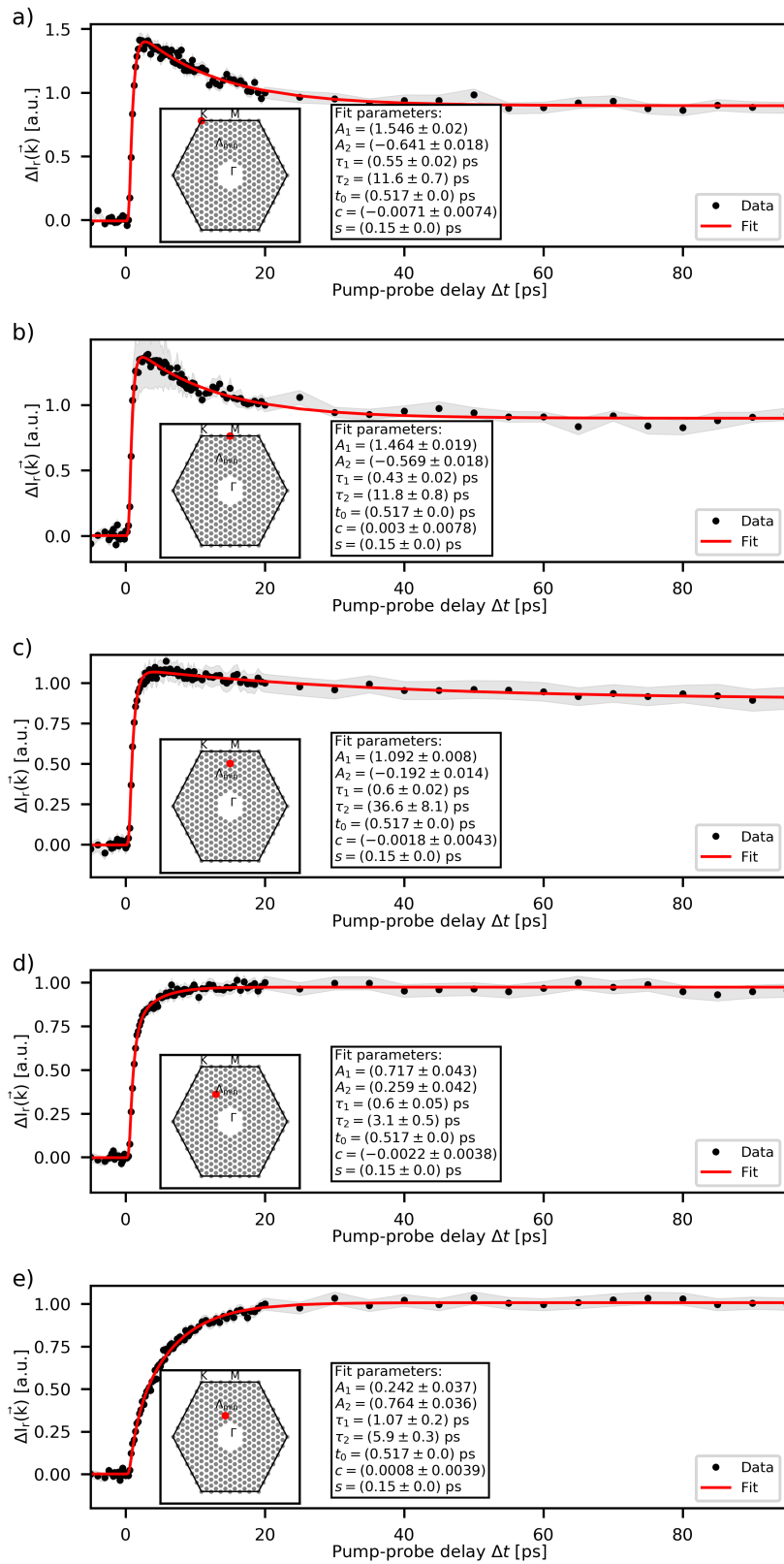


Figure 30: Exemplary non-weighted fits of selected sampling points inside the 1.BZ for MoS₂ with standard deviation given by shaded areas. The sampling point position inside the 1.BZ is indicated by the red dot in the first inset. The second inset shows the fit parameters.

The increase of phonon populations modeled by the EPC-term accounts for phonons emitted by electronic transitions in the VB and CB, generating a non-equilibrium phonon distribution. The subsequent equilibration of the lattice by phonon-phonon scattering is modeled by the PPC-term.

Electronic transitions can be divided into two types, intravalley and intervalley transitions [52]. Intravalley transitions are transitions connecting two electronic states in the same momentum space area, mostly high-symmetry points, which result in the emission of low-momentum phonons close to Γ . Due to the high Bragg peak intensities at Γ we are not able to observe inelastic diffraction signals of those processes. Phonon dynamics at the Γ point are best observed by complementary methods such as time-resolved Raman spectroscopy, but this goes beyond the scope of this thesis.

Intervalley transitions are defined as transitions connecting two electronic states of different valleys or hills in the CB or VB, resulting in the emission of large-momentum phonons. Transitions across the gap are forbidden due to energy conservation. In the experiments presented here, the tail of Bragg peaks limits the observable momentum range to processes with phonon momentum ranging from 0.45 \AA^{-1} up to the BZ edges. Characteristic for the first zone is, that all sampling points exhibit a positive amplitude of the EPC-term and a negative amplitude of the PPC-term, which has the smaller magnitude. This behaviour is best explained by the phonon population at \vec{k} being driven out of equilibrium by EPC and relaxing to its equilibrium level at an elevated temperature by PPC. Hence the first zone could be renamed as strong electron-phonon coupling zone.

To what extent the phonon population at \vec{k} is driven out of equilibrium is reflected in the slow amplitude and time constant. Small negative amplitudes with large time constants indicate that the phonon population already had reached its elevated equilibrium population by EPC. Whereas large negative amplitudes and small time constants of the PPC-term indicate that these areas are strongly driven out of equilibrium, overshooting the elevated equilibrium population. These areas are interpreted as strongly-coupled areas, in terms of EPC.

We can distinguish the coupling strength best by looking at the amplitude and time constant ratios. Low values of these ratios indicate strong coupling. The strongest coupling is observed at regions around K, whereas regions around M exhibit weaker coupling. As shown in Fig. 30 a) and b), sampling points covering the high-symmetry points K and M exhibit mostly identical dynamics. The coupling strength is decreasing as regions come closer to the edge of the first zone.

A comparison of the strongly-coupled areas with the momentum-integrated elastic diffraction signals (Chapter 8) shows that the EPC time constants, 420 - 560 fs and (470 ± 20) fs respectively, are consistent, indicating that the strongly-coupled areas dominate the momentum integrated EPC-signal observed in the Bragg peak dynamics.

9.2.2 Phonon dynamics around the Brillouin zone center

The second zone includes \vec{k} -points between half Γ -K (or half Γ -M) and the cut Γ -area. It is defined by the interior of the dashed hexagon shown in Fig. 27. The CBM Λ_{\min} is included in the second zone at its border to the first zone.

The observed signals are completely different from those observed in the first zone.

The fit amplitudes A_1 and A_2 , shown in Fig. 29 a) and b) respectively, are positive in most parts of the second zone. The magnitude of A_1 decreases as the distance to Γ decreases, and vice versa for A_2 . In regions near the cut Γ -area, the second amplitudes are dominating with $A_1 < A_2$, as indicated in the amplitude ratios shown in panel c). The negative amplitudes of A_1 around the cut Γ -area are attributed to an overlap with the Bragg peak intensities and we do not discuss them further.

The features observed in the fast time constant τ_1 , seen in Fig. 29 d), have to be interpreted with care. The variations of τ_1 are much greater than those observed in the first zone, covering magnitudes from ~ 450 fs to 1.1 ps. Especially areas around the CBM Λ_{\min} show higher magnitudes than areas between Γ and half Γ -M. These variations could be artificial, since the signal rises can also be captured by a single exponential term which accounts for all processes. In this second zone, EPC signals are so weak that they cannot be well separated from the PPC signals. A further separation between single and biexponential fitting should be implemented in the software.

The slower time constant τ_2 (e) shows magnitudes of ~ 2 ps at all border points except one point at half the Γ -M distance, which has a magnitude of 30 ps. All other sampling points between the border and Γ do not show a characteristic pattern and range between ~ 4 ps and 6 ps. The time constant ratios, shown in panel (f), mainly reflect the pattern of τ_1 , since the τ_2 values are relatively constant.

Two exemplary fits inside the second zone are shown in figures 30 d) and e). Panel d) shows the fitted relative intensity difference evolution of the sampling point closest to Λ_{\min} . This signal is characteristic for most points of the outer second zone edge. The EPC term is the dominating term due to $A_1 > A_2$. Instead of decreasing the amplitude, the PPC term is also contributing to the intensity rise indicated by its positive amplitude A_2 . The fast EPC term time constant $\tau_1 = (600 \pm 50)$ fs is ~ 100 fs slower than the momentum integrated elastic EPC signal (Sec. 8), indicating that most of the EPC processes observed at Λ_{\min} do not dominate the momentum integrated EPC processes. A comparison of the PPC time constant $\tau_2 = (3.1 \pm 0.5)$ ps with the momentum integrated PPC time constant $\tau_{2,el} = (2.8 \pm 0.2)$ ps shows that the phonon equilibration in the CBM is quite similar to the momentum integrated phonon equilibration.

Figure 30 e) shows the relative intensity difference evolution of phonons close to the cut Γ -area and close to the Γ -K line. The most characteristic features of these areas are the amplitude ratios $A_1 < A_2$, showing that the PPC term is now dominating the phonon equilibration. The EPC time constant $\tau_1 = (1.1 \pm 0.2)$ ps is relatively slow compared to other areas in the first zone as previously described. The slow time constant is an indicator that the EPC generating phonons at those areas is much less likely to happen. The same holds for the second time constant $\tau_2 = (5.9 \pm 0.3)$ ps, which is a few picoseconds slower than the momentum integrated PPC signal.

Summarizing all this information, we can say that the EPC in the second zone is generally slower and weaker than the coupling in the first zone. The relaxation of the phonon system at low-momenta is driven by the EPC and PPC terms, that are both leading to an increase in phonon population. The double increase is best explained by phonons being first generated through EPC, generating a phonon population below its elevated equilibrium population (given by the BE-statistics). The subsequent second rise is best explained through the decay of high-energy modes into low-energy and low-momentum

phonons, restoring the equilibrium population. Additionally, we observe a transition from EPC dominated phonon generation to PPC dominated phonon generation for decreasing momentum, as indicated by the amplitude ratios.

Most interesting features are observed in the EPC time constant, which are significantly increased at areas around the CBM Λ_{\min} , building a light star-like shape of increased time constants. It remains the question of the origin of the sharp feature.

10 Towards branch-resolved inelastic scattering analysis

In this section, we extend the analysis of diffuse scattering intensities presented in Sec. 9 by implementing the branch-resolved approach introduced in a recent FEDS work on graphite by De Cotret et al. [20] and introduced in Sec. 3.2. We discuss the influence of the approximations made in this approach, the sensitivity of the experiment to signals generated by individual branches and the merging of calculated and experimental intensity difference maps. Additionally, the influence of diffuse multi-phonon scattering is discussed and compared to recent studies. Finally, the results of the time-, momentum- and branch- resolved approach are discussed and compared to the more established elastic and inelastic scattering dynamics presented in Sec. 8 and 9.

10.1 Self-consistency test on MoS₂

Before applying the branch-resolved approach to MoS₂, we carry out the self-consistency test to detect multicollinearity in the equation system of Eq. 38, as presented in Sec. 6. In this section, we first apply the method of the variance inflation factor (VIF) to determine where multicollinearity occurs in the case of MoS₂. Next, we perform a binning of the phonon branches into effective branches, and we check again the VIF. The OPSF contributions used in the self-consistency test are based on the ab initio calculations presented in Sec. 5.3 and 5.4.

10.1.1 Multicollinearity of one-phonon structure factor contributions

Similar to section 6.2, the multicollinearity of the OPSF branch contributions are estimated by calculating their variance inflation factor maps $VIF_j(\vec{k})$. Figure 31 shows the $VIF_j(\vec{k})$ for all branches of MoS₂. In the literature, a VIF value of 5 to 15 indicates high multicollinearity [58]. Our calculations show that all active branch contributions of the OPSF contain highly multicollinear areas, indicated by VIF-values far above 15. As presented in the self-consistency tests on graphene (section 6.4), these areas cause instabilities of the solution, resulting in extremely high or low phonon temperatures. The solutions retrieved using all phonon branches are shown in the appendix D and are not further discussed due to their unreliability.

If VIF patterns of one branch are also visible in neighbouring branch contributions, it is an indicator that those branches are collinear or multicollinear to each other, e.g. branch contributions 1, 2 and 3. All of them have high VIF values around M. The observed similarities of VIF patterns are later used in the phonon branch binning processes to reduce multicollinearity. In addition to the similar patterns around M for branches 1, 2 and 3, the VIF pattern observed in branch 3 also shows similarities with those of branches 4, 5 and 6. All of them show a similar pattern of high VIF areas around K and on the Γ -M line. Branches 7 and 8 are completely inactive and are not relevant for reducing multicollinearity. Branches 9 and 10 show high VIF values at K. These values result from small OPSF contributions in the K-area. The VIF patterns of the optical branches 11 and 12 show high similarities, indicated by a high VIF area around Γ and along the Γ -M line. Branch 13 shows high VIF values in almost every available area of the BZ, thus a clear assignment to another branch is not possible. Branch 14 is assigned to branch 12, due to the dotted line of high VIF values along the Γ -K line. The last four branches can be assigned very easily due to their very similar patterns. Branches 15 and 16 as well as 17 and 18 show almost pairwise identical VIF patterns. Furthermore, both pairs of branches show high similarities due to their high VIF areas around Γ , on the Γ -M line and around K. Given these results, it is clear that phonon branch binning is required for MoS₂.

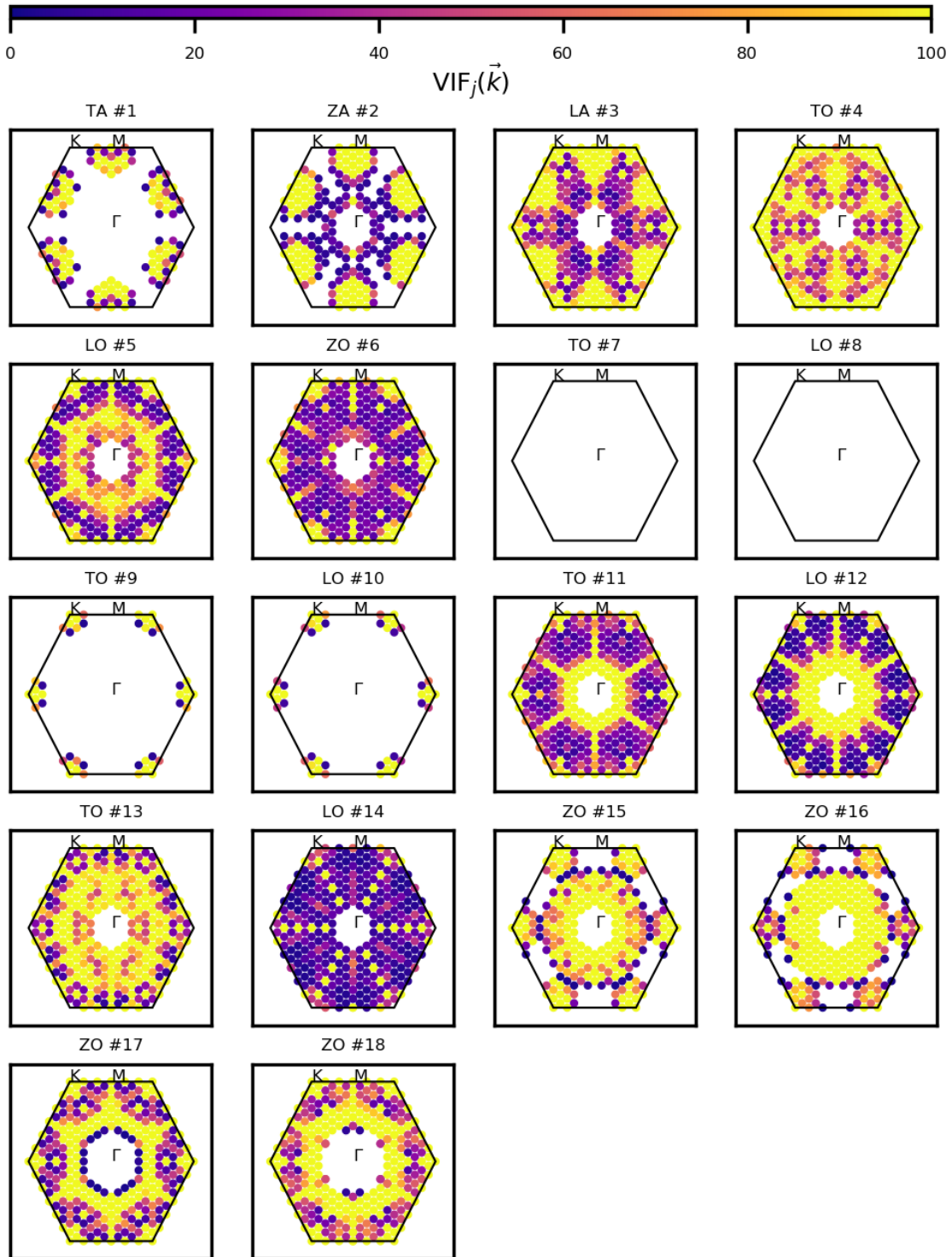


Figure 31: Branch-resolved variance inflation factor maps $VIF_j(\vec{k})$ for MoS₂. Empty spaces indicate non-contributing areas, where no VIF can be defined. VIF maps of branches are sorted according to the phonon energy at Γ , starting with the lowest energy branch.

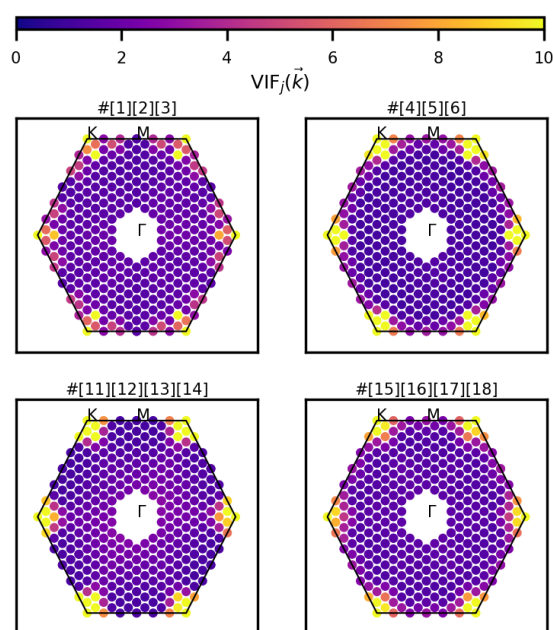
10.2 Phonon branch binning on MoS₂

In this section, the phonon branches of MoS₂ are binned to effective branches in order to reduce the multicollinearity of the equation system (Eq. 38). The best binning of branches is discussed on the basis of the VIF and checked by the results of the self-consistency test. The phonon branches of MoS₂ are binned in such a way that the multicollinearity of the equation system is most effectively reduced, while also minimizing the frequency differences of the binned branches. The goal is to achieve low VIFs in most areas of the BZ and in all effective branches, while also keeping the number of effective branches as high as possible, since every binning decreases the branch-resolution. As for graphene, an effective binning is achieved by binning branches which show high similarities in their VIF patterns.

Before starting the binning process, we exclude branches 7 and 8 which are inactive. Branches 9 and 10 are also excluded due to their very low contribution to diffuse scattering. Starting with the lowest energy branches, a best reduction of multicollinearity is achieved by binning the three acoustic branches 1, 2 and 3, due to their very similar VIF patterns. Since branches 1 and 2 are degenerated and branch 3 has similar frequencies, deviations in the effective electron-phonon coupling are expected to be small. The remaining branches 4, 5 and 6 of the low energy phonon band are binned, due to the same reasons. Branches 5 and 6 are also degenerated.

The remaining high-energy phonon branches consist of 4 pairs of degenerated branches, [11,12], [13,14], [15,16] and [17,18]. Based on the similarities of their VIF-patterns, we binned the first two pairs into an effective branch, and the last two pairs into another. Since frequency spreads between the pairs are larger, we expect stronger deviations from their true coupling to electrons. A pairwise binning of degenerated branches did not show sufficient good results in the self-consistency test. The VIF maps of the four effective branches are shown in figure 32.

Figure 32: Variance inflation factor maps $VIF_{\tilde{j}}(\vec{k})$ for every effective branch \tilde{j} of MoS₂.



The four effective branches can be distinguished in two low energy branches and two high energy branches. All of them show VIFs < 4 in all available regions of the BZ, except a small region around K, where most distortions due to multicollinearity are expected. Unluckily, strongest electron-phonon coupling is expected in that region, see Sec. 9.2 and Ref. [52]. Inactive regions inside the BZ have been eliminated due to the branch binning. Finally, the self-consistency test (see Sec. 6) is conducted by using the set of effective phonon branches. The experimental intensity difference in the equation system of Eq. 38 is replaced with the calculated OPC differences in thermal equilibrium with a temperature difference of $\Delta T = 190$ K and the initial temperature is set to $T_1 = 300$ K. The equation system is solved with a standard implementation of the NNLS algorithm as implemented in the *scipy*-package [37]. The calculated temperatures from the phonon population differences are shown in Fig. 33.

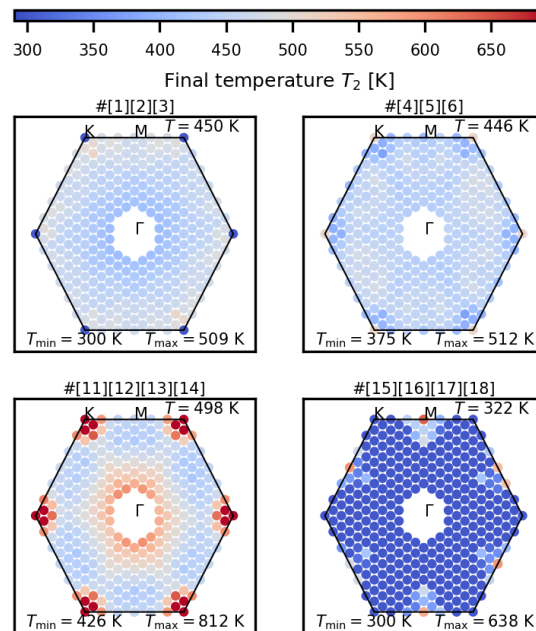


Figure 33: Final equilibrium temperatures T_2 obtained by the self-consistency test for MoS₂. Average, minimum and maximum temperature of effective branches are shown in their inset. Grey areas correspond to $T_2 = 490$ K.

The temperatures obtained by the self-consistency tests for the effective branches show a much better agreement with the ideal final temperature $T_2 = 490$ K, than with the complete set of branches. As discussed in Sec. 3.2.1, we see a general underestimation of temperatures in most areas. The first effective branch, consisting of acoustic branches [1,2,3], exhibits strongest deviations at the K-point, most likely a result of remaining multicollinearity. All other points show a good agreement with the ideal temperature, with values ranging from $T_2 = 420 - 509$ K. Similar temperatures are observed in the second effective low energy branch, consisting of branches [4,5,6]. The strongest deviations are located in a small area around K.

The results of the first effective high energy branch, consisting of branches [11,12,13,14], show more deviations than the effective low energy branches. Regions around Γ and

K overestimate the true temperature, while other areas underestimate them. Here also, the strongest deviations occur in an area around K. The shape of the area is identical to the overlaid shape of negative temperature deviations of the effective low energy branches. In conclusion, it is likely that the least squares solver transferred the phonon populations from the effective low energy branches to the first effective high energy branch, due to multicollinearity in these areas. The second effective high energy branch, consisting of branches [15,16,17,18], shows no temperature changes in most areas, indicated by the initial temperature of 300 K. This effect is attributed to the almost inactive areas of those branches, which are not populated by the NNLS solver. Only active areas around M exhibit underestimated temperatures.

In conclusion, the results of the self-consistency test on MoS₂ highlight the general problem of the time-, momentum- and branch-resolved approach in the presence of multicollinearity and calls into question its applicability for non-equilibrium and equilibrium states. Nevertheless, we were able to reduce the multicollinearity of the optimization problem to a satisfactory level by binning the phonon branches of MoS₂ into effective branches, based on their frequencies and VIFs.

10.3 Sensitivity of the experiment to effective phonon branches

In this section, we discuss the sensitivity of the experiment to changes in phonon populations in the effective phonon system. Since phonon frequencies and OPSFs are accessible by ab initio calculations, it is possible to determine the sensitivity of the experiment to changes in phonon populations. From Eq. 37 the sensitivity of a branch j at scattering vector \vec{q} on the diffraction pattern can be defined by:

$$S_j(\vec{q}, T) = \frac{|F_{1,j}(\vec{q}, T)|^2}{\omega_{j,\vec{k}}}, \quad (82)$$

with $|F_{1,j}(\vec{q}, T)|^2$ the OPSF of branch j and $\omega_{j,\vec{k}}$ its frequency. The sensitivity determines how much inelastic scattering signal each branch generates at \vec{q} , if its phonon population changes by one.

As inelastic scattering signals are averaged over every BZ and additionally rotationally averaged (see Sec. 9.2), we apply the same procedure to the sensitivity mapping. Thus the sensitivity of the whole diffraction pattern of a branch is reduced to the sensitivity of this branch within the 1.BZ, $|S_{1,j}(\vec{q}, T)|^2 \rightarrow |\bar{S}_{1,j}(\vec{k}, T)|^2$. When phonon branches are binned into effective branches, this is taken into account by summing the individual sensitivities to an effective branch sensitivity. The sensitivity of an effective branch l can be written as:

$$S_l(\vec{q}, T) = \sum_{m \in [j\dots l]} \frac{|F_{1,m}(\vec{k}, T)|^2}{\omega_{m,\vec{k}}}, \quad (83)$$

with $[j\dots l]$ being a set of binned branches. The calculated sensitivity for all 4 effective phonon branches of MoS₂ at $T = 300$ K is shown in Fig. 34.

The first three effective low energy branches show a good sensitivity in all parts of the available BZ, ranging from 30 to 100 % of the maximum sensitivity. Each branch exhibits small variations in sensitivity that are generated by the OPSF patterns. The last effective branch, consisting of the four highest energy optical branches, shows a

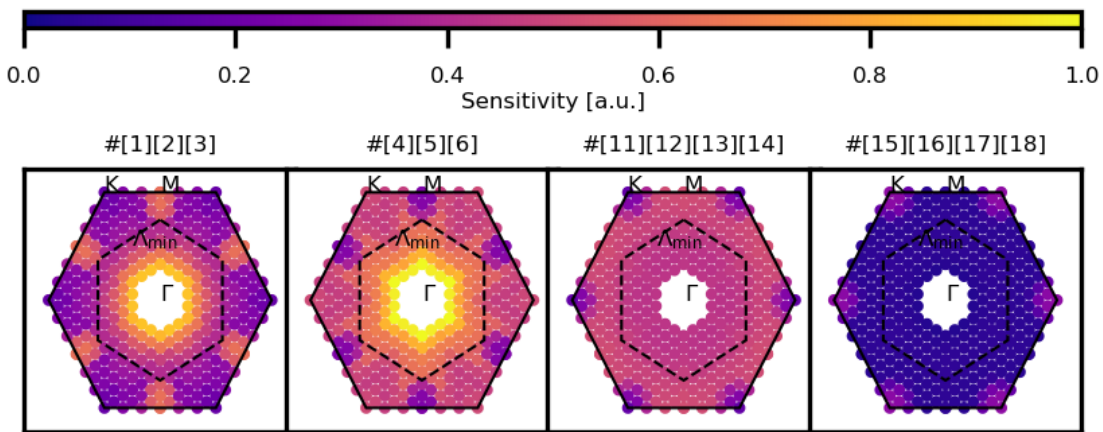


Figure 34: Sensitivity to phonon population changes of effective branches within the 1 BZ for MoS₂ normalized to the maximum value of all branches. Binned phonon branches are given above the figures. Effective branches are sorted, starting with lowest energy. Dashed line indicates separation of first and second zone as used in the inelastic analysis (see 9.2)

significant sensitivity only around the K point. All other parts of the BZ exhibit almost no sensitivity to phonon population changes. That pattern is a result of the very localized OPSF contributions that are almost inactive except for the area around K, see Fig. 8.

In conclusion, we see that the branch resolution of the approach is additionally reduced to 3 effective branches in most parts of the available BZ. Only a small area around K exhibits a good sensitivity to all effective branches, however we also saw that the K-region exhibits high multicollinearity.

10.4 Merging model and experimental intensities

Having performed the self-consistency test and branch binning, the next step is to merge the model and experimental data by matching their intensity magnitudes. A first approach could be to scale the intensities by the intensity of a single scattering event, i.e. by dividing $I_1(\vec{q})$ with the sample and setup parameters. For this, the model intensity would have to be divided by the number of unit cells N that diffract the electron beam. This number is given by the supercell size used in the calculations. However, the main problem with this approach arises from transforming the experimental intensities. In the experiments, N depends strongly on the crystal thickness and spatial width of the probe pulse. Both parameters are unknown and can only be estimated. Furthermore, we would need an exact knowledge of how many electrons are in each pulse and of the intensity generated by one electron on the detector. These parameters are calculated in the normalization procedure to account for fluctuations in the electron pulse intensities. They are sufficient for determining the dynamics, but still have deviations in their magnitude due to the non perfect quantum efficiency and non-linear behaviour of the detector for high intensities, as they occur in the zero order and Bragg peaks. To account for all these parameters quantitatively is currently impossible.

A better approach is to adapt the model intensity $I_{1,model}(\vec{q}, T)$ at the initial temperature to the experimental intensity in thermal equilibrium $I_{1,exp}(\vec{q}, \Delta t < 0 \text{ ps})$, by fitting $I_{1,model}(\vec{q}, T) = \lambda \cdot I_{1,exp}(\vec{q}, \Delta t < 0 \text{ ps})$. Instead of determining the experimental parameters, only one scaling parameter λ has to be calculated. The experimental and simulated intensity maps for the initial states are shown in Fig. 35. Panel a) shows the simulated OPC of MoS₂. In panel b), displaying the experimental pattern, the inelastic signals are overlaid with a large radially symmetric intensity, which originates from the tail of the transmitted electron beam (0th order beam). To apply this approach, the one-phonon contribution would thus have to be extracted by subtracting the tail of the transmitted beam. This is challenging, since the 0th order tail and the one-phonon contributions cannot be distinguished easily. Indeed both contributions decrease with increasing scattering vector. Hence a fitting of the rotationally averaged intensities, as is commonly used in the baseline removal of powder diffraction experiments [90], is here not possible.

In the limit of kinematical theory, the loss of the transmitted beam is equal to the

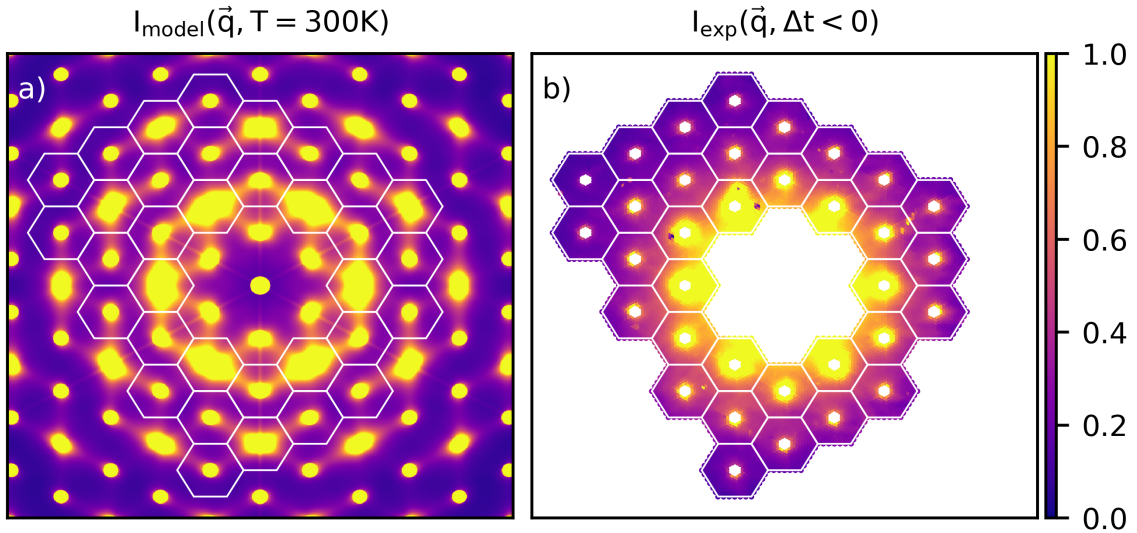


Figure 35: Comparison between model and experimental intensities $I(\vec{q}, T)$ in thermal equilibrium. White hexagons incate 1 BZs accessible by the experiment. a) Calculated intensity of the zero-phonon and one-phonon contributions $I_{model}(\vec{q}, T) = I_0(\vec{q}, T) + I_1(\vec{q}, T)$ for the initial temperature $T = 300K$. The characteristic features between the Bragg peaks generated by the one-phonon contribution are clearly visible. b) Initial intensity $I_{exp}(\vec{q}, \Delta t < 0)$ for negative pump probe delays with cut Bragg peaks. The one-phonon contribution is hidden by the large background from the 0th order tail.

increase of Bragg peak intensities [22]. This loss mainly depends on the crystal size, electron energy and atomic form factors, but does not depend on the crystal temperature. A temperature change results in an intensity transfer from Bragg peaks into diffuse intensity between the Bragg peaks, covered by the one- and multi-phonon contributions in the model. The transmitted beam is considered to be constant for every pump probe delay Δt and thus can be subtracted by using intensity difference maps, which only represent the changes in the Bragg peaks and diffuse intensity.

Based on these considerations, we employed intensity differences in the fitting approach, giving the following fit equation:

$$\Delta I_{model}(\vec{q}, \Delta T) = \lambda \cdot \Delta I_{exp}(\vec{q}, \Delta t = 20 \text{ ps}), \quad (84)$$

with the scaling factor λ . The problem of determining the transmitted beam tail is then shifted to determining the resulting temperature change ΔT in thermal equilibrium. If the pump parameters and heat capacity are known, ΔT can be estimated, as presented in Sec. 7.3. The one-phonon distribution is then calculated at the initial temperatures and elevated temperature to simulate the difference.

In this work, the OPCs were calculated for five temperatures in the range given by the boundaries estimated in section 7.3. The limited coherence of electrons in the experiment was accounted by a smearing parameter as described in Sec. 5.4. A temperature change of $\Delta = 190 \text{ K}$ ($T_2 = 490 \text{ K}$) gave the best match between model and experiment and was used for all calculations presented below. The final temperature is at the lower boundary, indicating either a model mismatch or that the true elevated temperature is below the estimated range. Furthermore the matching process leaves space for improvement. A more general procedure could be an algorithm that calculates a best match by tuning the smearing parameter and temperature in an iterative scheme. This procedure needs many simulated difference maps to converge, hence substantial computing power.

The resulting experimental and simulated intensity difference maps are shown in Fig. 36. With the subtracted tail of the transmitted beam, a clear qualitative match of model and experiment is visible. Most characteristic features in the simulated OPC are now visible in the experimental difference map.

The resulting scaling parameter is displayed in the inset of figure 37. Tests with different selections of BZs did not give significant differences in the scaling parameter. A good stability of the fit is also indicated by its standard deviation of only 0.44 % of λ . The coefficient of determination $R^2 = 0.67$ indicates a good, but not perfect agreement of model and experimental intensity differences. Deviations of the model from the experimental values in \vec{q} -space are analyzed by looking at the residuals relative to their experimental values:

$$R_{rel}(\vec{q}, \Delta T, \Delta t_{eq}, \lambda) = \frac{r(\vec{q}, \Delta T, \Delta t_{eq}, \lambda)}{\lambda \cdot \Delta I_{exp}(\vec{q}, \Delta t_{eq})} \quad (85)$$

with residuals simply given by:

$$r(\vec{q}, \Delta T, \Delta t_{eq}, \lambda) = \Delta I_{model}(\vec{q}, \Delta T) - \lambda \cdot \Delta I_{exp}(\vec{q}, \Delta t_{eq}). \quad (86)$$

The temperature difference of the calculated intensity difference maps is $\Delta T = 190 \text{ K}$ and the equilibrium pump-probe delay $\Delta t_{eq} = 20 \text{ ps}$, based on the results from section 8. The resulting $R_{rel}(\vec{q}, \Delta T, \lambda)$ are shown in figure 37.

Discrepancies between the model and experimental intensity differences could arise from three effects. First, there could be deviations of the calculated phonon properties compared to the phonons probed by the experiment. Such deviations are expected to mainly affect the shape of the OPSF features. Second, there could be deviations

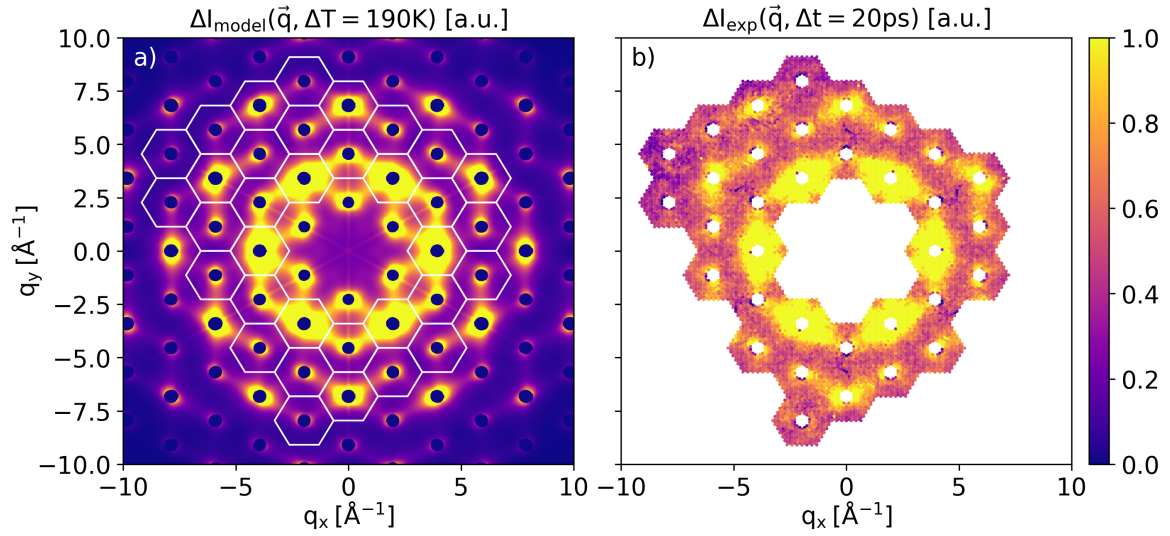
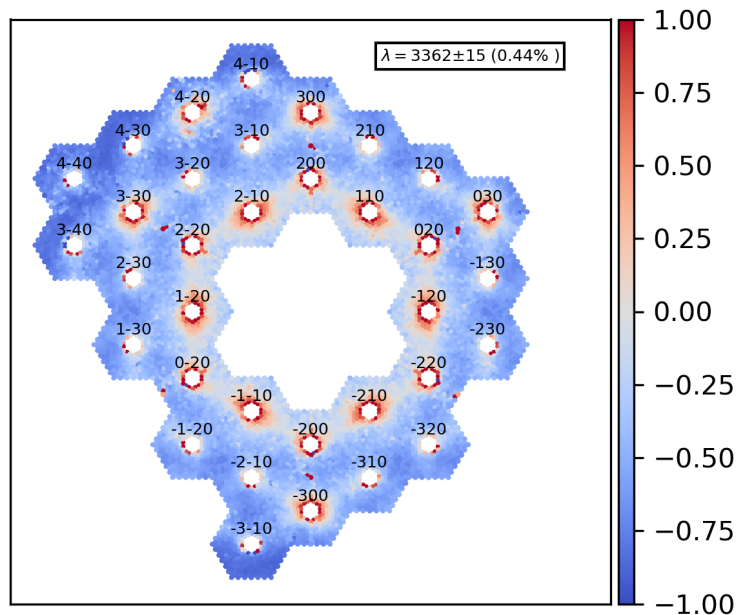


Figure 36: Comparison between model and experimental intensity changes $\Delta I(\vec{q}, T)$ in thermal equilibrium. Both images are plotted with the same color scale. a) Calculated intensity change of the zero-phonon and one-phonon contributions $\Delta I_{\text{model}}(\vec{q}, \Delta T) = \Delta I_0(\vec{q}, \Delta T) + \Delta I_1(\vec{q}, \Delta T)$ for a temperature change of $\Delta T = 190\text{K}$. White hexagons indicate 1 BZs accessible by the experiment. Only positive changes are covered by the colormap. Bragg peaks in the center have a negative change. Sixfold symmetric features of the one-phonon contribution also appear in the changes. b) Adjusted intensity change $\lambda \cdot \Delta I_{\text{exp}}(\vec{q}, \Delta t = 20\text{ps})$ at thermal equilibrium with cut Bragg peaks.

Figure 37: Relative residual map $R_{\text{rel}}(\vec{q}, \Delta T, \Delta t_{\text{eq}}, \lambda)$ for $\Delta T = 190\text{K}$ and $\Delta t_{\text{eq}} = 20\text{ps}$. Scaling parameter λ is shown in the inset. Positive or negative residuals are indicated by blue and red dots. Miller indices of Bragg peaks are given above the cut Brillouin zone centers.



in the expected temperature change ΔT . This would mainly affect the magnitude of the OPSF features in $\Delta I_{\text{model}}(\vec{q}, \Delta T)$. A third source of discrepancies is attributed to effects that are neglected in the calculations, such as multi-phonon scattering, defects, inelastic plasmon and secondary scattering [28, 91], as well as 0th order beam dynamics and dynamical laser noise.

As can be seen in Fig. 37, positive $R_{\text{rel}}(\vec{q}, \lambda)$ -values are mainly located at characteristic OPC features with higher intensity near the Bragg peaks, resulting in a light OPSF feature shape of positive values in $R_{\text{rel}}(\vec{q}, \lambda)$ (compared with Fig. 36). These areas indicate an overestimation of the modeled intensity difference (shown as red features in figure 37). Since the OPSF-shape agrees very well with the observed shape in the experiment, we can exclude strong deviations of calculated phonon properties from their experimental values. A more plausible source of overestimation in the observed red areas on Fig. 37 might be a slightly mismatched temperature change ΔT . With $\Delta I_{\text{mod}}(\vec{q}, \Delta T) = I_{\text{mod}}(\vec{q}, T_2) - I_{\text{mod}}(\vec{q}, T_1)$, an overestimated T_2 would result in higher phonon populations of $I_{\text{mod}}(\vec{q}, T_2)$, increasing $I_{\text{mod}}(\vec{q}, \Delta T)$. Owing to the product of phonon populations and OPSF (see Eq. 32), especially intense features of the OPSF would be increased most. In the next subsection we evaluate to what extent the discrepancies could result from multi-phonon scattering.

10.4.1 Multi-phonon scattering effects

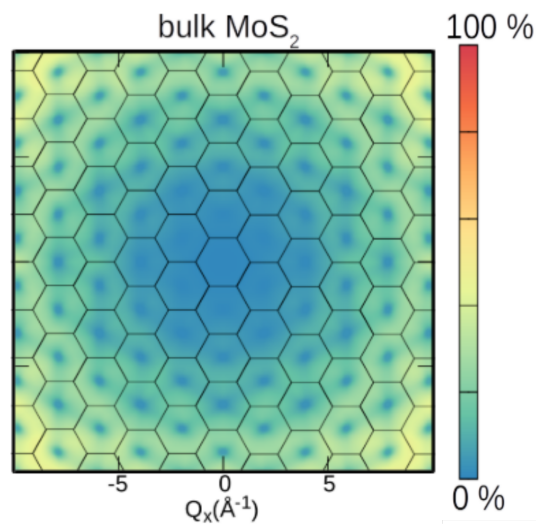
Blue areas on Fig. 37 indicate negative residuals, where the calculated intensity differences are underestimated. These areas appear as diffuse background between the Bragg peaks, showing no characteristic shape. The magnitude of deviations increases with increasing distance to the zero order. Based on the results of a recent study [28], such deviations can arise from multi-phonon scattering. In this study, the percentage contribution of multi-phonon interactions to diffuse scattering was calculated, given by:

$$P(\vec{q}, T) = \frac{I_{\text{multi}}(\vec{q}, T)}{I_1(\vec{q}, T) + I_{\text{multi}}(\vec{q}, T)}, \quad (87)$$

with I_1 being the one-phonon contribution (OPC) and I_{multi} the contribution of multi-phonon interactions. The calculated P for bulk MoS₂ at $T = 300$ K is shown in figure 38. The most remarkable feature of the multi-phonon contribution is its increase with increasing distance to the zero order, whereas zero- and one-phonon contribution show a decreasing behaviour. Areas accessible by the experiment show values from $\sim 5\%$ to 40 %, indicating that multi-phonon scattering is non-negligible for most accessible BZs.

In conclusion, the true contribution of most effects to the diffuse background in intensity differences remains unknown. We observe a good agreement of intense features of the intensity difference patterns, and the remaining deviations are attributed to a mismatch of equilibrium temperatures. Based on the good phenomenological agreement with calculated multi-phonon contributions, it is assumed that multi-phonon contributions dominate the diffuse residuals observed in the experiment. Since diffuse noise mostly affects areas with low one-phonon contributions, it is recommended to extract inelastic data in areas with high OPC signal. The extraction of inelastic data,

Figure 38: Calculated percentage contribution $P(\vec{q}, T)$ of multi-phonon interactions to diffuse scattering of bulk MoS_2 at $T = 300$ K. Graphic used from [28].



as described in section 9.2, rigorously averages over all points inside the BZ, to obtain a almost full BZ view on inelastic data. Such averaging step is only possible because intense OPC features are 1-2 magnitudes larger than the diffuse background.

Additionally multi-phonon scattering sets an upper boundary to the BZs that could be analyzed, since BZs with high scattering vectors \vec{q} do show significantly large multi-phonon contributions. The inner boundary is set by the tail of the zero order beam, restricting BZs with best SNR to an area of 2-3 BZs far away from the zero order BZ. The findings of our study together with the results of Ref. [28] point to the necessity of including multi-phonon contribution calculations even in the qualitative interpretation of inelastic scattering data. A comparison to other diffuse FED studies [17, 18, 20, 21, 92] shows that multi-phonon scattering effects have been more or less neglected.

10.5 Results

The equation system (Eq. 38) is solved with the intensity differences scaled to calculated OPC maps with a temperature change of 190 K, as determined from the previous section (Sec. 10.4). In order to reduce multicollinearity, the phonon system has been binned into four effective branches, described in section 10.2. For solving the equation system, the implementation of the NNLS algorithm as included in the *scipy*-package [37] has been used, to ensure that phonon population changes are positive. The retrieved phonon population changes are directly converted into an effective temperature by inverting the Bose-Einstein statistics and using the initial phonon population at 300 K (Sec. 6.1). Describing the out-of-equilibrium dynamics of the phonon system with BE statistics, only defined at thermal equilibrium, is a widely used approach [52]. Considering temperatures is equivalent to phonon populations, but is better suited since temperatures should become constant in thermal equilibrium within the BZ, whereas populations show variations. The effective branch-resolved out-of-equilibrium dynamics throughout all available parts of the BZ are shown in Fig. 39.

Our analysis of the out-of-equilibrium dynamics focuses on the first few picoseconds due to the following reasons: i) Multicollinearity is reduced in the early out-of-equilibrium dynamics, since only strongly coupled branches are contributing to the

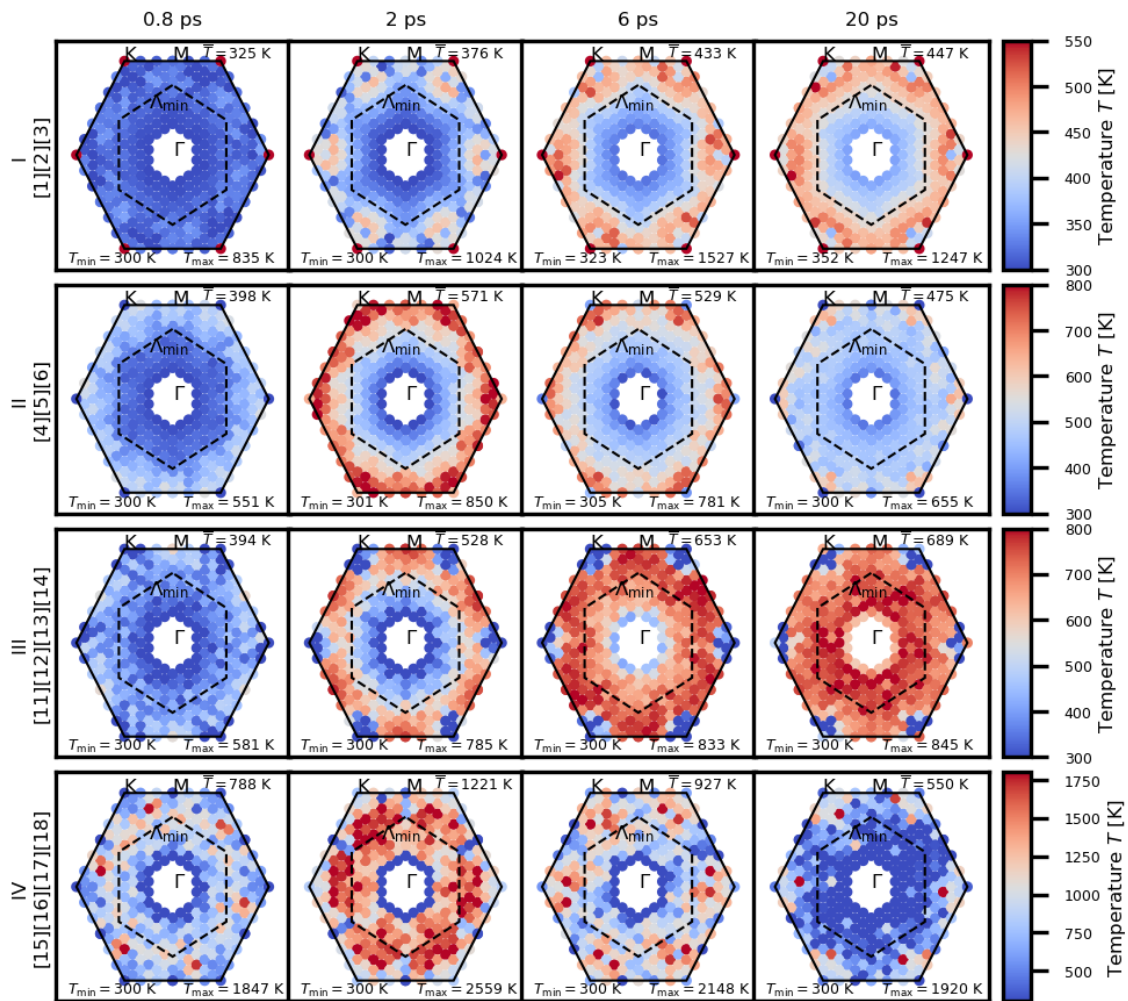


Figure 39: Temperature evolution of effective phonon branches within the first BZ. Binned branch indices are given on the left. Average, minimum and maximum temperature of every snapshot are given in the inset. The dashed line indicates the first (outer) and second (inner) zone as used in Sec. 9.2. Colour codes are different for every effective branch to gain a more detailed perspective.

diffuse signal. Thus signals of individual branch contributions can be better distinguished, in contrast to the equilibrium state where all active branches generate diffuse scattering signals. ii) The constant OPSF approximation, that uses the OPSF at the initial temperature of the measurement ($T_1 = 300$ K) for all pump-probe delays, is more valid if the lattice temperature is closer to the initial temperature.

Before starting the discussion of branch-resolved results, we have to keep in mind two things. First, a small region around K showed the highest multicollinearity with the peak at the direct K point (see Sec. 10.2). The diffuse scattering signals around K generated by the branches cannot be distinguished well. As a consequence, solutions show a strong shift of population changes to one branch, mainly indicated by singularities in phonon temperatures. Second, high energy branch temperatures are more sensitive to deviations due to their logarithmic dependence on phonon population changes. Thus, the strength of temperature changes is expected to show more deviations for the two effective high energy branches than for the effective low energy branches.

The interpretation of the fundamental processes observed is analogous to those in the elastic (Sec. 8) and inelastic analyses (Sec. 9.2). The areas around Γ are excluded due to the strong overlap with Bragg peak intensities. Hot electrons relax back to the Fermi level through the emission of phonons (electron-phonon coupling), leading to an increase in phonon populations and thus an increase of effective lattice temperature. As the first out-of-equilibrium phonon populations are generated, phonon relaxation starts in parallel restoring the BE-distribution via phonon-phonon scattering (phonon-phonon coupling). EPC is expected to be the dominating process generating phonons in the first few picoseconds. PPC is expected to generate phonons on longer timescales up to 20 ps, until the lattice reaches an elevated thermal equilibrium at an elevated temperature.

For the sake of clarity, we discuss the temperature evolution of each effective branch separately.

(I): We start with the first effective branch, consisting of all three acoustic branches. The hotspots at the K-point, visible in all snapshots, are attributed to multicollinearity. In comparison to other branches, it appears that the least squares solver shifted the K-phonon populations of the other effective branches to the first effective branch. In the following discussion, the K-point is interpreted as if it would have the temperature of its surrounding areas.

The overall dynamics of the first effective branch can be described as continuously rising with pump-probe delay, as indicated by the average temperatures. Most areas reached their maximum temperature at 20 ps and do not show a strong overshooting as expected for strong EPC. Thus temperature changes of this effective branch are mainly attributed to PPC. This interpretation is also underpinned by the relatively even heating of the first and second zones in the BZ. As non-equilibrium phonon scattering to acoustic branches is less restricted by energy and momentum conservation rules, they have more free phase space, resulting in an even distribution of phonons in \vec{k} -space. The first zone shows a good agreement with the expected temperature change of 490 K. The strongest deviations are observed in the highly multicollinear areas around K. The second zone around Γ underestimates the temperature changes by up to 100 K, as a possible result of an overlap of diffuse intensity with Bragg peak tails.

In conclusion, the phonon dynamics of the first effective branch indicates that the

phonon dynamics of the three acoustic branches are driven by PPC in the available parts of the BZ. Strong heating of very localized areas, as expected for strong EPC, was not observed. The continuously rising temperatures are in a good agreement with recent *ab initio* studies of the lattice dynamics of monolayer MoS₂ [52].

(II): The second effective branch, consisting of the three lowest optical branches, shows a strong rise of temperatures in the first outer zone within the first 2 ps. The maximum temperatures at the K-M line reach 850 K, far above the elevated equilibrium temperature. Strongest coupling is retrieved around K and a slightly weaker coupling around M. Those areas are much larger than those affected by multicollinearity, indicating that the temperatures arise from the diffuse signal. The rise is followed by a decay of temperatures in the first zone, reaching ≈ 500 K at 20 ps. The strong rise of temperatures in the first outer zone indicates strong EPC, followed by a thermalization through PPC for larger pump-probe delays. The EPC is strongest at the K-M line and gets weaker for areas closer to Γ . The temperature within the second inner zone shows a continuously rising evolution, reaching its maximum at 20 ps. The temperatures obtained in both zones at 20 ps show rather constant values around 480 K, indicating that a new thermal equilibrium is reached. The largest deviations are found at the highly multicollinear areas around K.

As the second effective branch consists of the lowest energy optical branches, it is quite interesting that such low-energy branches couple strongly to the electrons. A coupling to the high energy optical branches is more efficient and likely, since these phonons carry more energy. [12, 93, 94]. Due to the binning, it is not possible to distinguish which of the branches (4,5, or 6) contributes most. A comparison to the phonon dynamics obtained by first-principle calculations for monolayer MoS₂ [52] shows a good agreement with our results. The strong coupling of the two highest energy branches (5 and 6) in the low energy phonon band at K-M could explain the signals in the experiments. Both branches 5 and 6 are degenerated. The results of the elastic scattering analysis (Sec. 8) predicted a strongly coupled low-energy branch, due to the larger amplitude of the EPC signal (fast process) compared to the PPC signal (slow process). A possible explanation of that effect could be found in the large occupation of branches 5 and 6 in the non-equilibrium state of the lattice, since elastic scattering signal amplitudes depend on the phonon frequencies via $\frac{1}{w}$. In comparison, first principle calculations [52] predicted large non-equilibrium occupations around K, M and Γ for monolayers in the same branches, that would have a similar effect on elastic signals.

(III): We continue the analysis with the third effective branch, consisting of the four middle branches of the high energy phonon band. Branches 7-10 are excluded due to the inactivity of their OPC in the plane probed by the experiment, as seen in Fig. 8. The first outer zone exhibits an unusual behaviour in its temperature evolution. Within the first 2 ps, rising temperatures around M are observed, indicating strong EPC in those areas. Instead of a subsequent decay, however, temperatures continue to rise, covering most of the first zone except K, before they decay at 20 ps. Areas around K remain almost at the initial temperature for all snapshots. These extreme values are attributed to multicollinearity, as the shape of highly multicollinear areas are identical to those at K (Fig. 32).

The temperatures of the second zone continuously rise, until they reach their highest values at 20 ps. Temperatures of both zones are quite constant, but do not match the expected elevated temperature. With ≈ 700 K they are also clearly higher than the other effective branches.

A clear and consistent description of the phonon dynamics of the third effective branch failed. The results also show no agreement with the previous theory study on monolayer MoS₂ [52]. There are two possible effects causing strong temperature deviations. Temperatures of high energy branches are much more sensitive to deviations of phonon populations. Thus, shifts of phonon populations induced by multicollinearity can result in larger temperature shifts. The first two effective branches are slightly underestimating the temperature changes. It is possible that the populations of these branches have been shifted to the high energy branches. Multi-phonon scattering (see Sec. 10.4.1) results in an additional increase of diffuse scattering intensity with no specific shape, in contrast to the OPCs. In a good approximation multi-phonon scattering generates a diffuse background covering all parts of the BZ. It is possible that the additional intensity changes generated by multi-phonon scattering are attributed to the branches which match their pattern best. As a result, these branches would be hotter in equilibrium than the rest.

(IV): The last effective branch, consisting of the four highest energy branches, shows the highest temperatures observed in the system. Effects of multicollinearity, sensitivity and multi-phonon scattering are expected to have a large impact on the absolute temperatures. The overall dynamics observed are consistent with the elastic timetraces (Fig. 24) and dynamics observed for the effective branches I and II. The first and second zones both exhibit a rise of temperatures within the first few picoseconds, followed by a decay, reaching their lowest values at 20 ps.

The rise of temperatures at 2 ps indicates a strong coupling in most parts of the available BZ, reaching values up to 2500 K. A weaker EPC at the BZ edges compared to other regions is indicated by the few hundred degrees colder temperatures. It is obvious that the shape of colder temperatures is equivalent to the strongly-coupled areas in the second effective branch. This is very likely the result of multicollinearity between the branches. The lines at the M- Γ line are a result of double counting in the DFT calculations, due to rotational averaging, and only play a role in areas with low sensitivity.

The retrieved temperatures at 20 ps underpin the instability of the results. Regions at K show temperatures of ≈ 1000 K, whereas all other regions show 300 K, indicating no changes. These areas are equivalent to areas with very low sensitivity (Sec. 10.3). As such high temperatures cannot be explained by population shifts due to multicollinearity, they are tentatively attributed to multi-phonon effects covered by the branch. A quick comparison of phonon populations around K shows, that the population changes of the low energy branches would only result in ≈ 250 K temperature changes in the high energy branches, if all their population was transferred to them.

In conclusion, the phonon population dynamics of the four effective branches have been extracted using the branch-resolved approach first described in Ref. [20]. The phonon population dynamics were analyzed in the equivalent picture of effective tem-

peratures within a wide range of the BZ. The dynamics extracted for the effective low energy branches I and II showed consistent results with our own analysis and a good agreement of EPC and PPC with recent studies [52]. The results for the effective high energy branches III and IV exhibit overestimated temperatures and partially inconsistent dynamics. The observed deviations are mainly attributed to multi-phonon scattering, neglected here, as well as to the low sensitivity of our measurement to high energy phonon branches.

10.6 Residuals

The residuals $\Delta I - F \cdot \Delta n$ obtained by the non-negative least square optimization are used as the main parameters to determine the accuracy of the solution $\Delta n_j(\vec{k}, t)$. From solving the equation system (Eq. 38) we obtain residuals for every scattering vector \vec{q} , branch j and pump probe delay Δt . A more condensed view on the residuals is achieved by averaging over branches and pump-probe delays, which is shown in figure 40.

The total mean magnitude of residuals is -3×10^{-11} indicating a good match between the model and data. The maximum value of -5×10^{-9} is located in the hot spot visible in all BZs, which are closest to the transmitted electron beam. The averaged mean residual is 0.02 % of the resulting population changes, indicating a high accuracy of the NNLS algorithm. Deviation in the physics are thus accounted to the equation system itself and not to the solving procedure. Most deviations between the model and experimental data are visible in BZs close or very distant from the transmitted beam. Lines visible in the BZ are accounted to an overlap in the OPC calculations by the theoretician.

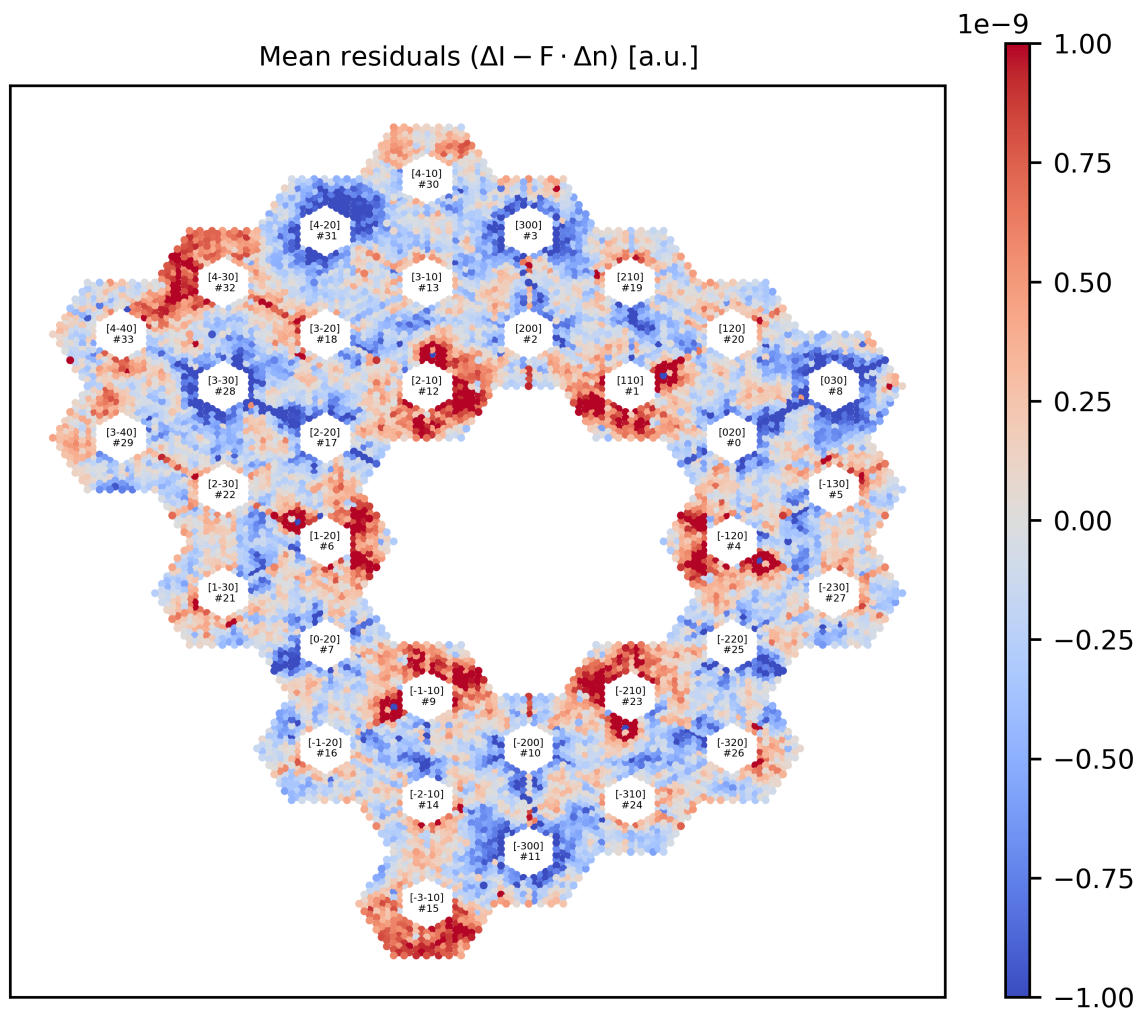


Figure 40: Delays and branch averaged residuals $\Delta I - F \cdot \Delta n$ of every Brillouin zone accessible by the experiment. Miller indices of the corresponding Bragg peaks and BZ indices are shown in the excluded center of every BZ.

11 Conclusion

In this thesis we investigated the structural dynamics of bulk MoS₂ after photoexcitation with momentum and partial branch resolution by combining femtosecond electron diffraction (FED) with first principle calculations.

As a first step, we implemented a streamlined analysis for the elastic and diffuse scattering data of FED experiments. Elastic scattering signals provide the momentum integrated transient phonon dynamics after photoexcitation via the Debye-Waller effect, whereas diffuse scattering signals provide a momentum-resolved view of the transient phonon dynamics within the first Brillouin zone. The elastic and comparably delicate diffuse scattering signals of MoS₂ were successfully extracted by applying various corrections and averaging steps. As a central correction step, we applied a distortion correction on the diffraction patterns to account for the strong distortions as they occur in FED experiments, compared to those of standard TEMs. The correction allows an exact extraction of elastic and diffuse scattering signals in reciprocal space.

As a second step, we implemented an approach first presented in Ref. [20] that combines ab-initio calculations with femtosecond electron diffuse scattering signals to achieve branch resolution in addition to time and momentum resolution. For this, experimental and simulated diffuse diffraction patterns were combined in an equation system. By testing the approach on graphene and MoS₂, we found that multicollinearity of the equation system and multi-phonon scattering are major factors which limit the quality and trustworthiness of results. We showed that by binning the phonon branches into 4 effective branches of similar energies, i.e. by simplifying the physical model, multicollinearity could be significantly reduced. With the binned branches, the results of MoS₂ showed a good agreement between the two low-energy branch dynamics and a recent ab initio study, but inconsistencies remained for the two high-energy branches. We tentatively attribute these inconsistencies to the low sensitivity of the experiment to the high-energy branches.

Multicollinearity of the equation system is less important if only a few branches exhibit strong inelastic signals. This is typically the case in highly non-equilibrium conditions and, for certain materials, this can be achieved by carefully choosing the pumping conditions. For instance, in the case of MoS₂, the possible electron-phonon scattering pathways could be reduced by setting the excitation wavelength right above the indirect or direct band gap transitions. Therefore, the approach of Ref. [20] could be well suited for describing the non-equilibrium states of a material with carefully selected excitation conditions. Nevertheless, our findings indicate that a complete branch-resolution (energy) over the entire structural dynamics timescales and for similar or more complex materials than MoS₂ remains elusive. In the future, it could be interesting to explore machine-learning approaches to retrieve branch-resolution. However, it is likely that algorithms based on the recognition of OPC patterns might similarly struggle to distinguish contributions from branches featuring similar OPC signatures.

Beyond its methodological developments, this thesis also provided physical insights into the lattice dynamics of MoS₂. We extracted the elastic scattering signals at non-equilibrium and equilibrium timescales. In particular, the experiments have revealed the non-thermal character of the lattice following photo-excitation. We found that the lattice dynamics can be described by a fast time constant of ~ 0.5 ps, attributed to

electron-phonon coupling (EPC), and a slow time constant of ~ 3 ps, attributed to phonon-phonon coupling (PPC). Interestingly, the comparison of the EPC and PPC signals indicates a strong EPC to low-frequency modes. We attribute this to the shape of the electronic band structure of MoS₂ (Fig. 5). Each populated valley provides many decay paths for intravalley transitions in the conduction and valence bands. Such transitions generate low-wavevector phonons around Γ , as shown in Fig. 41 for the case of monolayer MoS₂. Moreover, we could partially confirm the results of the recent first principle calculations presented in Ref. [52], which predicted a strong coupling to all modes around Γ (see Fig. 42) with similar excitation conditions.

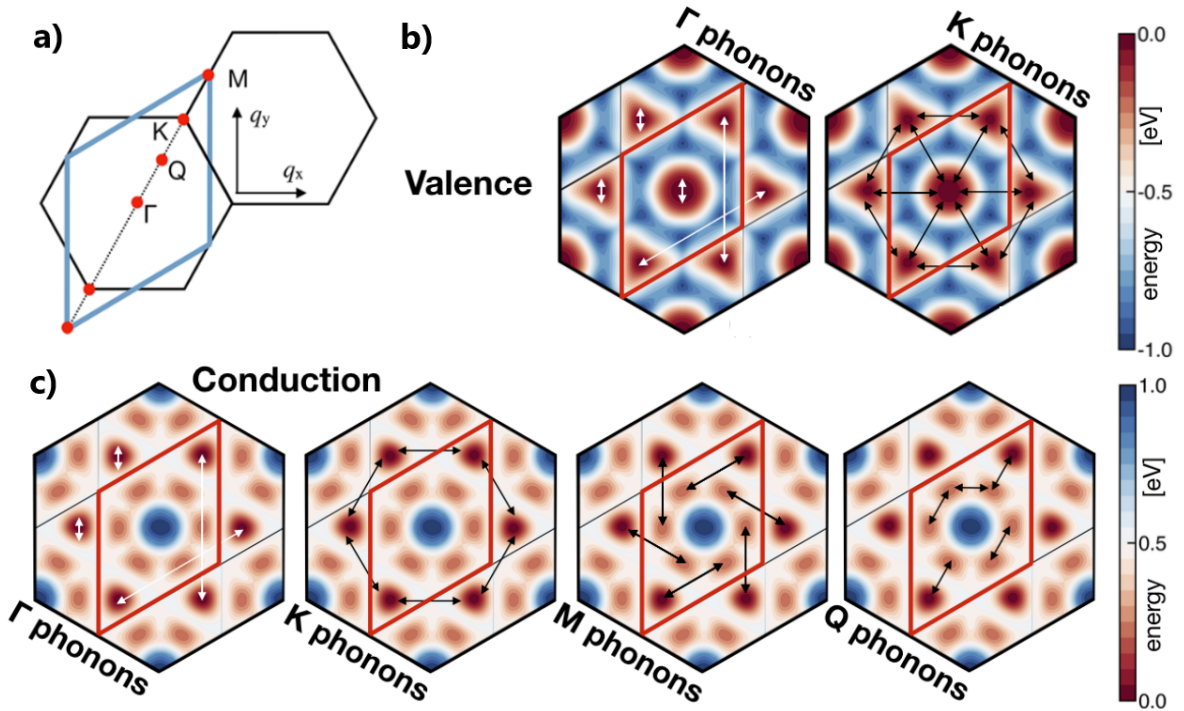


Figure 41: a) Brillouin zone of monolayer MoS₂ with high-symmetry points labeled. b) and c) Illustration of phonon- assisted electronic transitions (marked by arrows) in the valence and conduction bands, after excitation of the Q- and K-valley of monolayer MoS₂. The color coding indicates the valence and conduction band energies. Figure reproduced from Ref. [52].

Our analysis of the diffuse scattering signals within the available parts of the BZ revealed a momentum-resolved view on the phonon dynamics in MoS₂. We observed strong EPC around the BZ edges given by an area within the K/2-K-M-M/2 line, as qualitatively indicated by the shaded areas in Fig. 42 (b). The phonons generated in this area arise from intervalley transitions within the valence and conduction bands. Such processes emit phonons within a large variety of wavevectors (e.g. K-, M- and Q-phonons) as illustrated in Figure 41. The free decay paths for these transitions are further enhanced due to the degenerated valleys introduced by the six-fold symmetry of MoS₂. The generation of smaller wavevector phonons (e.g. K/2-phonons) is attributed to our excitation conditions, which enable broadband intervalley transitions between the valley (hill) slopes in the conduction band (valence band). These results are also in very good agreement with the recent first principle study (Ref. [52], Fig. 42 a)) and

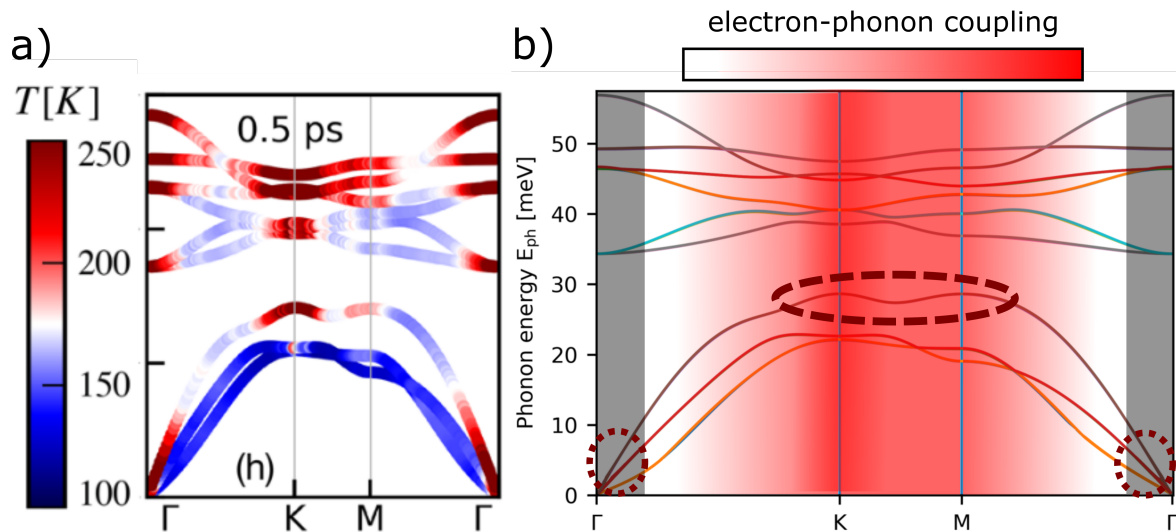


Figure 42: a) Transient effective phonon temperatures along the Γ -K-M- Γ line for monolayer MoS₂, 0.5 ps after photoexcitation, obtained by first principle calculations. b) Illustration of the momentum-resolved view on the EPC strength. Shaded red areas qualitatively (color scales and dimensions are not matched with the data) indicate EPC strength from the inelastic analysis. Black areas mark inaccessible parts. Dotted and dashed ovals indicate the strong EPC areas obtained by the elastic and branch-resolved inelastic analysis, respectively. Fig. a) used from Ref. [52].

underpin the capabilities of FEDS to determine momentum-dependent signals which reflect the EPC and PPC across the BZ. On the outlook, it would be interesting to compare first principle calculations and experiments with similar excitation conditions, to achieve a similar picture as shown in figure 41.

Finally, we applied the branch-resolved approach on bulk MoS₂ to achieve an additional energy- or branch-resolution of the phonon dynamics. We showed that due to the previously described reasons, the analysis is quite delicate and heavily depends on the material structure. For MoS₂ we extracted consistent results for the low-energy branches of the phonon system described by two effective branches. On the outlook, we could extend the analysis to explicitly retrieve the coupling constants by using the non-thermal lattice model [12]. The results suggest dominating PPC in the three acoustic branches and strong EPC signals around the BZ zone edges (indicated by the dashed oval in Fig. 42). These findings also partially confirm the results of the recent first-principle calculations in Ref. [52], showing that DFPT can be used together with FEDS to gain a more detailed view on EPC and PPC.

References

1. Eliashberg, G. M. Interactions between electrons and lattice vibrations in a superconductor. *Sov. Phys.–JETP* **11**, **11** (1960).
2. Hur, N. *et al.* Electric polarization reversal and memory in a multiferroic material induced by magnetic fields. *Nature* **429**, 392–395. ISSN: 00280836 (2004).
3. Zhao, L. D. *et al.* Ultrahigh power factor and thermoelectric performance in hole-doped single-crystal SnSe. *Science* **351**, 141–144. ISSN: 10959203 (2016).
4. Novko, D. & Kralj, M. Phonon-assisted processes in the ultraviolet-transient optical response of graphene. *npj 2D Materials and Applications* **3**. ISSN: 23977132. arXiv: 1911.04826. <http://dx.doi.org/10.1038/s41699-019-0131-5> (2019).
5. Saidi, W. A. & Kachmar, A. Effects of Electron-Phonon Coupling on Electronic Properties of Methylammonium Lead Iodide Perovskites. *Journal of Physical Chemistry Letters* **9**, 7090–7097. ISSN: 19487185 (2018).
6. Gibbons, T. M., Bebek, M. B., Kang, B., Stanley, C. M. & Estreicher, S. K. Phonon-phonon interactions: First principles theory. *Journal of Applied Physics* **118**. ISSN: 10897550. <http://dx.doi.org/10.1063/1.4929452> (2015).
7. Waldecker, L., Bertoni, R. & Ernstorfer, R. Compact femtosecond electron diffractometer with 100 keV electron bunches approaching the single-electron pulse duration limit. *Journal of Applied Physics* **117**. ISSN: 10897550. arXiv: 1412.1942. <http://dx.doi.org/10.1063/1.4906786> (2015).
8. Dwyer, J. R. *et al.* Experimental basics for femtosecond electron diffraction studies. *Journal of Modern Optics* **54**, 923–942. ISSN: 09500340 (2007).
9. Sciaini, G. & Miller, R. J. Femtosecond electron diffraction: Heralding the era of atomically resolved dynamics. *Reports on Progress in Physics* **74**. ISSN: 00344885 (2011).
10. Gao, M. *et al.* Mapping molecular motions leading to charge delocalization with ultrabright electrons. *Nature* **496**, 343–346. ISSN: 00280836 (2013).
11. Siwick, B. J., Dwyer, J. R., Jordan, R. E. & Miller, R. J. An Atomic-Level View of Melting Using Femtosecond Electron Diffraction. *Science* **302**, 1382–1385. ISSN: 00368075 (2003).
12. Waldecker, L., Bertoni, R., Ernstorfer, R. & Vorberger, J. Electron-phonon coupling and energy flow in a simple metal beyond the two-temperature approximation. *Physical Review X* **6**, 1–11. ISSN: 21603308. arXiv: 1507.03743 (2016).
13. Tsen, K. T. & Ferry, D. K. Studies of electron-phonon and phonon-phonon interactions in InN using ultrafast Raman spectroscopy. *Journal of Physics Condensed Matter* **21**. ISSN: 09538984 (2009).
14. Yan, H. *et al.* Time-resolved Raman spectroscopy of optical phonons in graphite: Phonon anharmonic coupling and anomalous stiffening. *Physical Review B - Condensed Matter and Materials Physics* **80**, 1–4. ISSN: 10980121 (2009).

15. Trigo, M. *et al.* Imaging nonequilibrium atomic vibrations with x-ray diffuse scattering. *Physical Review B - Condensed Matter and Materials Physics* **82**, 1–5. ISSN: 10980121 (2010).
16. Trigo, M. Ultrafast Fourier transform inelastic x-ray scattering. *MRS Bulletin* **43**, 520–526. ISSN: 08837694 (2018).
17. Maldonado, P. *et al.* Tracking the ultrafast nonequilibrium energy flow between electronic and lattice degrees of freedom in crystalline nickel. *Physical Review B* **101**. ISSN: 24699969. arXiv: 1906.08504 (2020).
18. Stern, M. J. *et al.* Mapping momentum-dependent electron-phonon coupling and nonequilibrium phonon dynamics with ultrafast electron diffuse scattering. *Physical Review B* **97**, 1–6. ISSN: 24699969. arXiv: 1708.01251 (2018).
19. Seiler, H. *et al.* Accessing the Anisotropic Nonthermal Phonon Populations in Black Phosphorus. *Nano Letters* **21**, 6171–6178. ISSN: 1530-6984. arXiv: 2006.12873 (2021).
20. De Cotret, L. P. R. *et al.* Time- and momentum-resolved phonon spectroscopy with ultrafast electron diffuse scattering. **214115**. arXiv: 1908.02795. <http://arxiv.org/abs/1908.02795> (2019).
21. Waldecker, L. *et al.* Momentum-resolved view of electron-phonon coupling in multilayer WSe₂. *Physical Review Letters* **119**, 1–6. ISSN: 10797114. arXiv: 1703.03496 (2017).
22. Fultz, B. & Howe, J. M. *Transmission Electron Microscopy and Diffractometry of Materials* - ISBN: 978-3-642-29760-1 (Springer Science and Business Media, Berlin Heidelberg, 2012).
23. Gross, R., Marx, A., Einzel, D. & Geprägs, S. *Festkörperphysik - Aufgaben und Lösungen* ISBN: 978-3-110-56635-2 (Walter de Gruyter GmbH Co KG, Berlin, 2018).
24. Carter, C. B. & Williams, D. B. *Transmission Electron Microscopy - Diffraction, Imaging, and Spectrometry* ISBN: 978-3-319-79988-9 (Springer International Publishing, Cham, Heidelberg, New York, Dordrecht, London, 2018).
25. Peng, L.-M., Dudarev, S. L. & Whelan, M. J. *High Energy Electron Diffraction and Microscopy* - ISBN: 978-0-198-50074-2 (Oxford University Press, New York, 2004).
26. Zacharias, M., Giustino, F., Kelires, P. C. & Ernstorfer, R. Multi-phonon diffuse scattering in solids from first-principles: Application to layered crystals and 2D materials, 1–18. arXiv: arXiv:2103.10108.
27. Xu, R. & Chiang, T. C. Determination of phonon dispersion relations by X-ray thermal diffuse scattering. *Zeitschrift für Kristallographie* **220**, 1009–1016. ISSN: 00442968 (2005).
28. Zacharias, M. *et al.* Multi-phonon diffuse scattering in solids from first-principles: Application to 2D MoS₂, bulk MoS₂, and black Phosphorous Marios, 1–15. arXiv: 2103.10108. <http://arxiv.org/abs/2103.10108> (2021).

29. Mueller, K. *Bestimmung von Strukturparametern für Galliumarsenid mittels Elektronenbeugung* PhD thesis (Universität Bremen, 2007).
30. Sahoo, S., Gaur, A. P., Ahmadi, M., Guinel, M. J. & Katiyar, R. S. Temperature-dependent Raman studies and thermal conductivity of few-layer MoS₂. *Journal of Physical Chemistry C* **117**, 9042–9047. ISSN: 19327447 (2013).
31. Fan, J. H. *et al.* Resonance Raman scattering in bulk 2H-MX₂ (M = Mo, W; X = S, Se) and monolayer MoS₂. *Journal of Applied Physics* **115**. ISSN: 10897550 (2014).
32. Seiler, H. *et al.* Accessing the anisotropic non-equilibrium phonon populations in black phosphorus, 1–6 (2020).
33. Windsor, Y. W. *et al.* Exchange-Striction Driven Ultrafast Nonthermal Lattice Dynamics in NiO. *Physical Review Letters* **126**, 147202. ISSN: 1079-7114. <https://doi.org/10.1103/PhysRevLett.126.147202> (2021).
34. Sen, A. & Srivastava, M. *Regression Analysis - Theory, Methods, and Applications* ISBN: 978-1-461-24470-7 (Springer Science and Business Media, Berlin Heidelberg, 2012).
35. Blobel, V. & Lohrmann, E. *Statistische und numerische Methoden der Datenanalyse* (1998).
36. Schwarz, H. R. & Köckler, N. *Numerische Mathematik* ISBN: 9783834806833 (2009).
37. Lawson, C. L. & Hanson, R. J. *Solving Least Squares Problems* - ISBN: 978-0-898-71356-5 (SIAM, Philadelphia, 1995).
38. Sebastian, A., Pendurthi, R., Choudhury, T. H., Redwing, J. M. & Das, S. Benchmarking monolayer MoS₂ and WS₂ field-effect transistors. *Nature Communications* **12**, 1–12. ISSN: 20411723 (2021).
39. Koppens, F. H. *et al.* Photodetectors based on graphene, other two-dimensional materials and hybrid systems. *Nature Nanotechnology* **9**, 780–793. ISSN: 17483395 (2014).
40. Lopez-Sanchez, O., Lembke, D., Kayci, M., Radenovic, A. & Kis, A. Ultrasensitive photodetectors based on monolayer MoS₂. *Nature Nanotechnology* **8**, 497–501. ISSN: 17483395 (2013).
41. Mak, K. F., Lee, C., Hone, J., Shan, J. & Heinz, T. F. Atomically thin MoS₂: A new direct-gap semiconductor. *Physical Review Letters* **105**, 2–5. ISSN: 00319007. arXiv: 1004.0546 (2010).
42. Hein, P. *et al.* Mode-resolved reciprocal space mapping of electron-phonon interaction in the Weyl semimetal candidate Td-WTe₂. *Nature Communications* **11**. ISSN: 20411723. arXiv: 1911.12166. <http://dx.doi.org/10.1038/s41467-020-16076-0> (2020).
43. Pogna, E. A. *et al.* Photo-induced bandgap renormalization governs the ultrafast response of single-layer MoS₂. *ACS Nano* **10**, 1182–1188. ISSN: 1936086X (2016).

44. Song, I., Park, C. & Choi, H. C. Synthesis and properties of molybdenum disulfide: From bulk to atomic layers. *RSC Advances* **5**, 7495–7514. ISSN: 20462069 (2015).
45. Momma, K. & Izumi, F. VESTA 3 for three-dimensional visualization of crystal, volumetric and morphology data. *Journal of Applied Crystallography* **44**, 1272–1276. ISSN: 00218898 (2011).
46. Tornatzky, H., Gillen, R., Uchiyama, H. & Maultzsch, J. Phonon dispersion in MoS₂. *Physical Review B* **99**, 144309. ISSN: 24699969. <https://doi.org/10.1103/PhysRevB.99.144309> (2019).
47. Splendiani, A. *et al.* Emerging photoluminescence in monolayer MoS₂. *Nano Letters* **10**, 1271–1275. ISSN: 15306984 (2010).
48. Böker, T. *et al.* Band structure of (formula presented) (formula presented) and (formula presented) Angle-resolved photoelectron spectroscopy and ab initio calculations. *Physical Review B - Condensed Matter and Materials Physics* **64**, 1–11. ISSN: 1550235X (2001).
49. Frey, G. & Elani, S. Optical-absorption spectra of inorganic fullerene-like W). *Physical Review B - Condensed Matter and Materials Physics* **57**, 6666–6671. ISSN: 1550235X (1998).
50. Padilha, J. E., Peelaers, H., Janotti, A. & Van De Walle, C. G. Nature and evolution of the band-edge states in MoS₂: From monolayer to bulk. *Physical Review B - Condensed Matter and Materials Physics* **90**, 1–5. ISSN: 1550235X (2014).
51. Ellis, J. K., Lucero, M. J. & Scuseria, G. E. The indirect to direct band gap transition in multilayered MoS₂ as predicted by screened hybrid density functional theory. *Applied Physics Letters* **99**, 1–3. ISSN: 00036951 (2011).
52. Caruso, F. Nonequilibrium Lattice Dynamics in Monolayer MoS₂. *Journal of Physical Chemistry Letters*, 1734–1740. ISSN: 19487185. arXiv: 2102.05989 (2021).
53. Jin, W. *et al.* Direct measurement of the thickness-dependent electronic band structure of MoS₂ using angle-resolved photoemission spectroscopy. *Physical Review Letters* **111**, 1–5. ISSN: 00319007 (2013).
54. Giannozzi, P. *et al.* Advanced capabilities for materials modelling with QUANTUM ESPRESSO. *Journal of Physics: Condensed Matter* **29**. ISSN: 0953-8984 (Nov. 2017).
55. Hartwigsen, C., Goedecker, S. & Hutter, J. Hartwigsen-1998. *Physical Review B* **58**, 3641–3662 (1998).
56. Perdew, J. P., Burke, K. & Ernzerhof, M. Generalized gradient approximation made simple. *Physical Review Letters* **77**, 3865–3868. ISSN: 10797114 (1996).
57. Baroni, S., de Gironcoli, S., Corso, A. D. & Giannozzi, P. Phonons and related crystal properties from density-functional perturbation theory Stefano. *REVIEWS OF MODERN PHYSICS* **73** (2001).
58. Craney, T. A. & Surlis, J. G. Model-dependent variance inflation factor cutoff values. *Quality Engineering* **14**, 391–403. ISSN: 08982112 (2002).

59. Allen, P. B. Theory of thermal relaxation of electrons in metals. *Physical Review Letters* **59**, 1460–1463. ISSN: 00319007 (1987).
60. Ruan, C. Y. *et al.* Ultrafast diffraction and structural dynamics: The nature of complex molecules far from equilibrium. *Proceedings of the National Academy of Sciences of the United States of America* **98**, 7117–7122. ISSN: 00278424 (2001).
61. Zahn, D. *not published* PhD thesis (Fritz-Haber Institute, 2021).
62. Siwick, B. J., Dwyer, J. R., Jordan, R. E. & Miller, R. J. Ultrafast electron optics: Propagation dynamics of femtosecond electron packets. *Journal of Applied Physics* **92**, 1643–1648. ISSN: 00218979 (2002).
63. Castellanos-Gomez, A. *et al.* Deterministic transfer of two-dimensional materials by all-dry viscoelastic stamping. *2D Materials* **1**. ISSN: 20531583. arXiv: 1311.4829 (2014).
64. Zahid, F., Liu, L., Zhu, Y., Wang, J. & Guo, H. A generic tight-binding model for monolayer, bilayer and bulk MoS₂. *AIP Advances* **3**. ISSN: 21583226. arXiv: 1304.0074 (2013).
65. Kim, J. H. *et al.* Carrier multiplication in van der Waals layered transition metal dichalcogenides. *Nature Communications* **10**, 1–9. ISSN: 20411723. <http://dx.doi.org/10.1038/s41467-019-13325-9> (2019).
66. Harb, M. *et al.* Carrier relaxation and lattice heating dynamics in silicon revealed by femtosecond electron diffraction. *Journal of Physical Chemistry B* **110**, 25308–25313. ISSN: 15206106 (2006).
67. Windt, D. L. IMD—Software for modeling the optical properties of multilayer films. *Computers in Physics* **12**, 360. ISSN: 08941866 (1998).
68. Ermolaev, G. A. *et al.* Broadband optical properties of monolayer and bulk MoS₂. *npj 2D Materials and Applications* **4**, 1–6. ISSN: 23977132. <http://dx.doi.org/10.1038/s41699-020-0155-x> (2020).
69. Bano, A., Khare, P. & Gaur, N. K. Thermal transport properties of bulk and monolayer MoS₂: An ab-initio approach. *Journal of Physics: Conference Series* **836**. ISSN: 17426596 (2017).
70. Volovik, L. S. *et al.* Enthalpy and heat capacity of molybdenum disulfide. *Soviet Powder Metallurgy and Metal Ceramics* **17**, 697–702. ISSN: 15739066 (1978).
71. Peng, B. *et al.* Thermal conductivity of monolayer MoS₂, MoSe₂, and WS₂: Interplay of mass effect, interatomic bonding and anharmonicity. *RSC Advances* **6**, 5767–5773. ISSN: 20462069. arXiv: 1509.01391 (2016).
72. Mannebach, E. M. *et al.* Dynamic Structural Response and Deformations of Monolayer MoS₂ Visualized by Femtosecond Electron Diffraction. *Nano Letters* **15**, 6889–6895. ISSN: 15306992 (2015).
73. He, X., Chebl, M. & Yang, D. S. Cross-Examination of Ultrafast Structural, Interfacial, and Carrier Dynamics of Supported Monolayer MoS₂. *Nano Letters* **20**, 2026–2033. ISSN: 15306992 (2020).

74. Hall, S. R., Allen, F. H. & Brown, I. D. *The crystallographic information file (CIF): a new standard archive file for crystallography* **6**, 655–685. ISBN: 0606553150 (International Union of Crystallography, 1991).
75. René de Cotret, L. P., Otto, M. R., Stern, M. J. & Siwick, B. J. An open-source software ecosystem for the interactive exploration of ultrafast electron scattering data. *Advanced Structural and Chemical Imaging* **4**. ISSN: 21980926. <https://doi.org/10.1186/s40679-018-0060-y> (2018).
76. Capitani, G. C., Oleynikov, P., Hovmöller, S. & Mellini, M. A practical method to detect and correct for lens distortion in the TEM. *Ultramicroscopy* **106**, 66–74. ISSN: 03043991 (2006).
77. Pack, H., Monkhorst, J. & D., J. Special points for Brillouin-zone integrations. *Phys. Rev. B* **13** (1976).
78. Nie, Z. *et al.* Ultrafast carrier thermalization and cooling dynamics in few-layer MoS₂. *ACS Nano* **8**, 10931–10940. ISSN: 1936086X (2014).
79. Harb, M. *et al.* Phonon-phonon interactions in photoexcited graphite studied by ultrafast electron diffraction. *Physical Review B* **93**, 1–7. ISSN: 24699969 (2016).
80. Ligges, M. *et al.* Transient (000)-order attenuation effects in ultrafast transmission electron diffraction. *Journal of Applied Physics* **109**. ISSN: 00218979 (2011).
81. Wei, L. *et al.* Dynamic diffraction effects and coherent breathing oscillations in ultrafast electron diffraction in layered 1T-TaSeTe. *Structural Dynamics* **4**. ISSN: 23297778. <http://dx.doi.org/10.1063/1.4979643> (2017).
82. Karam, T. E., Hu, J. & Blake, G. A. Strongly Coupled Electron-Phonon Dynamics in Few-Layer TiSe₂ Exfoliates. *ACS Photonics* **5**, 1228–1234. ISSN: 23304022 (2018).
83. Chatelain, R. P., Morrison, V. R., Klarenaar, B. L. & Siwick, B. J. Coherent and incoherent electron-phonon coupling in graphite observed with radio-frequency compressed ultrafast electron diffraction. *Physical Review Letters* **113**, 1–5. ISSN: 10797114. arXiv: 1410.4784 (2014).
84. Nie, S., Wang, X., Park, H., Clinite, R. & Cao, J. Measurement of the electronic Grüneisen constant using femtosecond electron diffraction. *Physical Review Letters* **96**, 15–18. ISSN: 10797114 (2006).
85. Zhao, Y. *et al.* Interlayer breathing and shear modes in few-trilayer MoS₂ and WSe₂. *Nano Letters* **13**, 1007–1015. ISSN: 15306984 (2013).
86. Kuznetsov, A. V. & Stanton, C. J. Theory of coherent phonon oscillations in semiconductors. *Physical Review Letters* **73**, 3243–3246. ISSN: 00319007 (1994).
87. Sun, L. *et al.* Phonon Dephasing Dynamics in MoS₂. *Nano Letters* **21**, 1434–1439. ISSN: 15306992 (2021).
88. Ge, S. *et al.* Coherent longitudinal acoustic phonon approaching THz frequency in multilayer molybdenum disulphide. *Scientific Reports* **4**, 30–32. ISSN: 20452322 (2014).

89. Czycholl, G. *Theoretische Festkörperphysik Band 1 - Grundlagen: Phononen und Elektronen in Kristallen* ISBN: 978-3-662-47141-8 (Springer-Verlag, Berlin Heidelberg New York, 2015).
90. René de Cotret, L. P. & Siwick, B. J. A general method for baseline-removal in ultrafast electron powder diffraction data using the dual-tree complex wavelet transform. *Structural Dynamics* **4**. ISSN: 23297778. <http://dx.doi.org/10.1063/1.4972518> (2017).
91. Wang, Z.-l. *Elastic and Inelastic Scattering in Electron Diffraction and Imaging* - ISBN: 978-1-489-91579-5 (Springer Science and Business Media, Berlin Heidelberg, 2013).
92. Otto, M. R. *et al.* Mechanisms of electron-phonon coupling unraveled in momentum and time: The case of soft phonons in TiSe₂. *Science Advances* **7**, 1–9. ISSN: 23752548. arXiv: 1912.03559 (2021).
93. Maldonado, P., Carva, K., Flammer, M. & Oppeneer, P. M. Theory of out-of-equilibrium ultrafast relaxation dynamics in metals. *Physical Review B* **96**, 1–13. ISSN: 24699969. arXiv: 1708.01470 (2017).
94. Sadasivam, S., Chan, M. K. & Darancet, P. Theory of Thermal Relaxation of Electrons in Semiconductors. *Physical Review Letters* **119**, 1–6. ISSN: 10797114. arXiv: 1709.00451 (2017).

A Phonon branch polarization and energy of MoS₂

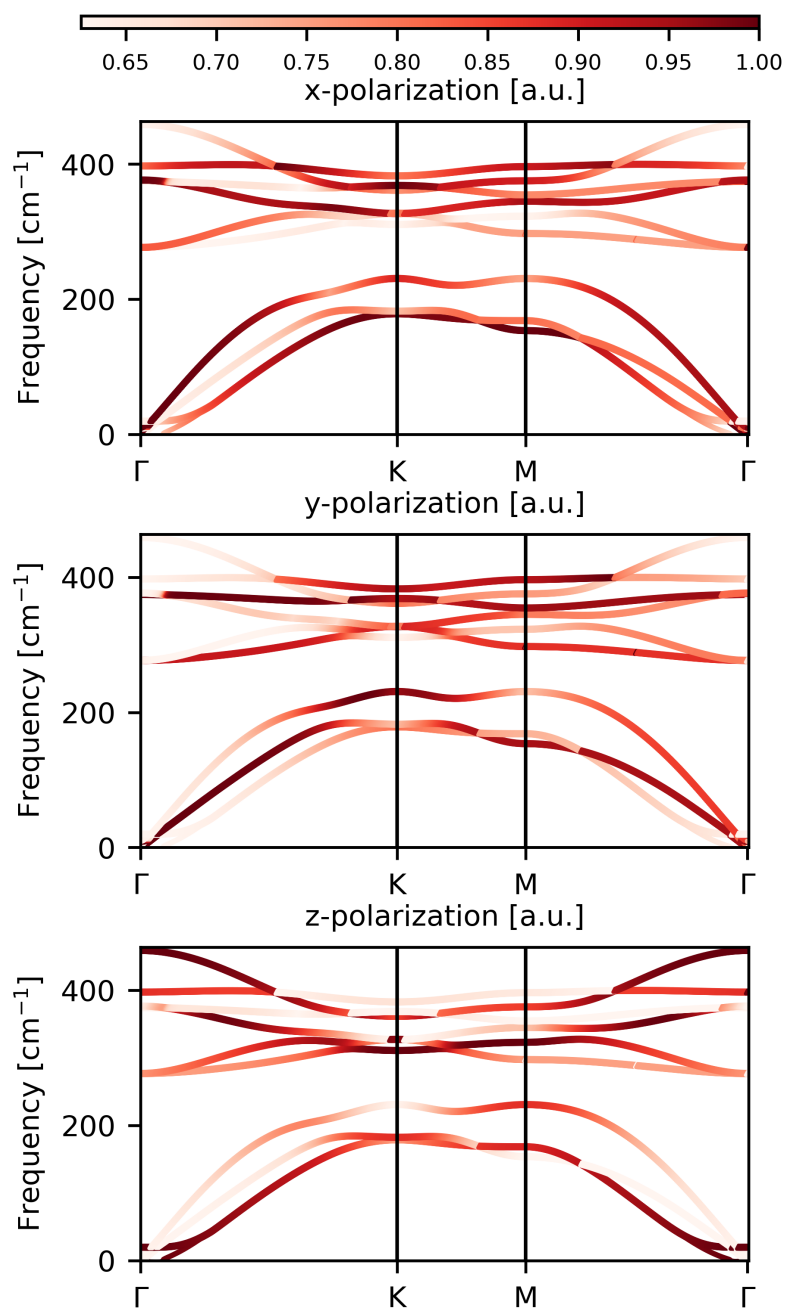


Figure 43: Mean polarization of all phonon branches of MoS₂ along the x,y and z-axis respectively.

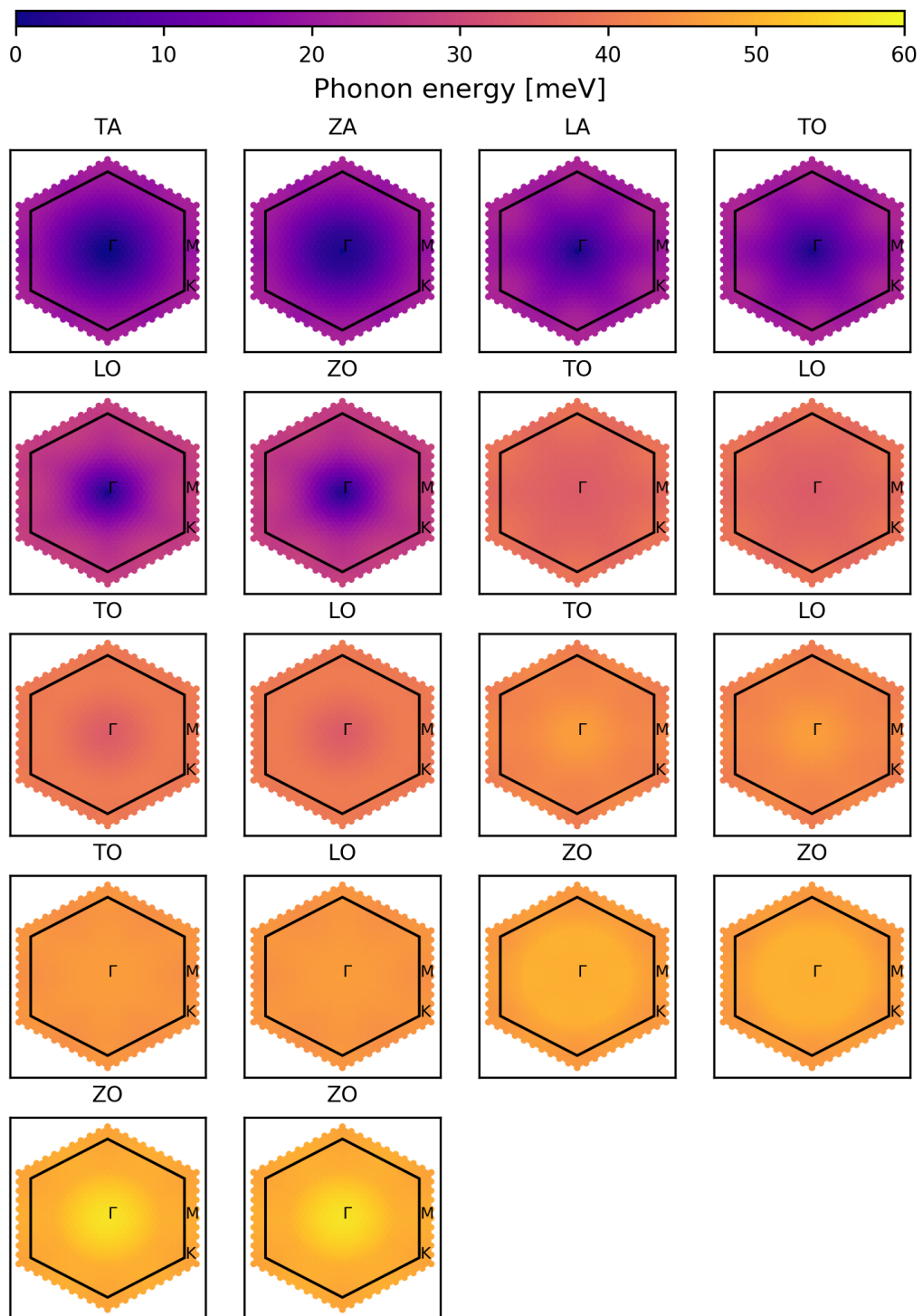


Figure 44: Phonon energies of MoS₂ of every branch in the first Brillouin zone.

B Results of the residual fit

[300]	[030]
Fit parameters:	Fit parameters:
$A = (0.042 \pm 0.006)$	$A = (0.066 \pm 0.006)$
$\mu = (9.3 \pm 0.6)$ ps	$\mu = (10.6 \pm 0.5)$ ps
$\sigma = (3.9 \pm 0.6)$ ps	$\sigma = (4.8 \pm 0.6)$ ps
$T = (8.4 \pm 0.5)$ ps	$T = (8.8 \pm 0.3)$ ps
$t_0 = (1.3 \pm 0)$ ps	$t_0 = (1.3 \pm 0)$ ps
$\phi = (0.8 \pm 0.5)$ ps	$\phi = (9.0 \pm 0.1)$ ps
$c = (0.0002 \pm 0.0002)$	$c = (0.0002 \pm 0.0002)$
$R^2 = 0.504$	$R^2 = 0.686$
[120]	[-240]
Fit parameters:	Fit parameters:
$A = (0.089 \pm 0.022)$	$A = (0.254 \pm 0.19)$
$\mu = (4.9 \pm 1.8)$ ps	$\mu = (3.7 \pm 9.7)$ ps
$\sigma = (6.8 \pm 1.7)$ ps	$\sigma = (16.8 \pm 11.8)$ ps
$T = (7.6 \pm 0.2)$ ps	$T = (7.6 \pm 0.1)$ ps
$t_0 = (1.3 \pm 0)$ ps	$t_0 = (1.3 \pm 0)$ ps
$\phi = (9.1 \pm 0.1)$ ps	$\phi = (1.7 \pm 0.1)$ ps
$c = (-0.0002 \pm 0.0002)$	$c = (-0.0003 \pm 0.0002)$
$R^2 = 0.744$	$R^2 = 0.802$

Figure 45: Complete parameter set of the fitted residuals of MoS₂ from section 8.3 with coefficient of determination. An error of zero indicates fixed parameters.

C Standard deviation of inelastic scattering fit parameters

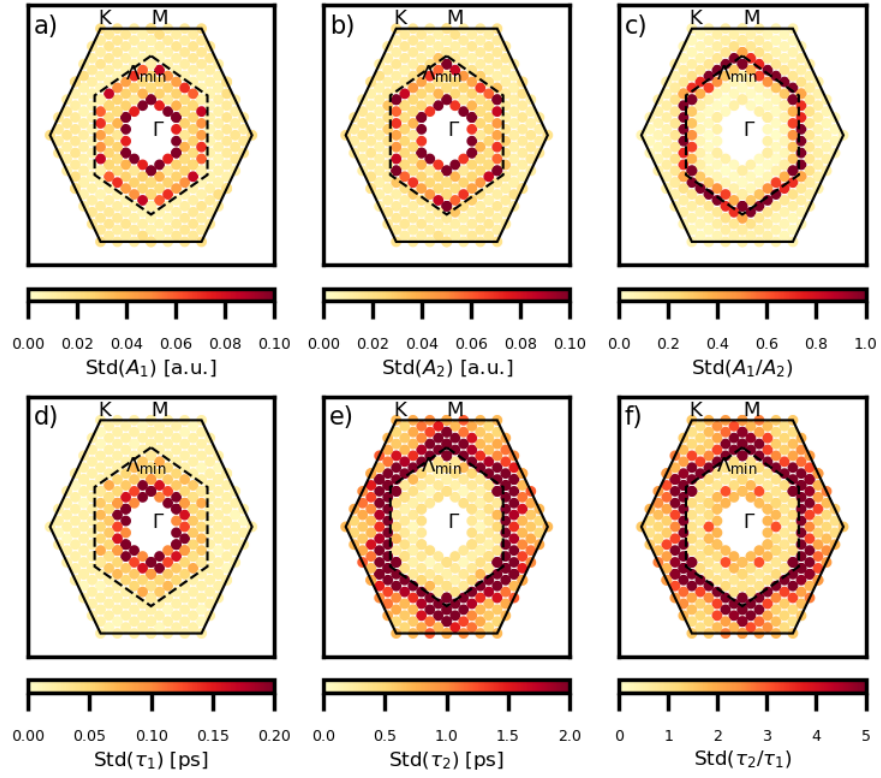


Figure 46: Complete parameter set of the fitted residuals of MoS2 from section 8.3 with coefficient of determination. An error of zero indicates fixed parameters.

D Complete phonon temperatures of every branch

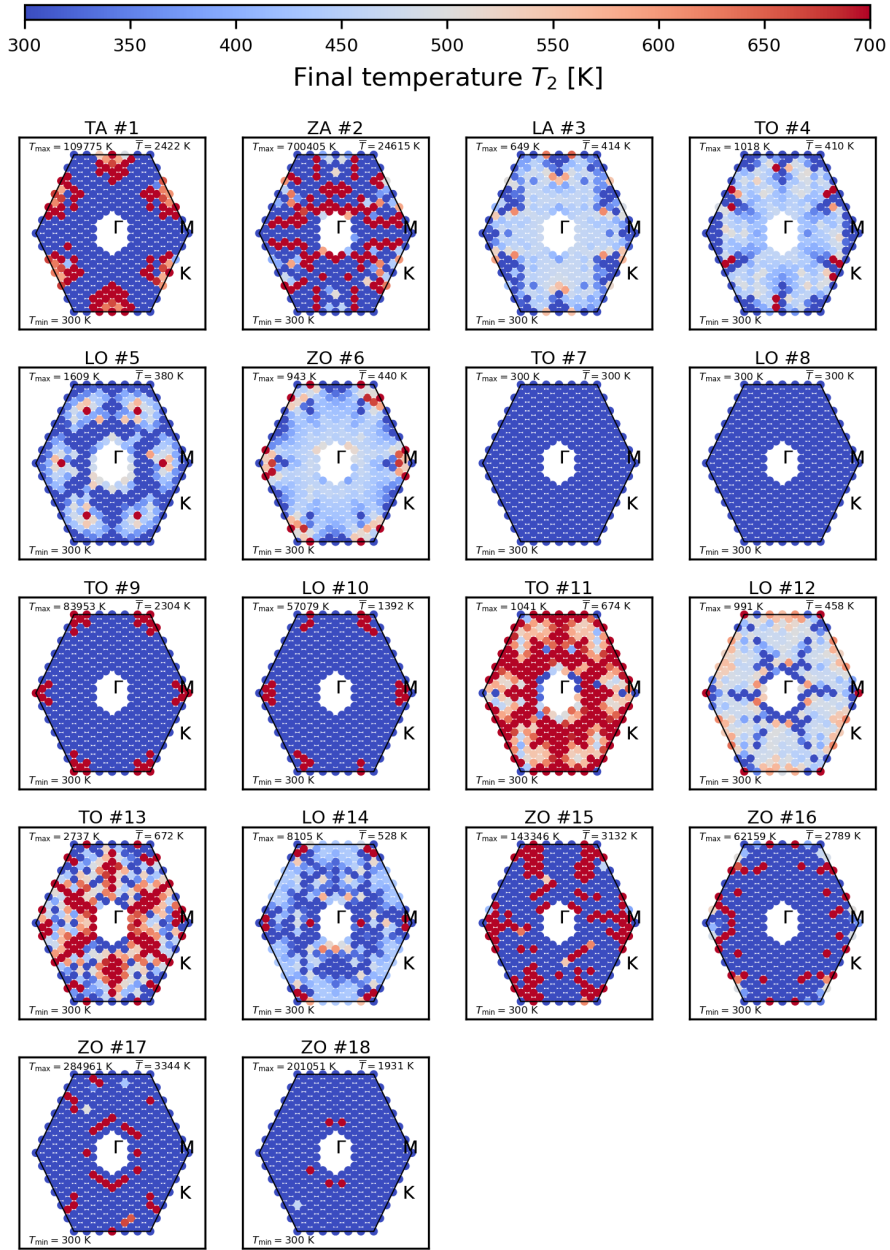


Figure 47: Final temperature T_2 of every phonon branch of MoS_2 obtained by the self-consistency test, using all phonon branches.

Acknowledgements

First and foremost, I would like to thank Prof. Dr. Ralph Ernstorfer for giving me the possibility to write my second and probably not last thesis in his very supportive and outstanding group.

The work presented in this thesis was performed in collaboration with Dr. Hélène Seiler and Dr. Marios Zacharias. It was truly a pleasure to work with you.

Very special thanks go out to Dr. Hélène Seiler, who has taken on the role of my supervisor and conducted the experimental parts of this thesis. I really have to point out the time you took to comment, question and discuss mostly all parts of my thesis, not only during a worldwide pandemic, but also but also in your parental leave. I really appreciate that. Without you, this work would not have been possible in this form.

I also gratefully acknowledge Dr. Marios Zacharias for providing me with his knowledge, interesting discussions and calculations of diffuse scattering intensities which were truly essential for this thesis.

I would like to thank PhD Daniela Zahn and Dr. Yoav William Windsor for always having an ear open for my questions and assisted in the experimental parts of this thesis.

On a more personal note, I owe special thanks to my partner, Hannah Kröger, for all her support, encouragement and giving me a wonderful daughter during this thesis.

Special thanks to my mother whose love and support has known no bounds.

Selbstständigkeitserklärung

Ich erkläre hiermit, dass ich die vorliegende Arbeit selbstständig verfasst und noch nicht für andere Prüfungen eingereicht habe. Sämtliche Quellen einschließlich Internetquellen, die unverändert oder abgewandelt wiedergegeben werden, insbesondere Quellen für Texte, Grafiken, Tabellen und Bilder, sind als solche kenntlich gemacht. Mir ist bekannt, dass bei Verstößen gegen diese Grundsätze ein Verfahren wegen Täuschungsversuchs bzw. Täuschung eingeleitet wird.

Ort, Datum

Unterschrift